TIME-DEPENDENT APPROACHES AND THEIR UTILITY: DYNAMICAL FORMULATIONS OF TWO-DIMENSIONAL ELECTRONIC SPECTROSCOPY SIGNALS AND ELECTRONIC STRUCTURE THEORY

by

ALEXIS J. KIESSLING

A DISSERTATION

Presented to the Department of Chemistry and Biochemistry
and the Graduate School of the University of Oregon
in partial fulfillment of the requirements
for the degree of
Doctor of Philosophy

June 2020

DISSERTATION APPROVAL PAGE

Student: Alexis J. Kiessling

Title: Time-Dependent Approaches and Their Utility: Dynamical Formulations of Two-Dimensional Electronic Spectroscopy Signals and Electronic Structure Theory

This dissertation has been accepted and approved in partial fulfillment of the requirements for the Doctor of Philosophy degree in the Department of Chemistry and Biochemistry by:

Cathy Wong	Chair
Jeffrey Cina	Core Member
George Nazin	Core Member
Steven van Enk	Institutional Representative

and

Kate Mondloch	Interim Vice Provost and Dean of the Graduate School

Original approval signatures are on file with the University of Oregon Graduate School.

Degree awarded June 2020

DISSERTATION ABSTRACT

Alexis J. Kiessling

Doctor of Philosophy

Department of Chemistry and Biochemistry

June 2020

Title: Time-Dependent Approaches and Their Utility: Dynamical Formulations of Two-Dimensional Electronic Spectroscopy Signals and Electronic Structure Theory

We present time-dependent reframings of the theory of two-dimensional electronic spectroscopy signals and of electronic structure theory. The dynamical formulation of spectroscopic signals, in particular of two-dimensional wave-packet interferometry (WPI), is used to calculate and interpret signals from a spatially oriented energy transfer dimer. A general study of the detection of electronic energy transfer using WPI is carried out. The signals are interpreted using a semiclassical analysis that considers the paths taken by wave packets through phase space and the conditions required for their phase-space overlap. The dimer is also used to propose a WPI experiment capable of observing electronic intersite and interexciton coherence. Weak-coupling (intersite) and strong-coupling (interexciton) cases are studied, with a variety of systems differing in number of vibrational modes and in excited-state energies of the monomers. The time-dependent framing of electronic structure theory is a spectral filtering technique, where the Fourier transform of the time evolution of an antisymmetrized wave packet to the frequency domain reveals eigenstates and eigenenergies. Direct numerical integration of the time-dependent Schrödinger equation and semiclassical parametrizations are presented and compared as methods of obtaining the time evolution. The method

is found to be accurate, and has some benefits; spectral filtering allows for many eigenstates to be obtained at once and includes electron correlation automatically. Future prospects for each of these works are discussed.

This dissertation includes previously published and unpublished co-authored material.

CURRICULUM VITAE

NAME OF AUTHOR: Alexis J. Kiessling

GRADUATE AND UNDERGRADUATE SCHOOLS ATTENDED:

University of Oregon, Eugene, OR
Mansfield University of Pennsylvania, Mansfield, PA

AREAS OF SPECIAL INTEREST:

Ultrafast Spectroscopy
Electronic Energy Transfer
Wave-Packet Dynamics

PROFESSIONAL EXPERIENCE:

Graduate Research Assistant, University of Oregon, 2016-2020
Graduate Teaching Assistant, University of Oregon, 2015-2020

PUBLICATIONS:

A.J. Kiessling and J.A. Cina, "Exploring a real-time approach to electronic structure calculations", *manuscript under revision for Mol. Phys.*

A.J. Kiessling and J.A. Cina, "Monitoring the evolution of intersite and interexciton coherence in electronic excitation transfer via wave-packet interferometry", *in press in J. Chem. Phys.*

J.A. Cina and A.J. Kiessling, "Nuclear wave-packet dynamics in two-dimensional interferograms of excitation transfer systems", in Coherent Multidimensional Spectroscopy, edited by M. Cho, Chap. 3 (Springer Nature, Singapore, 2019), pp. 51-85.

ACKNOWLEDGEMENTS

I would like to begin by acknowledging my advisor, Jeff Cina, for all of the guidance and patience while working on the works contained in this dissertation.

A special acknowledgement is in order for the members of the 2018-19 GTFF bargaining team, all of whom I am so proud to have had the opportunity to work with. Thanks to Mike Magee, Ellen Kress, Youssef Benasser, Trevor Brunnenmeyer, Curtis Dlouhy, Michelle Dreiling, Andy Labuza, Haley Laningham, Pearl Lee, Alberto Lioy, Rita Ludwig, Michael Marchman, Adam Morse, Juan Ospina, Hannah Pell, Larissa Petrucci, Kyle Raze, Morgan Sosa, and Sarah Stach.

Special thanks as well to the 2019-20 GTFF Executive Board - many of you were already listed, but I'm going to list you again anyway! This has been a difficult year. Thank you, Teresa Caprioglio, Rajeev Ravisankar, Rachel Hampton, Sarah Stach, Ellen Kress, Michelle Dreiling, Alberto Lioy, Morgan Sosa, and Trevor Brunnenmeyer, for being a part of it with me.

And finally, a very special thank you to Morgan Sosa and James Sadighian, for listening to a friend one late night in March when she really needed it.

This dissertation is the product of unionized labor by a member of the Graduate Teaching Fellows Federation, AFT Local 3544.

TABLE OF CONTENTS

Chapter Page

LIST OF FIGURES

LIST OF TABLES

Table Page

CHAPTER I

INTRODUCTION

Time dependent formulations of quantum mechanics are insightful because they connect a strange set of phenomena to our physical intuitions about the world. These intuitions, of course, come from our daily experiences of classical mechanics, and at the heart of these experiences is the movement of objects. Thinking about quantum mechanics from a dynamical perspective is thinking about the movement of wave packets, which often move in a way that is consistent with our classically-informed physical intuition. The works presented in this dissertation are united by this theme of dynamics, consisting of theoretical frameworks of ultrafast spectroscopy and electronic structure theory centered on time evolution.

Chapter II reframes the theory of two-dimensional electronic spectroscopy, particularly two-dimensional wave-packet interferometry (WPI), to highlight the dynamics underlying the signals. Expressions for general signals are derived in terms of the time-dependent wave functions - wave packets - generated by the action of the ultrashort laser pulses used in these experiments. The overlap of these wave packets with each other gives rise to the fluorescence-detected signal in a WPI experiment, and bringing the focus of the theory to the dynamics allows for insightful physical interpretation.

This chapter also introduces a model energy transfer dimer and makes use of this model to elucidate the manifestation of electronic energy transfer in WPI signals. The dimer is oriented such that controlling the polarizations of the pulses allows for the selection of individual monomers. An energy offset between monomer electronic states provides interesting dynamical consequences. The overlaps contributing to the WPI signal are analyzed semiclassically through the

phase-space trajectories of the wave packets. Additionally, the influence of an exciton shift, a lowering in the energy of excited states when both monomers are excited, on the overall signal is studied.

Chapter II was previously published in Coherent Multidimensional Spectroscopy, a book published by Springer Nature and edited by Minhaeng Cho. It was initiated by Jeffrey Cina. Both Jeffrey Cina and Alexis Kiessling derived the expressions and computed the signals appearing in the chapter. Jeffrey Cina was the principal investigator during this work.

Chapter III extends on the work of Chapter II. The same spatially-oriented dimer is used to both demonstrate the appearance of electronic coherence in WPI signals and propose an experimental strategy for observing the coherence. WPI experiments make use of two pairs of phase-locked pulses, and the coherence is found to live in the portion of WPI data where the intrapulse-pair delays are zero. The remaining interpulse-pair delay is used to track the time-development of the coherence. The proposed experiment requires a fixed spatial orientation, as the coherence detection relies on a pulse polarization scheme where the first three pulses probe only the "donor" state and the fourth pulse probes only the "acceptor" state. These states depend on the strength of the coupling; in the weak-coupling regime, the coherence is between site states, and in the strong-coupling regime, the coherence is between excitons. Both cases are explored in this chapter.

This chapter nicely illustrates the utility of a dynamical framework of thinking. The coherence of interest is shown to be the overlap between two particular wave packets. A theoretical framework which is primarily concerned with the motion of wave packets, combined with the knowledge that the electronic

coherence is simply a particular overlap of two wave packets, makes consideration of the experiment proposed in this chapter readily available.

Chapter III has been submitted for publication in the Journal of Chemical Physics, authored by Alexis Kiessling and Jeffrey Cina. Both Jeffrey Cina and Alexis Kiessling derived the expressions and computed the signals appearing in the chapter. Jeffrey Cina was the principal investigator during this work.

Chapter IV changes the focus from ultrafast spectroscopy to electronic structure theory, though it still shares the theme of dynamics. An initial exploration of a spectral filtering approach to numerically approximating solutions to the time-independent Schrödinger equation is carried out. Fourier transformation of the time evolution of an arbitrary antisymmetrized wave packet results in resonance at frequencies proportional to eigenenergies of the system Hamiltonian, while the Fourier coefficients approximate the corresponding eigenfunctions. Spectral filtering is applied to a model two-particle system using both direct numerical integration of the Schrödinger equation and a semiclassical parametrization. This simple model consists of harmonic oscillator potentials, and serves as a proof of concept. In direct numerical integration, a discrete position basis describes the time-evolution operator, which is then repeatedly applied to an antisymmetrized wave packet to obtain the packet's time evolution. The accuracy of the approach is considered through the eigenstate fidelities as a function of propagation time; the fidelity of a numerically determined eigenstate calculated with respect to the analytical solution increases with propagation time and approaches unity. In the semiclassical parametrization, equations of motion for the parameters are obtained from the Dirac-Frenkel-McLachlan functional [1, 2, 3]. Parametrization is applied both to the two-particle, harmonic-potential model

and to a single-particle system that contains a regularized Coulomb potential. The semiclassical approach requires less memory and accurately obtains the eigenspectrum, and for the two-particle system, the fidelities of the semiclassically determined eigenstates match the fidelities of the eigenstates determined by the direct numerical approach.

Chapter IV is a joint work between Alexis Kiessling and Jeffrey Cina being prepared for resubmission to Molecular Physics. Alexis Kiessling derived the expressions and computed the signals appearing in the chapter.

This dissertation is arranged as follows: Chapter II presents previously published work on two-dimensional wave-packet interferometry that elucidates the manifestation of electronic energy transfer in WPI signals. Chapter III presents work in press in Journal of Chemical Physics on the detection of electronic coherence through a specialized WPI experiment. Chapter IV discusses a dynamical approach to the stationary wave functions that make up electronic structure. Chapter V ends with a discussion of these works and possible future directions. Appendix A provides a derivation of a pump-probe experiment that has the same coherence-detecting ability as the WPI experiment in Chapter III, and Appendix B derives expressions for the same WPI experiment in the strong-coupling case. Appendices C and D provide expressions for the matrix elements that compose the equations of motion used to employ two different parametrized ansatzes for spectral filtering.

CHAPTER II

NUCLEAR WAVE-PACKET DYNAMICS IN TWO-DIMENSIONAL INTERFEROGRAMS OF EXCITATION-TRANSFER SYSTEMS

This work was previously published in Coherent Multidimensional Spectroscopy, a book published by Springer Nature and edited by Minhaeng Cho. Both Jeffrey Cina and Alexis Kiessling derived the expressions and computed the signals appearing in the chapter. Jeffrey Cina wrote the paper with assistance from Alexis Kiessling. Jeffrey Cina was the principle investigator during this work.

2.1 Introduction

Optically phase-coherent two-dimensional electronic spectroscopy has proved itself in recent years as an effective technique for revealing unprecedentedly detailed information on electronic excitation transfer (EET) within chromophore arrays [4, 5]. Because the molecular systems under study often comprise several participating excitation sites and a large number of interacting vibrational modes, all present in a variety of overall orientations with respect to the polarization of the incident light pulses, their signals' simulation and interpretation can become rather involved [6, 7, 8].

Here, for the sake of sharpening our thinking about some basic aspects of the information content of multi-dimensional spectroscopy and its interpretation in terms of the underlying, entangled electronic and nuclear dynamics, we undertake an exercise of reframing the basic theory with an emphasis on the role of nonstationary nuclear wave functions under the influence of laser pulse- and energy transfer-driven transitions among relevant site, adiabatic, or spatially-extended exciton states. While our treatment conforms in its physical content with those based on nonlinear optical response functions, its set-up differs from conventional

approaches in reversing the order of quantum-mechanical averaging and temporal integration over the external fields. It performs the latter operation *first*, with the interpretive and computational advantages that the analysis then turns on the dynamics of the nonstationary molecular states actually prepared and probed by phase-coherent, short-pulse optical spectroscopy.

This work expands on a previous study by Cina, Kilin, and Humble [9], who investigated two-dimensional signals from model systems similar to that used for illustration here, but made some additional simplifying assumptions. The model used here consists of a dimer that interacts with four identically shaped laser pulses resonant with the bare electronic transition frequency of the constituent chromophores. The total time-dependent wave function is expressed as a sum of nuclear wave packets evolving in different electronic states that have various different interactions with the pulses. The quantum mechanical overlaps of these wave packets give rise to the 2D ES signal. The dynamics of an individual wave packet is determined by its episodes of motion under the relevant vibronic Hamiltonians describing both evolution on a particular electronic potential energy surface and energy-transfer and/or nonadiabatic transitions between surfaces, interspersed with pulse actions that shape it and also effect its inter-surface transfer. The resulting spectra, plotted with respect to combinations of pulse-to-pulse delay times, are interpreted in terms of these dynamics.

In addition to the prior analysis of Cina, Kilin, and Humble, other works somewhat similar in spirit include that carried out by Tiwari, Peters, and Jonas [10] to explore the origin of oscillating peaks in 2D ES spectra and a theoretical study of the transfer and trapping of coherent vibrational motion in EET by Cina and Fleming [11]. The latter provided an explanation for the behavior

of vibrational quantum beats observed in time-resolved polarized fluorescence up-conversion measurements of LH-1 by Bradforth *et al.* [12], and the analysis of Tiwari *et al.* endeavored to illuminate the roles of coherent electronic and vibrational dynamics in producing signal oscillations from EET systems. Both of those reports make use of models similar to the one studied here. Butkus *et al.* [13] explored similar questions, comparing calculated signals from a monomer model with only vibronic coupling and a dimer model with only electronic coupling. Biggs and Cina investigated the influence that preparing nonstationary states of nuclear motion can exert on EET after subsequent electronic excitation [14, 15, 16].

In a four-wave mixing (FWM) rendition of 2D ES, the experiments detect the interference between a laser pulse that serves as a local oscillator and a signal beam emitted by the oscillating third-order dipole moments induced in the sample by the other three pulses [17]. While it is possible to describe this kind of signal using a wave-packet framework, we restrict ourselves for the present to wave-packet interferometry (WPI) by fluorescence detection. Two-dimensional fluorescence spectroscopy measurements employing optical phase modulation came into prominence with the works of Tekavec, Lott, and Marcus [18] and Lott *et al* [19]. With certain differences due to fluorescence-yield weighting of contributions from singly- versus doubly-excited electronic states, phase-modulated WPI signals effect an isolation of sum- and difference-phased overlap combinations that is similar to the separation in FWM approaches between different wave-vector-matched directions.

This chapter continues by describing an EET dimer model consisting of interacting chromophores whose states of electronic excitation are coupled to a collection of intra-complex or environmental vibrational degrees of freedom. Basic

expressions are derived for the fluorescence-detected wave-packet interferometry signal resulting from the dimer's interaction with two optically phase-controlled ultrashort laser pulse-pairs. Contributions to the 2D WPI signal are calculated for the exemplary case of a spatially-oriented pair of weakly-coupled monomers with perpendicular electronic transition moments, each possessing a single Franck-Condon-active internal vibrational mode.

2.2 Energy-Transfer Dimer

We start by describing a molecular dimer model comprising four *site states*, $|\bar{g}g\rangle$, $|\bar{e}g\rangle$, $|\bar{g}e\rangle$, and $|\bar{e}e\rangle$, in which neither, one, or both of the monomers are electronically excited.[1] Such a complex can exhibit electronic energy (or excitation) transfer between the two singly excited states. The dimer Hamiltonian is $H = T + H_{el}(\hat{Q})$, where T is the nuclear kinetic energy. The electronic Hamiltonian in the site basis is

$$\begin{aligned} H_{el}(Q) = |\bar{g}g\rangle V_{\bar{g}g}(Q)\langle\bar{g}g| + |\bar{e}g\rangle V_{\bar{e}g}(Q)\langle\bar{e}g| + |\bar{g}e\rangle V_{\bar{g}e}(Q)\langle\bar{g}e| \\ + |\bar{e}e\rangle V_{\bar{e}e}(Q)\langle\bar{e}e| + J(Q)(|\bar{e}g\rangle\langle\bar{g}e| + |\bar{g}e\rangle\langle\bar{e}g|) \; . \end{aligned} \tag{2.1}$$

Q stands for the full collection of intramolecular and intermolecular nuclear coordinates, including those of any surrounding medium. Alternatively, the electronic Hamiltonian can be expressed in terms of the *adiabatic electronic states* as

$$\begin{aligned} H_{el}(Q) = |0\rangle E_0(Q)\langle 0| + |\bar{1}(Q)\rangle E_{\bar{1}}(Q)\langle\bar{1}(Q)| \\ + |1(Q)\rangle E_1(Q)\langle 1(Q)| + |2\rangle E_2(Q)\langle 2| \; . \end{aligned} \tag{2.2}$$

[1]The monomers may be the same or different. Our model neglects states such as $|\bar{e}'g\rangle$ or $|\bar{e}'e''\rangle$ in which one or both of the molecules occupy higher-lying electronic excited states.

It is easy to specify the relationship between these two representations. Let

$$\mathcal{P}_{one} = |\bar{e}g\rangle\langle\bar{e}g| + |\bar{g}e\rangle\langle\bar{g}e| \,, \tag{2.3}$$

$$\sigma_x = |\bar{e}g\rangle\langle\bar{g}e| + |\bar{g}e\rangle\langle\bar{e}g| \,, \tag{2.4}$$

$$\sigma_y = -i|\bar{e}g\rangle\langle\bar{g}e| + i|\bar{g}e\rangle\langle\bar{e}g| \,, \tag{2.5}$$

and

$$\sigma_z = |\bar{e}g\rangle\langle\bar{e}g| - |\bar{g}e\rangle\langle\bar{g}e| \,. \tag{2.6}$$

Introducing the following functions of nuclear coordinates,

$$K(Q) = \frac{1}{2}\big(V_{\bar{e}g}(Q) - V_{\bar{g}e}(Q)\big) \,, \tag{2.7}$$

$$L(Q) = \frac{1}{2}\big(V_{\bar{e}g}(Q) + V_{\bar{g}e}(Q)\big) \,, \tag{2.8}$$

$$M(Q) = \sqrt{J^2(Q) + K^2(Q)} \,, \tag{2.9}$$

and

$$\theta(Q) = \arctan\left(\frac{J(Q)}{K(Q)}\right) \,, \tag{2.10}$$

as illustrated in Fig. 1, allows us to rewrite Eq. (2.1) as

$$\begin{aligned} H_{el}(Q) &= |\bar{g}g\rangle\langle\bar{g}g|V_{\bar{g}g}(Q) + \sigma_x J(Q) + \sigma_z K(Q) + \mathcal{P}_{one}L(Q) + |\bar{e}e\rangle\langle\bar{e}e|V_{\bar{e}e}(Q) \\ &= |\bar{g}g\rangle\langle\bar{g}g|V_{\bar{g}g}(Q) + \mathcal{P}_{one}L(Q) \\ &\quad + e^{-i\sigma_y\theta(Q)/2}\sigma_z e^{i\sigma_y\theta(Q)/2}M(Q) + |\bar{e}e\rangle\langle\bar{e}e|V_{\bar{e}e}(Q) \,. \end{aligned} \tag{2.11}$$

The adiabatic eigenenergies appearing in Eq. (2.2) can be seen from Eq. (2.11) to be

$$E_0(Q) = V_{\bar{g}g}(Q) \,, \tag{2.12}$$

$$E_{\bar{1}}(Q) = L(Q) + M(Q) \,, \tag{2.13}$$

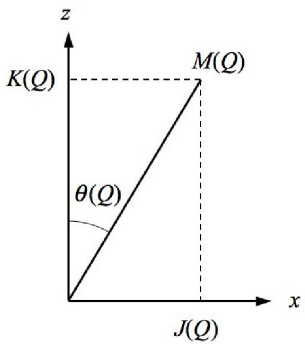

Figure 1. Parameters of the electronic Hamiltonian. $J(Q)$ is the energy-transfer coupling at nuclear configuration Q. $K(Q)$ is half the local site-energy difference. $M(Q)$ is half the resultant energy difference between adiabatic singly-excited electronic states.

$$E_1(Q) = L(Q) - M(Q) \,, \tag{2.14}$$

and

$$E_2(Q) = V_{\bar{e}e}(Q) \,. \tag{2.15}$$

The ground and doubly-excited adiabatic eigenstates of the model dimer, $|0\rangle = |\bar{g}g\rangle$ and $|2\rangle = |\bar{e}e\rangle$, respectively, remain unchanged from the site basis. The singly-excited adiabatic states can be defined as

$$|\bar{1}(Q)\rangle = e^{-i\sigma_y\theta(Q)/2}|\bar{e}g\rangle \,, \tag{2.16}$$

and

$$|1(Q)\rangle = e^{-i\sigma_y\theta(Q)/2}|\bar{g}e\rangle \,. \tag{2.17}$$

The electronic Hamiltonian for this dimer has been diagonalized by a Q-dependent unitary transformation. But the remaining contribution to the full Hamiltonian, the nuclear kinetic-energy operator T, may couple the adiabatic electronic states of the single-excitation manifold in the presence of sufficiently rapid nuclear motion. We shall see shortly that the dipole moment operator connecting single-excitation states to the electronic ground state or to the doubly

excited state become Q-dependent in the basis of adiabatic electronic states. This feature can complicate the description (using pulse propagators, as described below) of short-pulse-driven electronic transitions. Such complications do not arise in the site basis, with its nuclear coordinate-independent electronic states.

Another popular basis featuring Q-independent electronic states is the *exciton basis*. It consists of the four eigenstates of the electronic Hamiltonian evaluated at the equilibrium nuclear configuration of the electronic ground state $H_{el}(Q = 0)$: $|0\rangle$, $|1\rangle \equiv |1(0)\rangle$, $|\bar{1}\rangle \equiv |\bar{1}(0)\rangle$, and $|2\rangle$. The matrix elements of the electronic Hamiltonian in this basis are readily obtained. For example,

$$\begin{aligned}\langle\bar{1}|H_{el}(Q)|\bar{1}\rangle &= \langle\bar{1}|\bar{1}(Q)\rangle\langle\bar{1}(Q)|\bar{1}\rangle E_{\bar{1}}(Q) + \langle\bar{1}|1(Q)\rangle\langle 1(Q)|\bar{1}\rangle E_1(Q) \\ &= \langle\bar{e}g|e^{-i\frac{\delta\theta(Q)}{2}\sigma_y}|\bar{e}g\rangle\langle\bar{e}g|e^{i\frac{\delta\theta(Q)}{2}\sigma_y}|\bar{e}g\rangle E_{\bar{1}}(Q) \\ &\quad + \langle\bar{e}g|e^{-i\frac{\delta\theta(Q)}{2}\sigma_y}|\bar{g}e\rangle\langle\bar{g}e|e^{i\frac{\delta\theta(Q)}{2}\sigma_y}|\bar{e}g\rangle E_1(Q)\,, \end{aligned} \tag{2.18}$$

with $\delta\theta(Q) = \theta(Q) - \theta(0) \equiv \theta(Q) - \theta$. Simplification leads to

$$\langle\bar{1}|H_{el}(Q)|\bar{1}\rangle = L(Q) + M(Q)\cos\delta\theta(Q)\,. \tag{2.19}$$

By similar analyses,

$$\langle 1|H_{el}(Q)|1\rangle = L(Q) - M(Q)\cos\delta\theta(Q)\,, \tag{2.20}$$

and

$$\langle 1|H_{el}(Q)|\bar{1}\rangle = \langle\bar{1}|H_{el}(Q)|1\rangle = M(Q)\sin\delta\theta(Q)\,. \tag{2.21}$$

Using the definition of $\delta\theta(Q)$, we easily find

$$\cos\delta\theta(Q) = \frac{K(Q)K + J(Q)J}{M(Q)M}\,, \tag{2.22}$$

and

$$\sin\delta\theta(Q) = \frac{J(Q)K - K(Q)J}{M(Q)M}\,. \tag{2.23}$$

Combining these results and introducing the definitions $\delta J(Q) = J(Q) - J$ and $\delta K(Q) = K(Q) - K$, we arrive at the expression

$$\begin{aligned} H_{el}(Q) = |0\rangle\langle 0|E_0(Q) &+ |\bar{1}\rangle\langle\bar{1}|\Big\{L(Q) + M + \frac{K\delta K(Q) + J\delta J(Q)}{M}\Big\} \\ &+ |1\rangle\langle 1|\Big\{L(Q) - M - \frac{K\delta K(Q) + J\delta J(Q)}{M}\Big\} \\ &+ (|\bar{1}\rangle\langle 1| + |1\rangle\langle\bar{1}|)\Big\{\frac{K\delta J(Q) - J\delta K(Q)}{M}\Big\} + |2\rangle\langle 2|E_2(Q)\,, \end{aligned} \tag{2.24}$$

for the electronic Hamiltonian in the exciton basis.

In order to choose between the two nuclear coordinate-independent electronic bases in a given instance, we can compare the respective ratios of the off-diagonal matrix elements of their Hamiltonians to the difference between the two diagonal matrix elements within the singly-excited manifold. The site basis is seen to be favored by small values of the quantity

$$\Big|\frac{J(Q)}{V_{\bar{e}g}(Q) - V_{\bar{g}e}(Q)}\Big| = \frac{1}{2}\Big|\frac{J(Q)}{K(Q)}\Big|\,. \tag{2.25}$$

On the other hand, small values of

$$\left|\frac{K\delta J(Q) - J\delta K(Q)}{M}\frac{1}{2\big(M + \frac{K\delta K(Q) + J\delta J(Q)}{M}\big)}\right| = \frac{1}{2}\Big|\frac{K\delta J(Q) - J\delta K(Q)}{M^2 + K\delta K(Q) + J\delta J(Q)}\Big| \tag{2.26}$$

support a choice of the exciton basis. These criteria indicate that the site (exciton) basis is preferred under conditions of weak (strong) energy-transfer coupling.

2.3 Whoopee Signal

2.3.1 Interaction Hamiltonian

Next, we develop basic formulas for the fluorescence-detected WPI signal from the dimer complex. In order to carry out this derivation, we add to the Hamiltonian a time-dependent perturbation accounting for the dimer's interaction

with a sequence of four ultrashort laser pulses,

$$V(t) = \sum_{I=A,B,C,D} V_I(t)\,, \tag{2.27}$$

with

$$V_I(t) = -\hat{\mathbf{m}} \cdot \mathbf{E}_I(t)\,. \tag{2.28}$$

The electric fields are

$$\mathbf{E}_I(t) = \mathbf{e}_I E_I f_I\left(t - t_I(\mathbf{r})\right) \cos\left[\Omega(t - t_I\left(\mathbf{r}\right)) + \varphi_I\right]\,. \tag{2.29}$$

The quantity $\mathbf{e}_I$ in Eq. (2.29) is the polarization unit vector (assumed to be real) and $t_I(\mathbf{r}) = t_I + \mathbf{n}_I \cdot \mathbf{r}/c$ is the arrival time of the pulse at the molecular location, with t_I being the arrival time at some origin ($\mathbf{r} = 0$) within the sample and $\mathbf{n}_I$ being a unit vector in the direction of the laser beam's spatial propagation. We are specializing to the common situation in which the optical phase *differences* $\varphi_{BA} \equiv \varphi_B - \varphi_A$ and $\varphi_{DC} \equiv \varphi_D - \varphi_C$ are under experimental control even though the individual φ_I may vary randomly on successive laser shots due to mechanical jitter in the optical setup. As illustrated in Fig. 2, the pulse sequence comprises two phase-controlled pulse-pairs. The variable intrapulse-pair delays $t_{BA} \equiv t_B - t_A$ and $t_{DC} \equiv t_D - t_C$, or their conjugate frequency variables, are the two "dimensions" of a 2D WPI experiment. The pulse arrivals at the sample origin obey $t_A \leq t_B$, $t_C \leq t_D$, and $t_A + t_B \leq t_C + t_D$ (as explained on p. 18).

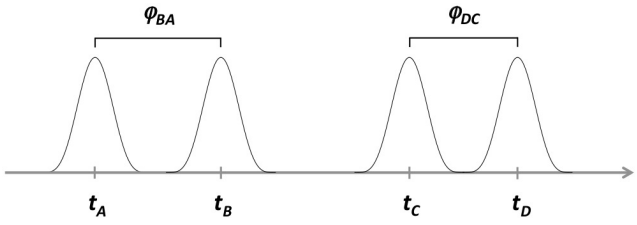

Figure 2. Electric field envelopes in a 2D WPI experiment are shown schematically, along with their arrival times and controlled intrapulse-pair optical phase shifts.

The dipole operator is

$$\hat{\mathbf{m}} = \mathbf{m}_a \left(|\bar{e}g\rangle\langle\bar{g}g| + |\bar{e}e\rangle\langle\bar{g}e|\right) + \mathbf{m}_b \left(|\bar{g}e\rangle\langle\bar{g}g| + |\bar{e}e\rangle\langle\bar{e}g|\right) + \text{H.c.} \tag{2.30}$$

We can find this operator in the adiabatic electronic basis by calculating its matrix elements,

$$\begin{aligned}\langle\bar{1}(Q)|\hat{\mathbf{m}}|0\rangle &= \mathbf{m}_a\langle\bar{1}(Q)|\bar{e}g\rangle + \mathbf{m}_b\langle\bar{1}(Q)|\bar{g}e\rangle \\ &= \mathbf{m}_a \cos\frac{\theta(Q)}{2} + \mathbf{m}_b \sin\frac{\theta(Q)}{2}\,, \end{aligned} \tag{2.31}$$

$$\langle 1(Q)|\hat{\mathbf{m}}|0\rangle = -\mathbf{m}_a \sin\frac{\theta(Q)}{2} + \mathbf{m}_b \cos\frac{\theta(Q)}{2}\,, \tag{2.32}$$

$$\langle 2|\hat{\mathbf{m}}|\bar{1}(Q)\rangle = \mathbf{m}_a \sin\frac{\theta(Q)}{2} + \mathbf{m}_b \cos\frac{\theta(Q)}{2}\,, \tag{2.33}$$

and

$$\langle 2|\hat{\mathbf{m}}|1(Q)\rangle = \mathbf{m}_a \cos\frac{\theta(Q)}{2} - \mathbf{m}_b \sin\frac{\theta(Q)}{2}\,. \tag{2.34}$$

From these we obtain

$$\begin{aligned}\hat{\mathbf{m}} = {} & |\bar{1}(Q)\rangle\langle 0|\Big\{\mathbf{m}_a \cos\frac{\theta(Q)}{2} + \mathbf{m}_b \sin\frac{\theta(Q)}{2}\Big\} \\ & + |1(Q)\rangle\langle 0|\Big\{ - \mathbf{m}_a \sin\frac{\theta(Q)}{2} + \mathbf{m}_b \cos\frac{\theta(Q)}{2}\Big\} \\ & + |2\rangle\langle\bar{1}(Q)|\Big\{\mathbf{m}_a \sin\frac{\theta(Q)}{2} + \mathbf{m}_b \cos\frac{\theta(Q)}{2}\Big\} \\ & + |2\rangle\langle 1(Q)|\Big\{\mathbf{m}_a \cos\frac{\theta(Q)}{2} - \mathbf{m}_b \sin\frac{\theta(Q)}{2}\Big\} + \text{H.c.}\end{aligned} \tag{2.35}$$

Setting $Q = 0$ in Eq. (2.35) yields the dipole operator in the exciton basis:

$$\begin{aligned}\hat{\mathbf{m}} = {} & |\bar{1}\rangle\langle 0|\Big\{\mathbf{m}_a \cos\frac{\theta}{2} + \mathbf{m}_b \sin\frac{\theta}{2}\Big\} + |1\rangle\langle 0|\Big\{ - \mathbf{m}_a \sin\frac{\theta}{2} + \mathbf{m}_b \cos\frac{\theta}{2}\Big\} \\ & + |2\rangle\langle\bar{1}|\Big\{\mathbf{m}_a \sin\frac{\theta}{2} + \mathbf{m}_b \cos\frac{\theta}{2}\Big\} + |2\rangle\langle 1|\Big\{\mathbf{m}_a \cos\frac{\theta}{2} - \mathbf{m}_b \sin\frac{\theta}{2}\Big\} + \text{H.c.}\end{aligned} \tag{2.36}$$

2.3.2 2D Signal

The two-dimensional whoopee signal S depends on the quadrilinear contributions (proportional to $E_A E_B E_C E_D$) to the population of each of the several

electronic excited states. For a sample having uniform dimer density ρ throughout an illuminated volume V, it can be written

$$\begin{aligned} S &= \rho \int_V d^3r \big\{ Q_{\bar{e}e} P_{\bar{e}e}(\mathbf{r}) + Q_{\bar{e}g} P_{\bar{e}g}(\mathbf{r}) + Q_{\bar{g}e} P_{\bar{g}e}(\mathbf{r}) \big\} \\ &= \rho \int_V d^3r \big\{ Q_2 P_2(\mathbf{r}) + Q_{\bar{1}} P_{\bar{1}}(\mathbf{r}) + Q_1 P_1(\mathbf{r}) \big\} , \end{aligned} \tag{2.37}$$

where $P_\xi(\mathbf{r})$ is the quadrilinear portion of the ξ-state population of a dimer at position $\mathbf{r}$ and Q_ξ is the fluorescence quantum yield in that state.[2] The $\mathbf{r}$-dependence of the quadrilinear populations would become important if we wished to describe a set-up in which the four incident laser beams were noncollinear; in that case, wave-vector-matching conditions among the $\mathbf{n}_I$ would play a role analagous to or in concert with optical phase cycling in helping to isolate a particular quadrilinear contribution to the signal (i.e. one having a sum or difference optical phase combination, $\varphi_{DC} + \varphi_{BA}$ or $\varphi_{DC} - \varphi_{BA}$, respectively). In order to simplify subsequent formulas, we shall omit the $\mathbf{r}$-dependence from here on out, but it could easily be restored. The resulting formulas will apply as they are in the case of four collinear beams or in the in-principle-possible case of experiments on a single molecule, with the spatial integrals of Eq. (2.37) also being omitted in the latter instance.

2.3.2.1 Singly excited-state populations

We focus first on the contributions to Eq. (2.37) arising from the population of singly-excited electronic states. Among the 48 quadrilinear overlaps contributing (along with their complex conjugates) to the population of a given singly-excited state, we may omit the sixteen overlaps carrying an uncontrolled optical phase factor of the form $\exp\{\pm i(\varphi_A + \varphi_B) \pm i(\varphi_C + \varphi_D)\}$, as these average to negligibility

[2] We do not include an average over any possible orientational distribution of the dimer at a given location, regarding this as being implicitly included in the spatial distribution of population.

over the many laser shots needed to accumulate a WPI signal. The remaining, phase-stable contributions to P_ξ can be broken into separately measurable sum- and difference-phased components (see Section 2.3.2.3). Thus $P_\xi = P_\xi^{(s)} + P_\xi^{(d)}$, where

$$\begin{aligned} P_\xi^{(s)} = 2\mathrm{Re}\big\{ & \langle \uparrow_A \downarrow_B \uparrow_C |\xi\rangle\langle\xi| \uparrow_D\rangle + \langle \uparrow_A \downarrow_D \uparrow_C |\xi\rangle\langle\xi| \uparrow_B\rangle + \langle \uparrow_C |\xi\rangle\langle\xi| \uparrow_B \downarrow_A \uparrow_D\rangle \\ & + \langle \uparrow_A |\xi\rangle\langle\xi| \uparrow_B \downarrow_C \uparrow_D\rangle + \langle \uparrow_C \downarrow_B \uparrow_A |\xi\rangle\langle\xi| \uparrow_D\rangle + \langle \uparrow_C \downarrow_D \uparrow_A |\xi\rangle\langle\xi| \uparrow_B\rangle \\ & + \langle \uparrow_C |\xi\rangle\langle\xi| \uparrow_D \downarrow_A \uparrow_B\rangle + \langle \uparrow_A |\xi\rangle\langle\xi| \uparrow_D \downarrow_C \uparrow_B\rangle \\ & + \langle \uparrow_A \uparrow_C \downarrow_B |\xi\rangle\langle\xi| \uparrow_D\rangle + \langle \uparrow_A \uparrow_C \downarrow_D |\xi\rangle\langle\xi| \uparrow_B\rangle + \langle \uparrow_C |\xi\rangle\langle\xi| \uparrow_B \uparrow_D \downarrow_A\rangle \\ & + \langle \uparrow_A |\xi\rangle\langle\xi| \uparrow_B \uparrow_D \downarrow_C\rangle + \langle \uparrow_C \uparrow_A \downarrow_B |\xi\rangle\langle\xi| \uparrow_D\rangle + \langle \uparrow_C \uparrow_A \downarrow_D |\xi\rangle\langle\xi| \uparrow_B\rangle \\ & + \langle \uparrow_C |\xi\rangle\langle\xi| \uparrow_D \uparrow_B \downarrow_A\rangle + \langle \uparrow_A |\xi\rangle\langle\xi| \uparrow_D \uparrow_B \downarrow_C\rangle \big\}, \end{aligned} \tag{2.38}$$

and (by swapping Cs and Ds throughout)

$$\begin{aligned} P_\xi^{(d)} = 2\mathrm{Re}\big\{ & \langle \uparrow_A \downarrow_B \uparrow_D |\xi\rangle\langle\xi| \uparrow_C\rangle + \langle \uparrow_A \downarrow_C \uparrow_D |\xi\rangle\langle\xi| \uparrow_B\rangle + \langle \uparrow_D |\xi\rangle\langle\xi| \uparrow_B \downarrow_A \uparrow_C\rangle \\ & + \langle \uparrow_A |\xi\rangle\langle\xi| \uparrow_B \downarrow_D \uparrow_C\rangle + \langle \uparrow_D \downarrow_B \uparrow_A |\xi\rangle\langle\xi| \uparrow_C\rangle + \langle \uparrow_C \downarrow_D \uparrow_A |\xi\rangle\langle\xi| \uparrow_B\rangle \\ & + \langle \uparrow_D |\xi\rangle\langle\xi| \uparrow_C \downarrow_A \uparrow_B\rangle + \langle \uparrow_A |\xi\rangle\langle\xi| \uparrow_C \downarrow_D \uparrow_B\rangle \\ & + \langle \uparrow_A \uparrow_D \downarrow_B |\xi\rangle\langle\xi| \uparrow_C\rangle + \langle \uparrow_A \uparrow_D \downarrow_C |\xi\rangle\langle\xi| \uparrow_B\rangle + \langle \uparrow_D |\xi\rangle\langle\xi| \uparrow_B \uparrow_C \downarrow_A\rangle \\ & + \langle \uparrow_A |\xi\rangle\langle\xi| \uparrow_B \uparrow_C \downarrow_D\rangle + \langle \uparrow_D \uparrow_A \downarrow_B |\xi\rangle\langle\xi| \uparrow_C\rangle + \langle \uparrow_D \uparrow_A \downarrow_C |\xi\rangle\langle\xi| \uparrow_B\rangle \\ & + \langle \uparrow_D |\xi\rangle\langle\xi| \uparrow_C \uparrow_B \downarrow_A\rangle + \langle \uparrow_A |\xi\rangle\langle\xi| \uparrow_C \uparrow_B \downarrow_D\rangle \big\}. \end{aligned} \tag{2.39}$$

Reading from left to right within any bra or ket, the pulses must act on the dimer in the order listed, irrespective of their order of temporal arrival, driving upward (absorptive) or downward (emissive) electronic transitions. Explicit expressions for the contributing multi-pulse amplitudes are developed subsequently. We have written the various quadrilinear populations so the displayed overlaps have phase signature $e^{-i\varphi_{BA}-i\varphi_{DC}}$ and $e^{-i\varphi_{BA}+i\varphi_{DC}}$ in $P_\xi^{(s)}$ and $P_\xi^{(d)}$, respectively. The first eight

overlaps in each of the quadrilinear ξ-state populations do not access the doubly excited electronic state at any stage in the amplitude-transfer process described by the three-pulse bra or ket. In the last eight overlaps of $P_{\xi}^{(s)}$ and $P_{\xi}^{(d)}$, amplitude is generated in the doubly excited state by the action of the second pulse of the three-pulse bra or ket.

If we make the reasonable assumption that the quantum yields for fluorescence (or other action-spectroscopy signal) following excitation of the $\bar{e}g$- and $\bar{g}e$-states are equal, $Q_{\bar{e}g} = Q_{\bar{g}e} = Q_{one}$, then the total quadrilinear population of both singly-excited site states $P_{one}^{(s/d)} = P_{\bar{e}g}^{(s/d)} + P_{\bar{g}e}^{(s/d)}$ is all that matters. Expressions for $P_{one}^{(s)}$ and $P_{one}^{(d)}$ could be obtained from Eqs. (2.38) and (2.39), respectively by replacing $|\xi\rangle\langle\xi|$ with $\mathcal{P}_{one} = |\bar{e}g\rangle\langle\bar{e}g| + |\bar{g}e\rangle\langle\bar{g}e|$. But all the one- and three-pulse bras and kets appearing there generate amplitude only in the singly electronically-excited manifold. So the operator $|\xi\rangle\langle\xi|$ can simply be removed to give $P_{one}^{(s/d)}$. The same sort of argument of course applies in the exciton basis.

The various quadrilinear overlaps differ in their dependence on the interpulse delays, and it is through this delay dependence that WPI data provide information on the dynamics of the energy-transfer system. For bookkeeping purposes—and without any sacrifice of experimental data—we require that $t_A \leq t_B$, $t_C \leq t_D$, and $(t_A + t_B)/2 \leq (t_C + t_D)/2$. Assuming that all four pulses have identical envelopes, any data obtained with t_B less than t_A would coincide with those within the prescribed range having t_A and t_B interchanged and φ_{BA} changed in sign; a similar statement holds for data with t_D less than t_C. Data with the midpoint of t_C and t_D less than that of t_A and t_B exist in the prescribed range with t_A interchanged with t_C, t_B interchanged with t_D, and φ_{BA} swapped with φ_{DC}. An exhaustive range of interpulse delays thus spans a three-dimensional space $\{t_{BA}, t_{DC}, t_{CB}\}$ with t_{BA} and

t_{DC} greater than or equal to zero and t_{CB} greater than or equal to $-(t_{DC} + t_{BA})/2$. Notice that under these restrictions, t_B can be before, between, or after t_C and t_D, and t_A can come before or after t_C, provided $t_{DC} + 2t_{CB} + t_{BA}$ remains nonnegative.

Because the pulses have short durations that sometimes preclude their acting in the required order, each of the wave-packet overlaps in Eqs. (2.38) and (2.39) is restricted in the range of interpulse delays for which it can make a contribution to the WPI signal. Let's identify the three-dimensional regions of the "delay space" within which each of the overlaps participating in $P_{one}^{(d)}$ may be active.

First we consider $\langle \uparrow_A \downarrow_B \uparrow_D \mid \uparrow_C \rangle$, which is responsible for bleaching the electronic ground state. Since the D pulse acts after the B pulse in this term, the overlap vanishes if t_D precedes t_B by more than approximately the pulse duration, whence $t_D - t_B > -\sigma$, or $t_{DC} + t_{CB} + \sigma > 0$. Together with the general restriction that $t_{DC} + 2t_{CB} + t_{BA}$ be nonnegative, this condition confines the overlap to the 3D temporal region plotted in Fig. 3. A similar argument for the stimulated-emission overlap, $\langle \uparrow_A \downarrow_C \uparrow_D \mid \uparrow_B \rangle$, shows that it can only exist within the 3D region where $t_{CB} + t_{BA} + \sigma > 0$ and $t_{DC} + 2t_{CB} + t_{BA} > 0$, which corresponds to the mirror image of the volume shown in Fig. 3 through the vertical plane $t_{DC} = t_{BA}$, containing the t_{CB} axis.

There are also fully three-dimensional regions of interpulse delays where the overlaps $\langle \uparrow_A \mid \uparrow_C \downarrow_D \uparrow_B \rangle$ and $\langle \uparrow_D \mid \uparrow_C \downarrow_A \uparrow_B \rangle$ may be nonnegligible. Since pulse D acts before pulse B in the first of these, its arrival times must obey $t_D - t_B < \sigma$, and $\langle \uparrow_A \mid \uparrow_C \downarrow_D \uparrow_B \rangle$ is therefore confined to the shared range of $t_{DC} + t_{CB} < \sigma$ and $t_{DC} + 2t_{CB} + t_{BA} > 0$ plotted in Fig. 4. For $\langle \uparrow_D \mid \uparrow_C \downarrow_A \uparrow_B \rangle$ on the other hand, pulse C must act before pulse A, whence $t_C - t_A < \sigma$. This overlap can make a nonvanishing contribution to $P_{one}^{(d)}$ when $t_{CB} + t_{BA} < \sigma$ and $t_{DC} + 2t_{CB} + t_{BA} > 0$.

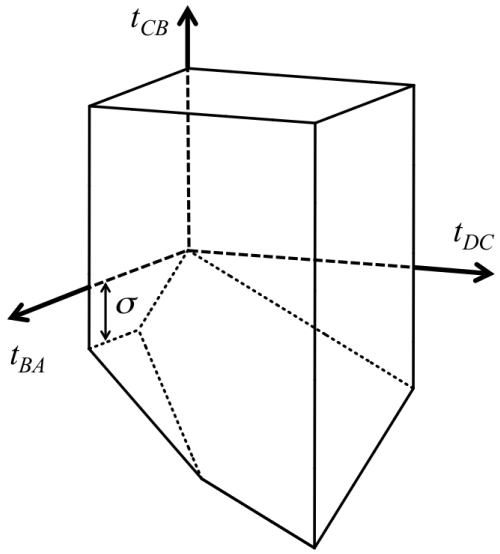

Figure 3. Three-dimensional region of time-delay parameter space in which the ground-state-bleach contribution to the difference-phased 2D-WPI signal may be nonvanishing. The region shown is to be extended to arbitrarily large, positive values of t_{BA} and t_{DC}, and to arbitrarily large positive and negative values of t_{CB} (while maintaining t_{CB} greater than both $-(t_{DC} + t_{BA})/2$ and $-\sigma - t_{DC}$). The stimulated-emission overlap may be nonzero in the temporal region generated from that depicted here by reflection through the $t_{DC} = t_{BA}$ plane.

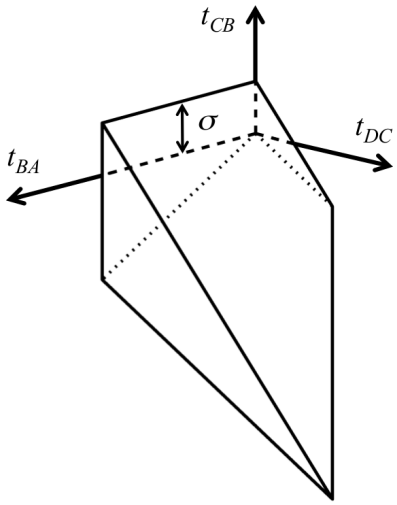

Figure 4. Delay region in which the contribution of $\langle\uparrow_A \mid \uparrow_C\downarrow_D\uparrow_B\rangle$ to the difference-phased 2D-WPI signal may not vanish. The pictured volume is to be extended to arbitrarily large, positive values of t_{BA} and t_{DC}, while maintaining t_{CB} greater than $-(t_{DC} + t_{BA})/2$ and less than $\sigma - t_{DC}$. The region of possibly nonvanishing $\langle\uparrow_D \mid \uparrow_C\downarrow_A\uparrow_B\rangle$ is the mirror image of this one through the vertical $t_{DC} = t_{BA}$ plane.

This region mirrors the volume shown in Fig. 4 through the $t_{DC} = t_{BA}$ plane. Note that the delay-range regions where both of these overlaps may contribute are largely limited to negative t_{CB}.

In $\langle\uparrow_A \mid \uparrow_B\downarrow_D\uparrow_C\rangle$, the D pulse acts before the C pulse, despite the fact that by definition the arrival time t_D follows t_C; $t_{DC} < \sigma$. Since the B pulse also acts before the C pulse in this overlap, but t_C can precede t_B in the specified range of unique interpulse delays, $t_B - t_C$ has to be less than the pulse length, so $t_{CB} > -\sigma$ is required as well. Together with $t_{DC} + 2t_{CB} + t_{BA} > 0$, these conditions restrict $\langle\uparrow_A \mid \uparrow_B\downarrow_D\uparrow_C\rangle$ to the quasi-2D time-delay region illustrated in Fig. 5. The delay region for $\langle\uparrow_D \mid \uparrow_B\downarrow_A\uparrow_C\rangle$ is obtained by reflecting this slab in the $t_{DC} = t_{BA}$ plane.

The two remaining overlaps in $P^{(d)}_{one}$ which do not access the doubly-excited state are limited to quasi zero-dimensional delay regions. Since pulse B and D both act before pulse A in $\langle\uparrow_D\downarrow_B\uparrow_A \mid \uparrow_C\rangle$, this overlap cannot contribute unless t_{BA} and

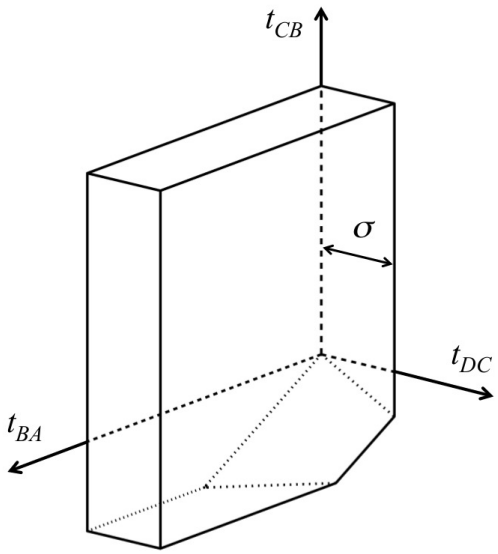

Figure 5. Quasi-2D time-delay region in which the overlap $\langle \uparrow_A \quad | \quad \uparrow_B \downarrow_D \uparrow_C \rangle$ may contribute to the 2D-WPI signal; it is to be extended to arbitrarily large, positive values of t_{BA} and t_{CB}. Reflection in the plane $t_{DC} \quad = \quad t_{BA}$ yields the slab within which $\langle \uparrow_D \mid \uparrow_B \downarrow_A \uparrow_C \rangle$ may take nonzero values.

$t_D - t_A = t_{DC} + t_{CB} + t_{BA}$ are less than about σ. These conditions, together with the restriction to nonnegative $t_{DC} + 2t_{CB} + t_{BA}$, limit this overlap to the region shown in Fig. 6. The mirror image of this region through $t_{DC} = t_{BA}$ similarly confines $\langle \uparrow_D \downarrow_C \uparrow_A \mid \uparrow_B \rangle$.

It is apposite to recall that—despite their differing phase signatures, pulse orderings, and confining regions of time-delay space—the first eight overlaps appearing in each of Eqs. (2.38) and (2.39) are essentially the same from the dimer's point of view; each term records a contribution to the population of the one-exciton manifold resulting from the interference between an amplitude generated by the action of a single resonant electric-field interaction and another generated by an excitation-deexcitation-reexcitation process driven by three sequential interactions with resonant fields. The pulse labels attached to the participating fields don't evince themselves in a single population-generation

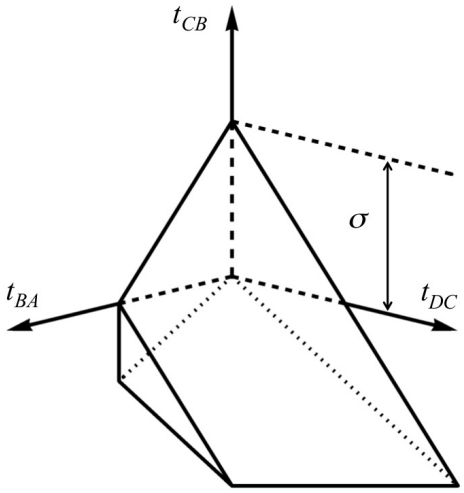

Figure 6. Delay region where $\langle\uparrow_D\downarrow_B\uparrow_A \;\; | \;\; \uparrow_C\rangle$ may take nonnegligible values. This region is quasi zero-dimensional because it shrinks towards nonexistence in all three directions as the pulses become shorter. The overlap $\langle\uparrow_D\downarrow_C\uparrow_A \;\; | \;\; \uparrow_B\rangle$ may exist only inside a region mirroring this one through the $t_{DC} = t_{BA}$ plane.

process, but only in the way the measured quadrilinear contribution to the singly-excited population varies with the experimentally specified pulse polarizations, intrapulse-pair phase shifts, and interpulse delays. The same is true among the second set of eight overlaps in Eqs. (2.38) and (2.39); each of these represents the interference population between a singly-excited wave packet generated by the action of one pulse and another driven by a three-pulse process of excitation-excitation-deexcitation.

Each of the last eight overlaps in Eqs. (2.38) and (2.39), those involving a three-pulse bra or ket whose amplitude visits the doubly-excited electronic state between the second- and third-acting pulse, can also be confined to a specified region of $\{t_{BA}, t_{DC}, t_{CB}\}$. Here we identify the delay-space volumes for the last eight quadrilinear overlaps contributing to $P^{(d)}_{one}$.

The overlap $\langle\uparrow_A\uparrow_D\downarrow_B | \uparrow_C\rangle$ is confined to negative or very short positive t_{CB}. Because it depends on pulse D acting before B, $t_{DC} + t_{CB}$ can be no larger than the

pulse duration σ. The data-organizational requirement that the temporal midpoint of C and D follow that of A and B is the only other restriction, so this overlap's admissible delay range is the quasi-3D region displayed in Fig. 7.

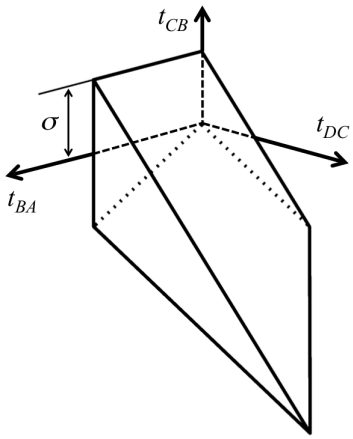

Figure 7. Region of interpulse delays where the effects of the order of pulse action alone do not prevent $\langle\uparrow_A\uparrow_D\downarrow_B \quad | \quad \uparrow_C\rangle$ from taking significant values. This delay volume extends to arbitrarily large positive t_{BA} and t_{DC}, and arbitrarily large negative t_{CB}.

The signal contribution from $\langle\uparrow_A\uparrow_D\downarrow_C|\uparrow_B\rangle$ can only be sizable in the quasi-2D delay region shown in Fig. 8. For t_{DC} must be less than σ and, as usual, $2t_{CB} + t_{BA} + t_{DC} > 0$. The condition $t_C - t_A = t_{CB} + t_{BA} > -\sigma$ imposes no additional restriction.

The three-pulse wave packet participating in $\langle\uparrow_D \mid \uparrow_B\uparrow_C\downarrow_A\rangle$ can only be formed under the stringent conditions $t_{BA} < \sigma$, $t_{CB} > -\sigma$, and $t_{CB} + t_{BA} < \sigma$, along with $2t_{CB} + t_{BA} + t_{DC} > 0$. These requirements restrict its nonnegligible contributions to the quasi one-dimensional t_{DC} range plotted in Fig. 9.

Contributions to the $P^{(d)}_{one}$ WPI signal from $\langle\uparrow_A|\uparrow_B\uparrow_C\downarrow_D\rangle$ can arise whenever $t_{CB} > -\sigma$. The condition $2t_{CB} + t_{BA} + t_{DC} > 0$ has an impact only at very small intrapulse-pair delays. This important overlap may therefore exist anywhere within the 3D delay volume portrayed in Fig. 10.

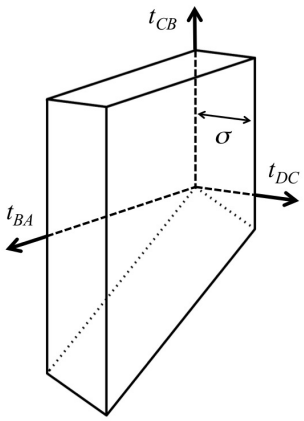

Figure 8. Delay region where $\langle \uparrow_A \uparrow_D \downarrow_C \ | \ \uparrow_B \rangle$ may be nonzero. This pulse-duration-thick slab extends to arbitrarily large positive t_{BA} and t_{CB}, and to $t_{CB} \approx -t_{BA}/2$.

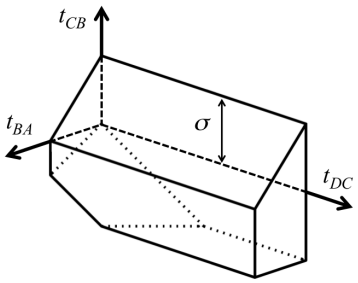

Figure 9. Narrow region of delay-space to which nonnegligible contributions from $\langle \uparrow_D | \uparrow_B \uparrow_C \downarrow_A \rangle$ are confined.

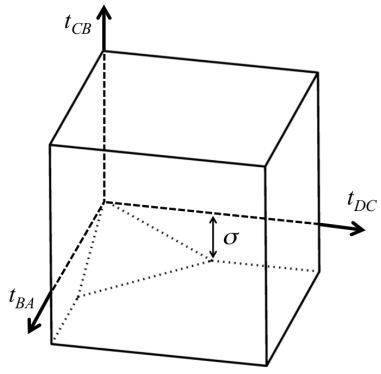

Figure 10. Volume in $\{t_{BA}, t_{DC}, t_{CB}\}$, extending to indefinitely large values of all three delays, where $\langle \uparrow_A | \uparrow_B \uparrow_C \downarrow_D \rangle$ can in principle make a signal contribution.

Because pulse D acts before A in its bra, $\langle\uparrow_D\uparrow_A\downarrow_B \mid \uparrow_C\rangle$ can only exist for very small values of all three interpulse delays. Thus $t_D - t_A = t_{DC} + t_{CB} + t_{BA} < \sigma$ combined with $2t_{CB} + t_{BA} + t_{DC} > 0$ confines nonnegligible values of this overlap to the quasi-1D region illustrated in Fig. 11. The overlap $\langle\uparrow_D\uparrow_A\downarrow_C \mid \uparrow_B\rangle$ is restricted to the same region: $t_D - t_A$ must again be less than the pulse duration, and the condition $t_C - t_A = t_{CB} + t_{BA} < \sigma$ proves to be redundant.

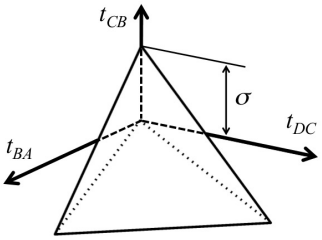

Figure 11. The small delay-range region within which the overlaps $\langle\uparrow_D\uparrow_A\downarrow_B \mid \uparrow_C\rangle$ and $\langle\uparrow_D\uparrow_A\downarrow_C \mid \uparrow_B\rangle$ are expected to contribute to $P^{(d)}_{one}$.

.

The ket in $\langle\uparrow_D \mid \uparrow_C\uparrow_B\downarrow_A\rangle$ vanishes unless both $t_C - t_A = t_{CB} + t_{BA}$ and t_{BA} alone are less than the pulse duration. Along with $2t_{CB} + t_{BA} + t_{DC} > 0$, these lead to the delay region of significance sketched in Fig. 12.

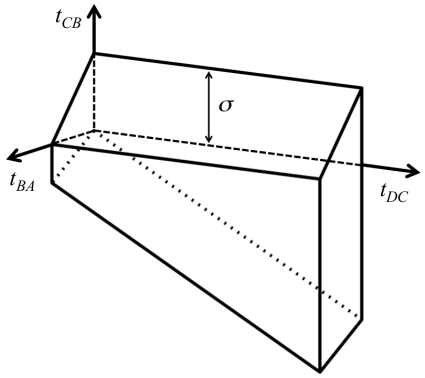

Figure 12. Interpulse-delay region, extending to arbitrarily large positive t_{DC} and negative t_{CB}, where $\langle\uparrow_D \mid \uparrow_C\uparrow_B\downarrow_A\rangle$ may give rise to significant signal.

.

It is worth recalling that outside its prescribed interpulse-delay region, a particular overlap vanishes simply because the delay combinations are inconsistent with the required order of pulse action in the participating three-pulse bra or ket. But criteria specific to the dimer's Hamiltonian, including internal molecular and host-medium nuclear degrees of freedom, will sometimes diminish the overlaps for certain delay combinations inside these regions. In multimode systems for instance, electronic dephasing driven by electronic-nuclear coupling will often severely limit the maximal intrapulse-pair delays t_{BA} and t_{DC} over which the electronic coherence on which a nonvanishing 2D-WPI signal depends can be effectively maintained. Because the B- and C-pulses are not phase-locked, signal contributions tend to be less susceptible to dynamical truncation along t_{CB}.

2.3.2.2 Doubly excited-state population

As indicated in Eq. (2.37), the quadrilinear portion of the population of the doubly-excited electronic state contributes to the 2D-WPI signal with a certain quantum yield $Q_{\bar{e}e} = Q_2 \equiv Q_{two}$. Eliminating as unmeasured the four overlaps appearing in the doubly-excited population whose optical phases are uncontrolled allows us to write P_{two} as a sum of two experimentally isolable portions,

$$P_{two}^{(s)} = 2\mathrm{Re}\big\{\langle\uparrow_A\uparrow_C|\uparrow_B\uparrow_D\rangle+\langle\uparrow_A\uparrow_C|\uparrow_D\uparrow_B\rangle+\langle\uparrow_C\uparrow_A|\uparrow_B\uparrow_D\rangle+\langle\uparrow_C\uparrow_A|\uparrow_D\uparrow_B\rangle\big\}\,, \quad (2.40)$$

and (by interchanging Cs and Ds)

$$P_{two}^{(d)} = 2\mathrm{Re}\big\{\langle\uparrow_A\uparrow_D|\uparrow_B\uparrow_C\rangle+\langle\uparrow_A\uparrow_D|\uparrow_C\uparrow_B\rangle+\langle\uparrow_D\uparrow_A|\uparrow_B\uparrow_C\rangle+\langle\uparrow_D\uparrow_A|\uparrow_C\uparrow_B\rangle\big\}\,. \quad (2.41)$$

Let's work out the region of $\{t_{BA}, t_{DC}, t_{CB}\}$ to which each of the difference-phased quadrilinear contributions to the population of the doubly-excited state, seen in Eq. (2.41), is exclusively confined. In $\langle\uparrow_A\uparrow_D|\uparrow_B\uparrow_C\rangle$, the pulses act in their nominal order (A before D and B before C), so the overlap can be nonnegligible in

a three-dimensional region of delay-space. More specifically, t_C must exceed $t_B - \sigma$, or the B-pulse could not act before C; hence $t_{CB} > -\sigma$. But the bookkeeping restriction $t_D + t_C > t_B + t_A$ also requires $t_{CB} > -\frac{1}{2}(t_{DC} + t_{BA})$, which is slightly more restrictive for tiny intrapulse-pair delays. All three interpulses delays can take arbitrarily large positive values. These are the same restrictions as apply to $\langle\uparrow_A|\uparrow_B\uparrow_C\downarrow_D\rangle$, so the relevant delay volume is identical to Fig. 10.

In the ket of $\langle\uparrow_A\uparrow_D|\uparrow_C\uparrow_B\rangle$, C-pulse action precedes B-pulse action. In order that this overlap not vanish, t_{CB} must therefore be shorter than σ. As the general condition $t_{CB} > -\frac{1}{2}(t_{DC} + t_{BA})$ also applies, nonvanishing values can only reside in the delay region plotted in Fig. 13.

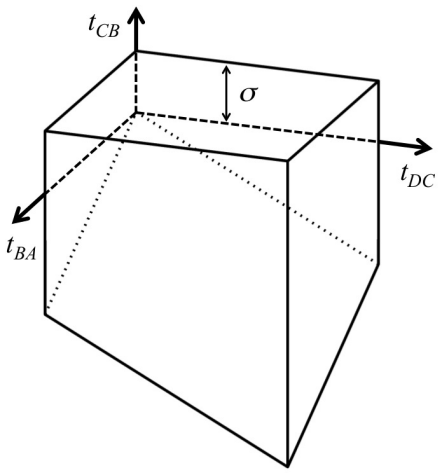

Figure 13. Region of interpulse delays where $\langle\uparrow_A\uparrow_D|\uparrow_C\uparrow_B\rangle$ can be nonzero.

The overlap $\langle\uparrow_D\uparrow_A|\uparrow_B\uparrow_C\rangle$ can only be nonnegligible when $t_D - t_A = t_{DC} + t_{CB} + t_{BA}$ is less than the pulse duration. But t_{CB} must exceed $-\frac{1}{2}(t_{BA} + t_{DC})$, so this contribution to $P^{(d)}_{two}$ can exist only in a quasi zero-dimensional region of very short interpulse delays. The same restrictions apply to $\langle\uparrow_D\uparrow_A \mid \uparrow_C\uparrow_B\rangle$, for nonnegligibility of this overlap again requires $t_{DC} + t_{CB} + t_{BA} < \sigma$. The weaker

condition $t_{CB} < \sigma$ adds no additional constraint. The resulting common delay region coincides with that illustrated in Fig. 11 for $\langle\uparrow_D\uparrow_A\downarrow_B|\uparrow_C\rangle$ and $\langle\uparrow_D\uparrow_A\downarrow_C|\uparrow_B\rangle$.

2.3.2.3 Signal isolation

As we have mentioned, it is possible to separate experimentally the sum-phased signal arising from Eqs. (2.38) and (2.40), on one hand, and the difference-phased signal from Eqs. (2.39) and (2.41), on the other. This is accomplished by combining WPI measurements $S(\varphi_{BA}, \varphi_{DC})$ having different combinations of the optical phase shifts φ_{BA} and φ_{DC}. In fact, the same "phase-cycling" methods enable the isolation of the quantum yield-weighted sum of the complex-valued quantities inside the braces of the first two or the second two of those expressions. We can illustrate the basic strategy with a simple example; more complicated schemes may have advantages in practice.

Writing the signal with particular phase shifts as

$$S(\varphi_{BA}, \varphi_{DC}) = 2\mathrm{Re}\{e^{-i\varphi_{BA}-i\varphi_{DC}}\xi_s + e^{-i\varphi_{BA}+i\varphi_{DC}}\xi_d\}\,, \tag{2.42}$$

and denoting $\xi_{s/d} = \xi'_{s/d} + i\xi''_{s/d}$, leads to distinct combinations such as

$$S(0,0) = 2(\xi'_s + \xi'_d)\,, \tag{2.43}$$

$$S(\tfrac{\pi}{2},0) = 2(\xi''_s + \xi''_d)\,, \tag{2.44}$$

$$S(0,\tfrac{\pi}{2}) = 2(\xi''_s - \xi''_d)\,, \tag{2.45}$$

and

$$S(\tfrac{\pi}{2},\tfrac{\pi}{2}) = 2(-\xi'_s + \xi'_d)\,. \tag{2.46}$$

From these we can reconstruct the sought-after quantities

$$\xi_s = \tfrac{1}{4}\{S(0,0) - S(\tfrac{\pi}{2},\tfrac{\pi}{2}) + iS(\tfrac{\pi}{2},0) + iS(0,\tfrac{\pi}{2})\}\,, \tag{2.47}$$

and

$$\xi_d = \tfrac{1}{4}\{S(0,0) + S(\tfrac{\pi}{2},\tfrac{\pi}{2}) + iS(\tfrac{\pi}{2},0) - iS(0,\tfrac{\pi}{2})\}\,. \tag{2.48}$$

2.3.3 One-, two-, and three-pulse kets

Using time-dependent perturbation theory, we now seek explicit expressions for the various multi-pulse bras and kets whose overlaps determine the 2D-WPI signal from an EET complex. Under the dimer Hamiltonian $H = T + H_{el}(\hat{Q})$ (see Eq. (2.1)) and the interaction potential $V(t)$, given in Eq. (2.27) with the pulse arrival times reckoned at $\mathbf{r} = 0$, the quantum mechanical state obeys

$$i\hbar\frac{\partial}{\partial t}|\Psi(t)\rangle = \big(H + V(t)\big)|\Psi(t)\rangle\,. \tag{2.49}$$

The initial condition is taken to be $|\Psi(t \ll t_A)\rangle = [t - t_A]|\bar{g}g\rangle|\psi_0\rangle$ (using the notation $[t] \equiv \exp\{-iHt/\hbar\}$), where $|\psi_0\rangle$ is some eigenket of the ground-state nuclear Hamiltonian, $T + \langle\bar{g}g|H_{el}(Q)|\bar{g}g\rangle$. In the interaction picture, Eq. (2.49) becomes

$$i\hbar\frac{\partial}{\partial t}|\tilde{\Psi}(t)\rangle = \tilde{V}(t)\big)|\tilde{\Psi}(t)\rangle\,, \tag{2.50}$$

with $\tilde{V}(t) = [-t + t_A]V(t)[t - t_A]$ and $|\tilde{\Psi}(t \ll t_A)\rangle = |\bar{g}g\rangle|\psi_0\rangle$.

Since the quadrilinear signal contributions all take the form of an overlap between a two-pulse bra and a two-pulse ket, or between a one-pulse bra and a three-pulse ket, it is enough to solve Eq. (2.50) through third order in the external fields:

$$\begin{aligned}|\tilde{\Psi}(t)\rangle \cong \Bigg\{1 + \frac{1}{i\hbar}\int_{-\infty}^{t} d\tau\, \tilde{V}(\tau) + \left(\frac{1}{i\hbar}\right)^2 \int_{-\infty}^{t} d\tau \int_{-\infty}^{\tau} d\bar{\tau}\, \tilde{V}(\tau)\tilde{V}(\bar{\tau}) \\ + \left(\frac{1}{i\hbar}\right)^3 \int_{-\infty}^{t} d\tau \int_{-\infty}^{\tau} d\bar{\tau} \int_{-\infty}^{\bar{\tau}} d\bar{\bar{\tau}}\, \tilde{V}(\tau)\tilde{V}(\bar{\tau})\tilde{V}(\bar{\bar{\tau}})\Bigg\}|\bar{g}g\rangle|\psi_0\rangle\,.\end{aligned} \tag{2.51}$$

This perturbative solution can be rewritten in terms of *pulse propagators* which encapsulate the effect of each finite-duration laser pulse in the instantaneous

action of a single quantum mechanical operator. Upon reversion to the Schrödinger picture, this reframing results in an equivalent solution,

$$\begin{aligned}|\Psi(t)\rangle = \big\{[t-t_A] &+ i\sum_{I=A,B,C,D}[t-t_I]P_I(t-t_I;\tau)[t_{IA}] \\ &+ i^2\sum_{IJ}[t-t_J]P_J(t-t_J;\tau)[t_{JI}]P_I(\tau+t_{JI};\bar{\tau})[t_{IA}] \\ &+ i^3\sum_{IJK}[t-t_K]P_K(t-t_K;\tau)[t_{KJ}]P_J(\tau+t_{KJ};\bar{\tau})[t_{JI}] \\ &\times P_I(\bar{\tau}+t_{JI};\bar{\bar{\tau}})[t_{IA}]\big\}|\bar{g}g\rangle|\psi_0\rangle\,, \end{aligned} \tag{2.52}$$

in which the I^{th} pulse propagator is

$$P_I(t;\tau) = \frac{E_I}{\hbar}\int_{-\infty}^{t} d\tau\, f_I(\tau)\cos(\Omega\tau+\varphi_I)\,[\,-\tau\,]\,\mathbf{e}_I\cdot\hat{\mathbf{m}}\,[\,\tau\,]\,. \tag{2.53}$$

The first argument of a pulse propagator is the upper integration limit and the second designates the variable of integration.

By extracting terms from Eq. (2.52) we can develop formulas for the wave-packet overlaps contributing to the 2D-WPI signal using any electronic basis. Portions of the two- and three-pulse sums in this expression of quadratic or cubic order in the field-strength of an individual pulse are of course irrelevant. We bypass the adiabatic electronic basis in favor of the two fixed bases, letting $|\xi\rangle$ denote either a site or an exciton state. Electronic matrix elements of the pulse propagator (2.53) can be conveniently expressed in terms of reduced pulse propagators,

$$p_I^{(\xi\bar{\xi})}(t;\tau) = \int_{-\infty}^{t}\frac{d\tau}{\sigma}\, f_I(\tau)e^{\mp i\Omega\tau}[-\tau]_{\xi\xi}[\tau]_{\bar{\xi}\bar{\xi}}\,, \tag{2.54}$$

by making a rotating-wave approximation and invoking one of the forms (2.30) or (2.36) for the dipole operator. We have written $\langle\xi|[\tau]|\bar{\xi}\rangle = [\tau]_{\xi\bar{\xi}}$ and made a significant simplification by assuming that electronic transitions between different singly excited states *in the appropriate basis* can be neglected on the timescale of

the pulse duration. The upper (lower) sign in Eq. (2.54) applies in the case of an absorptive (emissive) transition $\xi \leftarrow \bar{\xi}$ ($\bar{\xi} \rightarrow \xi$). With the same approximations and conventions, the nonvanishing elements of the overall pulse propagator (2.53) can be written as

$$\langle \xi | P_I(t;\tau) | \bar{\xi} \rangle = i F_I^{(\xi\bar{\xi})} e^{\mp i\varphi_I} p_I^{(\xi\bar{\xi})}(t;\tau)\,, \tag{2.55}$$

where $F_I^{(\xi\bar{\xi})} \equiv F_I \langle \xi | \hat{\mathbf{m}} \cdot \mathbf{e}_I | \bar{\xi} \rangle$ with $F_I = E_I \sigma / 2\hbar$.[3]

2.4 Illustrative Calculations

2.4.1 Overlaps

The stage is set for a variety of calculations of WPI signals from EET dimers and their interpretation in terms of the underlying nuclear wave-packet and energy-transfer dynamics. For illustration, we drastically pare the vast range of possible molecular parameters expressible in terms of the electronic Hamiltonian (2.1) and experimental choices by investigating the difference-phased fluorescence-detected signal from a space-fixed dimer with perpendicularly oriented monomer transition dipoles, $\mathbf{m}_a = m_a \hat{\mathbf{x}}$ and $\mathbf{m}_b = m_b \hat{\mathbf{y}}$.[4] We restrict attention to the situation in which the A, B, C, and D pulses arrive in their nominal order and are short enough that temporal pulse overlap can be neglected.[5] Consulting the relevant delay regions shown in Sections 2.3.2.1 and 2.3.2.2 confirms inspection of Eqs. (2.39) and (2.41) in showing that, under these circumstances, the quadrilinear

[3]Note that any polarization dependence of a 2D-WPI signal enters through the $F_I^{(\xi\bar{\xi})}$.

[4]The net signal from an isotropic sample of dimers with a certain internal geometry would be a weighted sum of signals from a handful of representative space-fixed orientations.

[5]Specifically, these assumptions mean that t_{CB} is positive and greater than the pulse duration. In addition, since t_{BA} and t_{DC} are defined to be positive, they also mean that pulse-overlap effects will be ignored when either is very short.

singly- and doubly-excited populations simplify to

$$P_{one}^{(d)} = 2\mathrm{Re}\big\{\langle\uparrow_A\downarrow_B\uparrow_D \mid \uparrow_C\rangle + \langle\uparrow_A\downarrow_C\uparrow_D \mid \uparrow_B\rangle + \langle\uparrow_A \mid \uparrow_B\uparrow_C\downarrow_D\rangle\big\}\,, \tag{2.56}$$

and

$$P_{two}^{(d)} = 2\mathrm{Re}\big\{\langle\uparrow_A\uparrow_D \mid \uparrow_B\uparrow_C\rangle\big\}\,. \tag{2.57}$$

We assume that the electronic excitation-transfer coupling is sufficiently weak that the site states are an appropriate electronic basis. Provided the interpulse delays are not too long, the condition $|Jt_{IK}|/\hbar \ll 1$ then ensures that the WPI signal will be at most of first order in J. It is easy to show that if all four laser pulses have the same (x or y) polarization, then first-order EET cannot contribute to the signal. To see this, we can arrange the site-state labels as in Fig. 14, so the

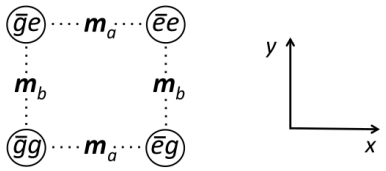

Figure 14. Site-state labels arranged so that each pair is separated in the direction of the monomer transition moment that connects them.

directions between them are those of the connecting transition moments. Four x-polarized pulses combined with a single EET-driven amplitude transfer can then be seen to generate one- and three-pulse wave packets in *different* electronic states, as illustrated in Fig. 15; their overlaps vanish and hence make no contribution to P_{one}. Four x-pulses are similarly unable to contribute to P_{two} linearly in J, as Fig. 16 reveals.

As an example of a polarization combination that produces a nonzero difference-phased interference signal of first order in J from our oriented model dimer (and no signal in the absence of energy transfer), we consider the case

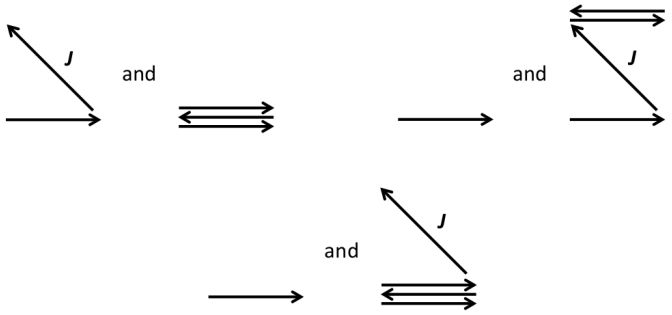

Figure 15. Three combinations of one- and three-pulse states formed by all x-polarized pulses, with one state or the other being linear in J. Each of the three pairs forms a vanishing wave-packet overlap.

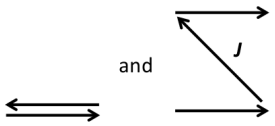

Figure 16. Illustration that a pair of two-pulse wave packets, one of them linear in J, formed by four x-polarized pulses produce a vanishing overlap.

$\mathbf{e}_A = \hat{\mathbf{y}}$, $\mathbf{e}_B = \mathbf{e}_C = \mathbf{e}_D = \hat{\mathbf{x}}$. The sequences of pulse- and EET-driven electronic transitions making up the quadrilinear overlaps of $P^{(d)}_{one}$ are sketched in Fig. 17, while those responsible for $P^{(d)}_{two}$ are illustrated in Fig. 18.[6]

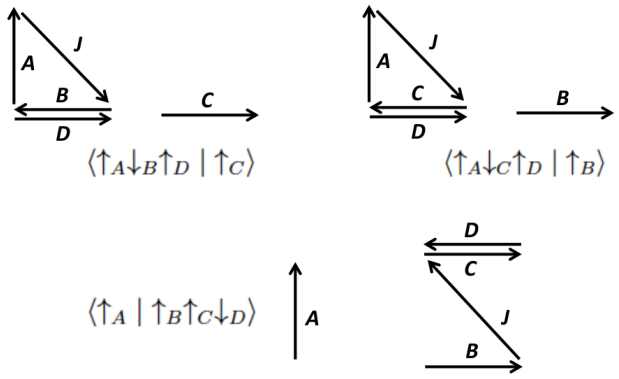

Figure 17. Sequence of electronic transitions under $A_y B_x C_x D_x$ polarization in each pair of states whose overlap contributes to $P^{(d)}_{one}$ at first order in J.

[6] 2D interferograms from $\langle\uparrow_A \quad | \quad \uparrow_B\uparrow_C\downarrow_D\rangle$ alone in model dimers akin to that considered here, under the same polarization conditions—but with arbitrarily abrupt laser pulses—were the subject of earlier work by Cina, Kilin, and Humble [9].

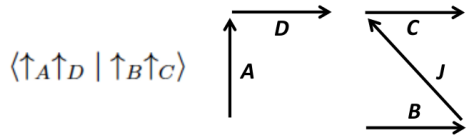

Figure 18. Electronic transitions under $A_y B_x C_x D_x$ polarization in the two states whose overlap determines $P_{two}^{(d)}$ at first order in J.

In the simple version of the dimer Hamiltonian (2.1) used here, each monomer will be assigned a single internal vibrational mode, so the kinetic energy is

$$T = \frac{p_a^2}{2m} + \frac{p_b^2}{2m}\,, \tag{2.58}$$

and the site-state potential functions are

$$V_{\bar{g}g}(q_a, q_b) = \frac{m\omega^2}{2}(q_a^2 + q_b^2)\,, \tag{2.59}$$

$$V_{\bar{e}g}(q_a, q_b) = \epsilon_{\bar{e}g} + \frac{m\omega^2}{2}\big((q_a - d)^2 + q_b^2\big)\,, \tag{2.60}$$

$$V_{\bar{g}e}(q_a, q_b) = \epsilon_{\bar{g}e} + \frac{m\omega^2}{2}\big(q_a^2 + (q_b - d)^2\big)\,, \tag{2.61}$$

and

$$V_{\bar{e}e}(q_a, q_b) = \epsilon_{\bar{e}e} + \frac{m\omega^2}{2}\big((q_a - d)^2 + (q_b - d)^2\big)\,. \tag{2.62}$$

We focus on a case of "downhill" energy transfer with $\epsilon_{\bar{e}g} - \epsilon_{\bar{g}e} = m\omega^2 d^2$, so the intersection line between the singly-excited site-state potentials passes through the minimum point $(q_a, q_b) = (d, 0)$ of the higher-energy, "donor-state" potential, as shown in Fig. 19. We pick a moderate Franck-Condon displacement $d = q_{rms}$, where $q_{rms} = \sqrt{\hbar/2m\omega}$. The condition (2.25) for weak energy-transfer coupling underlying our choice of the site basis here implies $|J| \ll m\omega^2 d^2 = \hbar\omega/2$. We treat J as a constant, dismissing any nuclear-coordinate dependence.

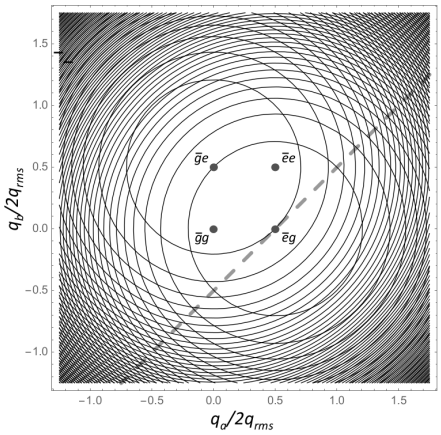

Figure 19. Plot of $V_{\bar{e}g}$ and $V_{\bar{g}e}$ with their minima labeled. Dashed diagonal is the line of intersection between $V_{\bar{e}g}$ and $V_{\bar{g}e}$ for the chosen bare site-energy difference. Minimum points of $V_{\bar{g}g}$ and $V_{\bar{e}e}$ are also shown.

The weak-coupling condition just invoked ensures $|Jt_{IK}/\hbar| \ll \omega t_{IK}/2$ in the present instance. So the effect of energy transfer is small and can be treated perturbatively through first order in J, as we wish to do, over interpulse delays up to several vibrational periods in length. Other than assuming that weak coupling is operative and stating the sign of J, we need not specify it any more precisely. In the WPI signal calculations presented below the sign of J is taken positive; all the interferograms would change sign if it were instead made negative.

From Eq. (2.52) we extract formulas for each of the wave packets appearing in Eqs. (2.56) and (2.57). We find, for instance,

$$|\uparrow_C\rangle = ie^{-i\varphi_C} \sum_{\xi,\xi_1=\bar{e}g,\bar{g}e} |\xi\rangle F_C^{(\xi_1\,\bar{g}g)}[t-t_C]_{\xi\,\xi_1}\, p_C^{(\xi_1\,\bar{g}g)}[t_{CA}]_{\bar{g}g\,\bar{g}g}|\psi_0\rangle\,, \tag{2.63}$$

and

$$\begin{aligned}|\uparrow_A\downarrow_B\uparrow_D\rangle = -ie^{i\varphi_{BA}-i\varphi_D} \sum_{\xi,\xi_2,\xi_3,\xi_4=\bar{e}g,\bar{g}e} |\xi\rangle F_D^{(\xi_2\,\bar{g}g)} F_B^{(\bar{g}g\,\xi_3)} F_A^{(\xi_4\,\bar{g}g)} \\ \times [t-t_D]_{\xi\,\xi_2}\, p_D^{(\xi_2\,\bar{g}g)}[t_{DB}]_{\bar{g}g\,\bar{g}g}\, p_B^{(\bar{g}g\,\xi_3)}[t_{BA}]_{\xi_3\,\xi_4}\, p_A^{(\xi_4\,\bar{g}g)}|\psi_0\rangle\,.\end{aligned} \tag{2.64}$$

Because temporal pulse overlap is being neglected, we have replaced the first argument of each reduced pulse propagator by infinity and written $p_I^{(\xi\bar{\xi})}(\infty;\tau) = p_I^{(\xi\bar{\xi})}$.

The "observation time" t disappears when we take the inner product between the wave packets (2.63) and (2.64) and sum over the state index ξ. Since unitary evolution of both wave packets, including subsequent energy transfer, does not affect their contribution to the singly-excited population, the resulting overlap can be formally evalutated at $t = t_D$:

$$\langle\uparrow_A\downarrow_B\uparrow_D \mid \uparrow_C\rangle = -e^{-i\varphi_{BA}+i\varphi_{DC}} \sum_{\xi_1\,\xi_2\,\xi_3\,\xi_4} F_A^{(\bar{g}g\,\xi_4)} F_B^{(\xi_3\,\bar{g}g)} F_D^{(\bar{g}g\,\xi_2)} F_C^{(\xi_1\,\bar{g}g)} \langle\psi_0| \tag{2.65}$$

$$\times\, p_A^{(\bar{g}g\xi_4)}[-t_{BA}]_{\xi_4\xi_3} p_B^{(\xi_3\bar{g}g)}[-t_{DB}]_{\bar{g}g\,\bar{g}g} p_D^{(\bar{g}g\xi_2)}[t_{DC}]_{\xi_2\xi_1} p_C^{(\xi_1\bar{g}g)}[t_{CA}]_{\bar{g}g\,\bar{g}g}|\psi_0\rangle.$$

The overlap (2.65) serves as a template for the others appearing in Eqs. (2.56) and (2.57), which can be written out directly:

$$\langle\uparrow_A\downarrow_C\uparrow_D \mid \uparrow_B\rangle = -e^{-i\varphi_{BA}+i\varphi_{DC}} \sum_{\xi_1\,\xi_2\,\xi_3\,\xi_4} F_A^{(\bar{g}g\,\xi_4)} F_C^{(\xi_3\,\bar{g}g)} F_D^{(\bar{g}g\,\xi_2)} F_B^{(\xi_1\,\bar{g}g)} \langle\psi_0| \tag{2.66}$$

$$\times\, p_A^{(\bar{g}g\xi_4)}[-t_{CA}]_{\xi_4\xi_3} p_C^{(\xi_3\bar{g}g)}[-t_{DC}]_{\bar{g}g\,\bar{g}g} p_D^{(\bar{g}g\xi_2)}[t_{DB}]_{\xi_2\xi_1} p_B^{(\xi_1\bar{g}g)}[t_{BA}]_{\bar{g}g\,\bar{g}g}|\psi_0\rangle\,,$$

$$\langle\uparrow_A \mid \uparrow_B\uparrow_C\downarrow_D\rangle = -e^{-i\varphi_{BA}+i\varphi_{DC}} \sum_{\xi_1\,\xi_2\,\xi_3\,\xi_4} F_A^{(\bar{g}g\,\xi_1)} F_D^{(\xi_2\,\bar{e}e)} F_C^{(\bar{e}e\,\xi_3)} F_B^{(\xi_4\,\bar{g}g)} \langle\psi_0| \tag{2.67}$$

$$\times\, p_A^{(\bar{g}g\,\xi_1)}[-t_{DA}]_{\xi_1\xi_2} p_D^{(\xi_2\,\bar{e}e)}[t_{DC}]_{\bar{e}e\,\bar{e}e} p_C^{(\bar{e}e\,\xi_3)}[t_{CB}]_{\xi_3\xi_4} p_B^{(\xi_4\,\bar{g}g)}[t_{BA}]_{\bar{g}g\,\bar{g}g}|\psi_0\rangle\,,$$

and

$$\langle\uparrow_A\uparrow_D \mid \uparrow_B\uparrow_C\rangle = e^{-i\varphi_{BA}+i\varphi_{DC}} \sum_{\xi_1\,\xi_2\,\xi_3\,\xi_4} F_A^{(\bar{g}g\,\xi_1)} F_D^{(\xi_2\,\bar{e}e)} F_C^{(\bar{e}e\,\xi_3)} F_B^{(\xi_4\,\bar{g}g)} \langle\psi_0| \tag{2.68}$$

$$\times\, p_A^{(\bar{g}g\,\xi_1)}[-t_{DA}]_{\xi_1\xi_2} p_D^{(\xi_2\,\bar{e}e)}[t_{DC}]_{\bar{e}e\,\bar{e}e} p_C^{(\bar{e}e\,\xi_3)}[t_{CB}]_{\xi_3\xi_4} p_B^{(\xi_4\,\bar{g}g)}[t_{BA}]_{\bar{g}g\,\bar{g}g}|\psi_0\rangle\,.$$

It is to be noted that $\langle\uparrow_A\uparrow_D \mid \uparrow_B\uparrow_C\rangle$, which describes excited-state absorption from the singly- to the doubly-excited electronic manifold, equals minus $\langle\uparrow_A \mid \uparrow_B\uparrow_C\downarrow_D\rangle$,

which accounts for "bleaching" of the singly-excited states in the same process. The degree to which the contributions of these overlaps cancel in the WPI signal depends on the relative fluorescence quantum yield following double and single excitation.

Each of the overlaps (2.65) - (2.68) contains two periods of free molecular evolution in the singly-excited manifold of the form $[t_{KL}]_{\xi\,\bar{\xi}}$ during which site-to-site electronic excitation transfer may not or must occur, according to whether ξ is or isn't equal to $\bar{\xi}$; these free molecular-evolution operators consist exclusively of terms of even or odd powers of J, respectively. Thus, an expansion of the signal through first order in J could be found by collecting terms of zeroth and first order in Eqs. (2.65) - (2.68). But the task is simplified when we consider the chosen dimer orientation and the polarization directions. For the y-polarized A-pulse we have

$$\begin{aligned} F_A^{(\bar{g}g\,\bar{e}g)} &= 0\,; \\ F_A^{(\bar{g}g\,\bar{g}e)} &= m_b F_A \end{aligned} \tag{2.69}$$

(see below Eq. (2.55)). For $I = B, C,$ and D, which are x-polarized,

$$\begin{aligned} F_I^{(\bar{g}g\,\xi)} &= \delta_{\xi\,\bar{e}g} m_a F_I\,, \\ F_I^{(\bar{e}g\,\xi)} &= \delta_{\xi\,\bar{g}g} m_a F_I\,, \\ F_I^{(\bar{g}e\,\xi)} &= \delta_{\xi\,\bar{e}e} m_a F_I\,, \\ F_I^{(\bar{e}e\,\xi)} &= \delta_{\xi\,\bar{g}e} m_a F_I\,. \end{aligned} \tag{2.70}$$

Under these circumstances, net transfer occurs during one particular evolution interval in each of the contributing overlaps. All of them vanish at zeroth order

in J, and the sought-after first-order overlaps reduce to

$$\langle\uparrow_A\downarrow_B\uparrow_D \mid \uparrow_C\rangle = -e^{-i\varphi_{BA}+i\varphi_{DC}}\mathcal{F}\langle\psi_0|p_A^{(\bar{g}g\,\bar{g}e)}[-t_{BA}]^{(1)}_{\bar{g}e\,\bar{e}g}p_B^{(\bar{e}g\,\bar{g}g)} \times [-t_{DB}]_{\bar{g}g\,\bar{g}g}p_D^{(\bar{g}g\,\bar{e}g)}[t_{DC}]^{(0)}_{\bar{e}g\,\bar{e}g}p_C^{(\bar{e}g\,\bar{g}g)}[t_{CA}]_{\bar{g}g\,\bar{g}g}|\psi_0\rangle\,, \tag{2.71}$$

$$\langle\uparrow_A\downarrow_C\uparrow_D \mid \uparrow_B\rangle = -e^{-i\varphi_{BA}+i\varphi_{DC}}\mathcal{F}\langle\psi_0|p_A^{(\bar{g}g\,\bar{g}e)}[-t_{CA}]^{(1)}_{\bar{g}e\,\bar{e}g}p_C^{(\bar{e}g\,\bar{g}g)} \times [-t_{DC}]_{\bar{g}g\,\bar{g}g}p_D^{(\bar{g}g\,\bar{e}g)}[t_{DB}]^{(0)}_{\bar{e}g\,\bar{e}g}p_B^{(\bar{e}g\,\bar{g}g)}[t_{BA}]_{\bar{g}g\,\bar{g}g}|\psi_0\rangle\,, \tag{2.72}$$

$$\langle\uparrow_A \mid \uparrow_B\uparrow_C\downarrow_D\rangle = -e^{-i\varphi_{BA}+i\varphi_{DC}}\mathcal{F}\langle\psi_0|p_A^{(\bar{g}g\,\bar{g}e)}[-t_{DA}]^{(0)}_{\bar{g}e\,\bar{g}e}p_D^{(\bar{g}e\,\bar{e}e)} \times [t_{DC}]_{\bar{e}e\,\bar{e}e}p_C^{(\bar{e}e\,\bar{g}e)}[t_{CB}]^{(1)}_{\bar{g}e\,\bar{e}g}p_B^{(\bar{e}g\,\bar{g}g)}[t_{BA}]_{\bar{g}g\,\bar{g}g}|\psi_0\rangle\,, \tag{2.73}$$

and

$$\langle\uparrow_A\uparrow_D \mid \uparrow_B\uparrow_C\rangle = e^{-i\varphi_{BA}+i\varphi_{DC}}\mathcal{F}\langle\psi_0|p_A^{(\bar{g}g\,\bar{g}e)}[-t_{DA}]^{(0)}_{\bar{g}e\,\bar{g}e}p_D^{(\bar{g}e\,\bar{e}e)} \times [t_{DC}]_{\bar{e}e\,\bar{e}e}p_C^{(\bar{e}e\,\bar{g}e)}[t_{CB}]^{(1)}_{\bar{g}e\,\bar{e}g}p_B^{(\bar{e}g\,\bar{g}g)}[t_{BA}]_{\bar{g}g\,\bar{g}g}|\psi_0\rangle\,, \tag{2.74}$$

where $\mathcal{F} = m_a^3 m_b F_A F_B F_C F_D$. Free-evolution operators of zeroth and first order in J within the singly excited manifold are marked with superscripts. More explicitly, $[t] \cong [t]^{(0)} + [t]^{(1)}$, where $[t]^{(0)} = \exp\{\{-iH^{(0)}t/\hbar\}\}$ (with $H^{(0)}$ being $T + H_{el}(Q)$ in which J is set to zero) and, by first-order time-dependent perturbation theory,

$$[t]^{(1)} = -\frac{iJ}{\hbar}\int_0^t d\tau\,[t-\tau]^{(0)}\big(|\bar{e}g\rangle\langle\bar{g}e| + |\bar{g}e\rangle\langle\bar{e}g|\big)[\tau]^{(0)}\,. \tag{2.75}$$

In the calculated interferograms shown here, the common envelope function for all four pulses is taken to be $f(t) = \exp\{-t^2/2\sigma^2\}$ with $\sigma = 0.09(2\pi/\omega) \equiv 0.09\tau_v$. From Eq. (2.54), the reduced pulse propagators,

$$p^{(\xi\bar{\xi})} = \int_{-\infty}^{\infty}\frac{d\tau}{\sigma}\,e^{-\tau^2/2\sigma^2}e^{\mp i\Omega\tau}[-\tau]^{(0)}_{\xi\xi}[\tau]^{(0)}_{\bar{\xi}\bar{\xi}}\,, \tag{2.76}$$

are seen to become proportional to Fourier components of the envelope evaluated at the offset between Ω and the $\bar{\xi}$-to-ξ vibronic transition frequency.

In order to calculate the WPI signal from the excited-state populations, we have to specify the relative fluorescence quantum yield from the singly- and doubly-excited manifolds. We set $Q_{one} = 1$ and illustrate several possibilities by taking $Q_{two} = 0, 1,$ or 2. The first choice would be appropriate if some rapid, nonradiative process were to shut off fluorescence from doubly-excited dimers; the second applies if the dimer obeys "Kasha's rule" by undergoing quick internal conversion to the singly-excited manifold prior to radiative decay; and the last value would be applicable if simultaneously excited monomers within a dimer decay by emitting one photon each.

We have not yet stated a value for the bare electronic energy $\epsilon_{\bar{e}e}$ seen in Eq. (2.62). One could imagine that it is simply the sum of the individual excitation energies, $\epsilon_{\bar{e}g}$ and $\epsilon_{\bar{g}e}$, and some of our calculations will make this assumption. It's also possible, however, that an "exciton shift" alters the excitation energy for one monomer when the other is already excited, perhaps lowering it due to stronger dispersion interactions between two excited monomers than between one excited and another unexcited species. We'll entertain the possible effect of a nonvanishing exciton shift by considering a particular choice, $\epsilon_{\bar{e}e} = \epsilon_{\bar{e}g} + \epsilon_{\bar{g}e} - \hbar\omega/2$. Due to the phase-sensitive nature of 2D WPI, even this small shift will be seen to influence nonnegligibly the form of the calculated interferograms. A significantly stronger exciton shift might even move singly-to-doubly-excited transitions outside the power spectrum of the laser pulses, driving the relevant matrix elements of $p_C^{(\bar{e}e\,\bar{g}e)}$ and $p_D^{(\bar{g}e\,\bar{e}e)}$ effectively to zero in Eqs. (2.73) and (2.74) and eliminating contributions from those overlaps. This consequence of a strong exciton shift could be similar to that of a Kasha's-rule cancelation between the same two overlaps.

Shown below are the real part and the absolute value of each of the contributing overlaps as well as those of the quantum yield-weighted sum of overlaps ξ_d determining the measured 2D signal (see Sect. 2.3.2.3), calculated under the conditions just described. All the time-evolution operators and pulse propagators are represented as matrices in a two-dimensional harmonic oscillator basis. The waiting time is set to half a vibrational period ($t_{CB} = \tau_v/2$) to allow optically generated excited-state wave packets at most one pass through the $V_{\bar{e}g} = V_{\bar{g}e}$ intersection during this interval. The overlaps are multiplied by $\exp\{i\Omega(t_{DC} - t_{BA})\}$ to eliminate optical-frequency oscillations and by $\exp\{i\varphi_{BA} - i\varphi_{DC}\}$ to specify the $\varphi_{BA} = \varphi_{DC} = 0$ case. All overlaps and signals are plotted in units of $|J|/\hbar\omega$ times $m_a^3 m_b F_A F_B F_C F_D$.

Figure 20 plots $\langle\uparrow_A\downarrow_B\uparrow_D|\uparrow_C\rangle$ and $\langle\uparrow_A\downarrow_C\uparrow_D|\uparrow_B\rangle$, which appear in $P_{one}^{(d)}$. Since the three-pulse bra in each of these overlaps does not access the doubly excited state, they would be impervious to the presence of an exciton shift. In Fig. 21 is seen the overlap $\langle\uparrow_A \mid \uparrow_B\uparrow_C\downarrow_D\rangle$, also appearing in $P_{one}^{(d)}$, whose three-pulse ket involves $\bar{e}e$-state wave-packet dynamics between t_C and t_D. This overlap will be recalculated below with an exciton shift included. It is not necessary to make a separate plot for the overlap $\langle\uparrow_A\uparrow_D \mid \uparrow_B\uparrow_C\rangle$ determining $P_{two}^{(d)}$, as it equals minus $\langle\uparrow_A|\uparrow_B\uparrow_C\downarrow_D\rangle$ without or with an exciton shift.

For the model dimer under study, it is possible to understand many key features of the delay dependence of the overlaps shown in Figs. 20 and 21 in terms of the underlying energy-transfer and nuclear wave-packet dynamics. The vanishing of $\langle\uparrow_A\downarrow_B\uparrow_D|\uparrow_C\rangle$ for $t_{BA} = 2n\tau_v$ is a striking consequence of the half-quantum offset between $\epsilon_{\bar{e}g}$ and $\epsilon_{\bar{g}e}$. We see from Eq. (2.71) that first-order energy transfer must occur during t_{BA} for this overlap to be nonzero. When $t_{BA} = 2n\tau_v$, this EET event

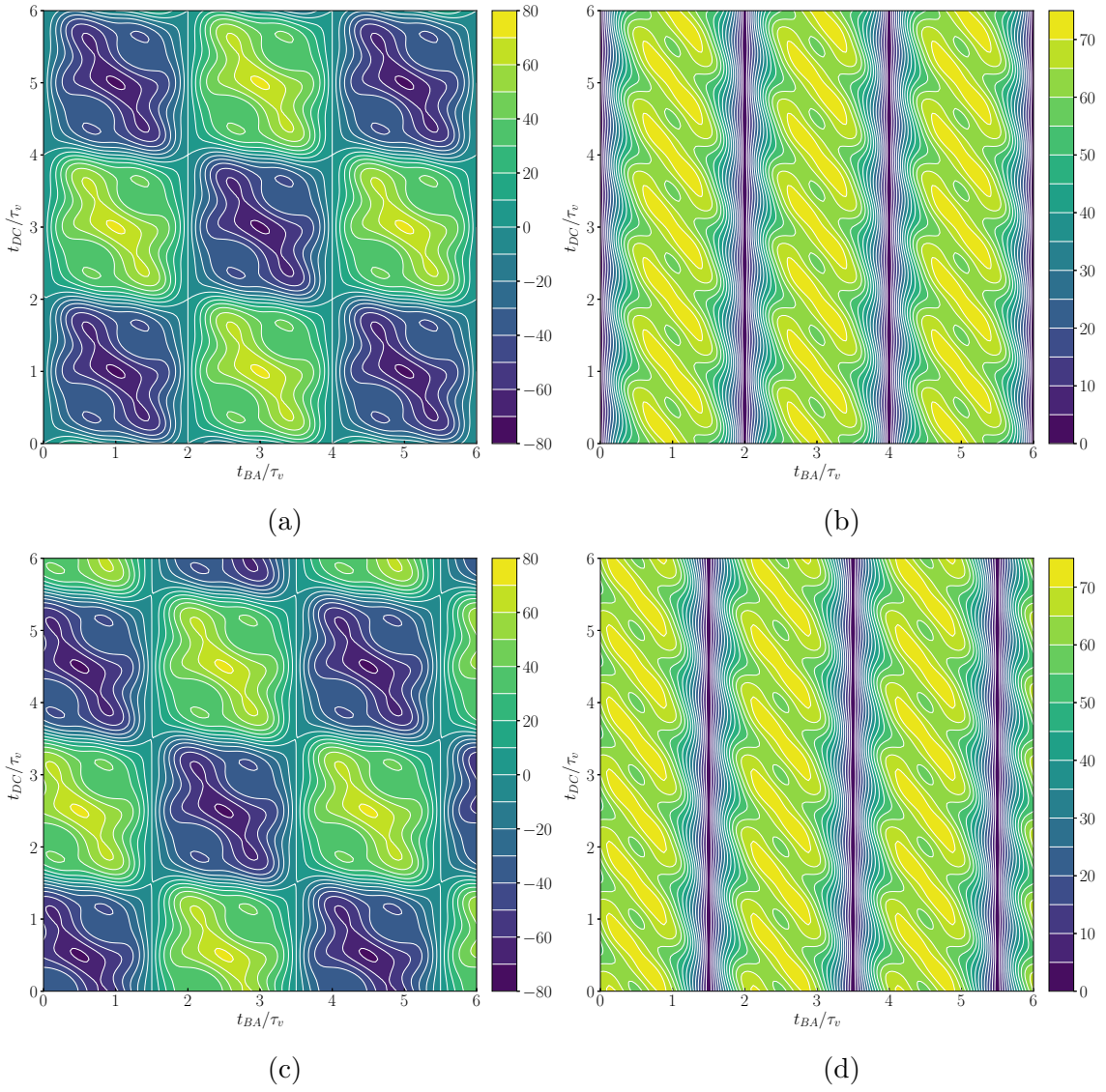

Figure 20. The two upper panels are the real part (left) and absolute value (right) of $\langle\uparrow_A\downarrow_B\uparrow_D \mid \uparrow_C\rangle$. Intrapulse-pair delays are in vibrational periods $\tau_v = 2\pi/\omega$, and the waiting time is fixed at $t_{CB} = \tau_v/2$. Lower panels are for $\langle\uparrow_A\downarrow_C\uparrow_D \,|\uparrow_B\rangle$. Neither of these overlaps would be affected by an "exciton shift" in the singly-to-doubly-excited transition energy.

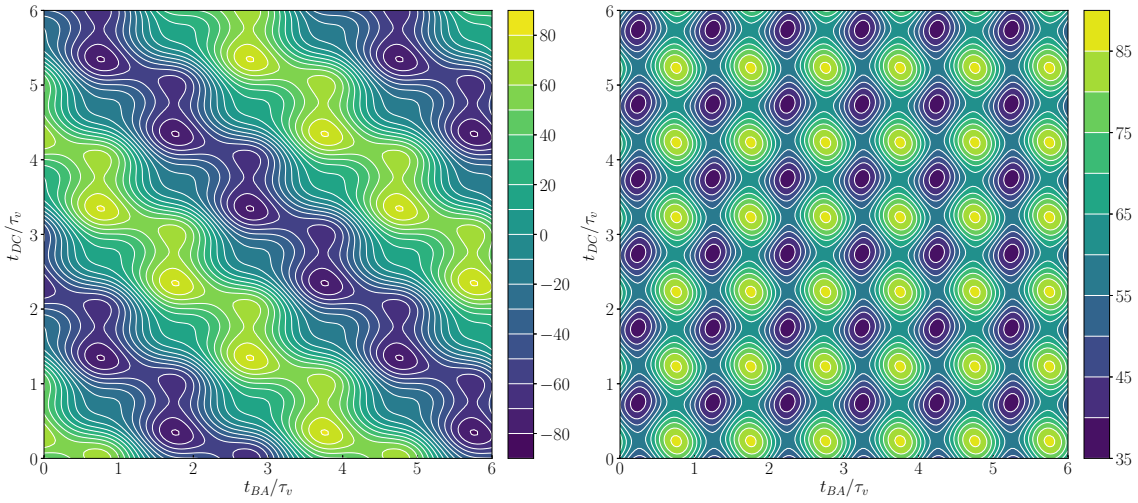

(a) (b)

Figure 21. The left panel gives $\mathrm{Re}\{\langle\uparrow_A \mid \uparrow_B\uparrow_C\downarrow_D\rangle\}$ (or $-\mathrm{Re}\{\langle\uparrow_A\uparrow_D \mid \uparrow_B\uparrow_C\rangle\}$) for the model dimer without an exciton shift, and the right panel shows its absolute value.

could take place during any $2\tau_v$-long interval, so we can write

$$\begin{aligned}[-2n\tau_v]^{(1)}_{\bar{g}e\,\bar{e}g} &= [-2\tau_v]^{(1)}_{\bar{g}e\,\bar{e}g}\,[-2(n-1)\tau_v]^{(0)}_{\bar{e}g\,\bar{e}g} \\ &\quad + [-2\tau_v]^{(0)}_{\bar{g}e\,\bar{g}e}\,[-2\tau_v]^{(1)}_{\bar{g}e\,\bar{e}g}\,[-2(n-2)\tau_v]^{(0)}_{\bar{e}g\,\bar{e}g} \\ &\quad + \cdots + [-2(n-1)\tau_v]^{(0)}_{\bar{g}e\,\bar{g}e}\,[-2\tau_v]^{(1)}_{\bar{g}e\,\bar{e}g}\ . \end{aligned} \tag{2.77}$$

We can break up the first order factors as

$$\begin{aligned}[-2\tau_v]^{(1)}_{\bar{g}e\,\bar{e}g} &= -\frac{iJ}{\hbar}\int_0^{-2\tau_v} d\tau\,[-2\tau_v-\tau]^{(0)}_{\bar{g}e\,\bar{g}e}\,[\tau]^{(0)}_{\bar{e}g\,\bar{e}g} \\ &= -\frac{iJ}{\hbar}\int_0^{-\tau_v} d\tau\,[-2\tau_v-\tau]^{(0)}_{\bar{g}e\,\bar{g}e}\,[\tau]^{(0)}_{\bar{e}g\,\bar{e}g} \\ &\quad -\frac{iJ}{\hbar}\int_{-\tau_v}^{-2\tau_v} d\tau\,[-2\tau_v-\tau]^{(0)}_{\bar{g}e\,\bar{g}e}\,[\tau]^{(0)}_{\bar{e}g\,\bar{e}g} \\ &= -\frac{iJ}{\hbar}\int_0^{-\tau_v} d\tau\,[-2\tau_v-\tau]^{(0)}_{\bar{g}e\,\bar{g}e}\,[\tau]^{(0)}_{\bar{e}g\,\bar{e}g} \\ &\quad -\frac{iJ}{\hbar}e^{i\frac{\tau_v}{\hbar}(\epsilon_{\bar{e}g}-\epsilon_{\bar{g}e})}\int_0^{-\tau_v} d\bar{\tau}\,[-2\tau_v-\bar{\tau}]^{(0)}_{\bar{g}e\,\bar{g}e}\,[\bar{\tau}]^{(0)}_{\bar{e}g\,\bar{e}g} = 0\,; \end{aligned} \tag{2.78}$$

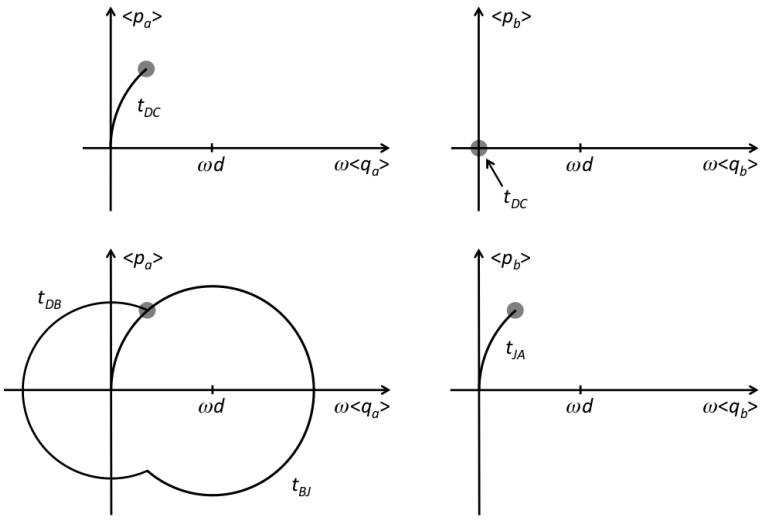

Figure 22. The upper two panels show approximate phase-space paths for $|\quad\uparrow_C\rangle$ while the lower two show those for $|\uparrow_A\downarrow_B\uparrow_D\rangle$, in the case $t_{CB} = \tau_v/2$.

the nuclear wave packet generated in the $\bar{e}g$-state by EET during the second half of each $2\tau_v$-interval is opposite in sign from that formed during the first half, giving rise to complete destructive interference and no net amplitude transfer. The first-order evolution operator in Eq. (2.77) therefore vanishes entirely.

A necessary condition for $\langle\uparrow_A\downarrow_B\uparrow_D\,|\,\uparrow_C\rangle$ to have a sizable value is that the overlapped one- and three-pulse wave packets reside in similar regions of phase space. That is to say, the expectation values of their coordinate and momentum must nearly coincide, for both a and b modes. Schematic diagrams for both modes of both wave packets are sketched in Fig. 22. The A pulse excites the dimer to the $\bar{g}e$ state, where b-mode motion ensues. The local splitting between the two site-states becomes larger than its Franck-Condon value of $\hbar\omega/2$ at positive q_b, so the most likely elapsed times before an energy-transfer transition to $\bar{e}g$, denoted by t_{JA}, will be integer multiples of τ_v. The condition for a-mode coincidence can then be

written

$$\omega d\big(1-e^{-i\omega t_{DC}}\big) = \omega d\big(1-e^{-i\omega t_{BJ}}\big)e^{-i\omega t_{DB}} \approx \omega d\big(1-e^{-i\omega t_{BA}}\big)e^{-i\omega t_{DC}-i\omega\frac{\tau_v}{2}}\,, \tag{2.79}$$

which reduces to $t_{DC}+t_{BA}=m\tau_v$ and rationalizes the slanted form of the peaks in the upper right panel of Fig. 20. The b-mode coincidence requirement $0=\omega d(1-\exp\{-i\omega t_{JA}\})$ simply reinforces the condition $t_{JA}\approx n\tau_v$.

The exciton shift affects the two contributing overlaps which involve wave-packet motion in the doubly excited electronic state. $\langle\uparrow_A \mid \uparrow_B\uparrow_C\downarrow_D\rangle$ with the chosen exciton shift (see p. 39) is illustrated in Fig. 23. $\langle\uparrow_A\uparrow_D \mid \uparrow_B\uparrow_C\rangle$ has the opposite sign. The complex-valued overlap itself changes drastically between Fig. 21 and Fig. 23, illustrating the sensitivity of the overlaps determining the 2D-WPI signal to small changes in the relative phase of the interfering wave packets. The absolute value of the overlap changes only slightly as a result of this small shift, reflecting minute changes in the location of the dimer's singly-to-doubly-excited vibronic transition energies within the power spectrum of the pulses.

The bra and ket trajectories whose final-point coincidence determines the delay combinations of maximal overlap visible in the right panels of Figs. 21 and 23 are drawn schematically in Fig. 24. The requirement for agreement between the two a-mode ending points can be written

$$0=\omega d\big[\big(1-e^{-i\omega t_{JB}}\big)e^{-i\omega(t_{CB}-t_{JB})}-1\big]e^{-i\omega t_{DC}}+\omega d\,, \tag{2.80}$$

where $t_{CB} = \tau_v/2$ and t_{JB} estimates the delay between B-pulse arrival and amplitude transfer by EET from $\bar{e}g$ to $\bar{g}e$. This requirement reduces to $t_{DC} = k\tau_v + t_{JB}$. The corresponding condition for the b-mode is

$$\omega d\big(1-e^{-i\omega t_{DA}}\big) = \omega d\big(1-e^{-i\omega t_{DJ}}\big)\,, \tag{2.81}$$

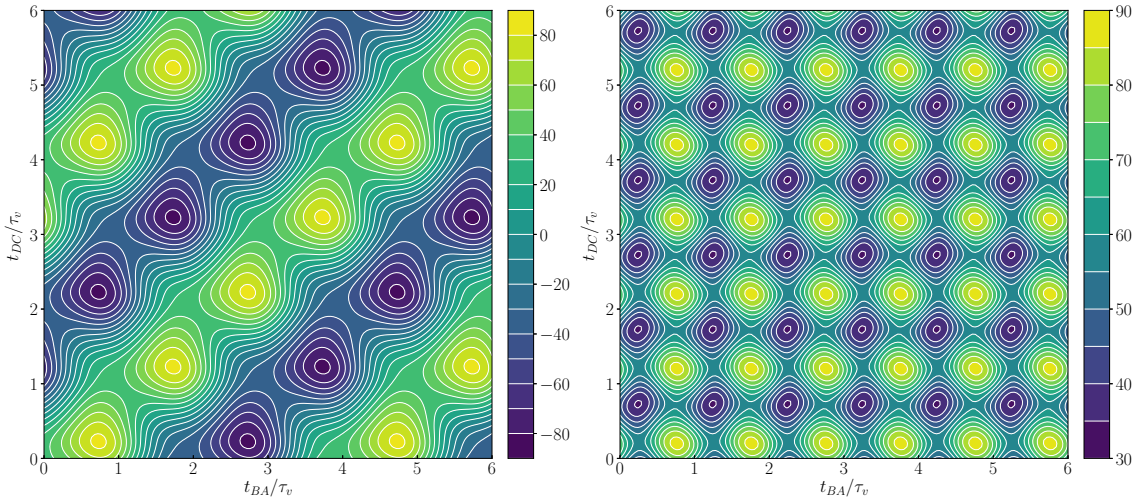

Figure 23. The left panel shows $\mathrm{Re}\{\langle\uparrow_A \mid \uparrow_B\uparrow_C\downarrow_D\rangle\}$ (or $-\mathrm{Re}\{\langle\uparrow_A\uparrow_D \mid \uparrow_B\uparrow_C\rangle\}$) for the model dimer *with* an exciton shift, and the right panel plots its absolute value.

or $t_{BA} = l\tau_v - t_{JB}$. Since $t_{JB} \approx \tau_v/4$ in the present situation, the coincidence requirements predict peaks at $(t_{BA}, t_{DC}) \approx (l - \frac{1}{4}, k + \frac{1}{4})\tau_v$, just as seen in the absolute-value plots.

It is interesting that, in the weak EET-coupling situation illustrated here, purely classical descriptions of intramolecular nuclear motion provide reliable explanations for the delay-dependence of 2D WPI signal intensity despite the fact that the spatial range of motion is similar to the width of the nuclear wave packets.

Despite the close similarity between the right-hand panels of Figs. 21 and 23, the phase dependence exhibited on the left is quite different. The residual

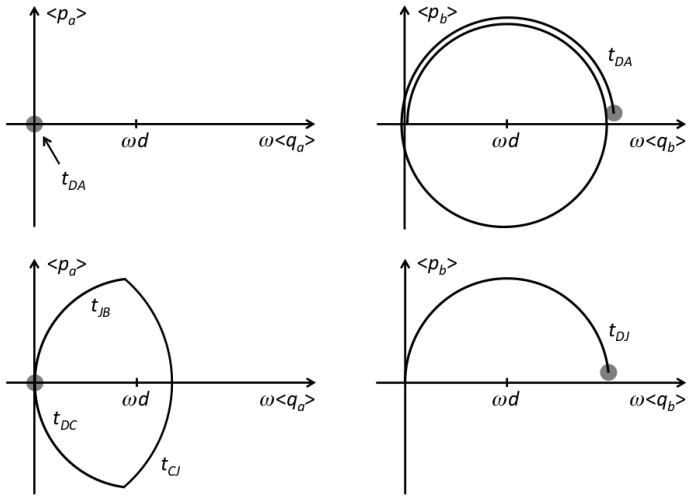

Figure 24. The top (bottom) panels show momentum-versus-position expectation-value trajectories for the bra (ket) of $\langle\uparrow_A \quad | \quad \uparrow_B\uparrow_C\downarrow_D\rangle$. Coincidence between the endpoints of these phase-space paths is a prerequisite for this overlap to be large.

electronic phase factor of the aliased overlap is

$$\begin{aligned} e^{i\Omega(t_{DC}-t_{BA})}\langle\uparrow_A \mid \uparrow_B\uparrow_C\downarrow_D\rangle \sim \exp\Bigg\{ & \frac{i}{\hbar}\left(\epsilon_{\bar{g}e}+\frac{\Delta\epsilon}{2}\right)\left(t_{DC}-t_{BA}\right) \\ & + \frac{i}{\hbar}\epsilon_{\bar{g}e}\left(t_{DC}+\frac{\tau_v}{2}+t_{BA}\right) - \frac{i}{\hbar}\left(2\epsilon_{eg}+\Delta\epsilon+\delta\epsilon\right)t_{DC} \\ & + \frac{i}{\hbar}\epsilon_{\bar{g}e}\left(t_{JB}-\frac{\tau_v}{2}\right) - \frac{i}{\hbar}\left(\epsilon_{\bar{e}g}+\Delta\epsilon\right)t_{JB}\Bigg\} \\ = \exp\Bigg\{ & -\frac{i}{\hbar}\Delta\epsilon\left(\frac{t_{DC}+t_{BA}}{2}+t_{JB}\right) - \frac{i}{\hbar}\delta\epsilon\, t_{DC}\Bigg\} \end{aligned} \tag{2.82}$$

(see p. 38), where $\Delta\epsilon = \epsilon_{\bar{e}g} - \epsilon_{\bar{g}e} = \hbar\omega/2$ is the site-energy offset and $\delta\epsilon = 0, -\hbar\omega/2$ is the exciton shift. In the absence of the latter,

$$e^{i\Omega(t_{DC}-t_{BA})}\langle\uparrow_A \mid \uparrow_B\uparrow_C\downarrow_D\rangle \sim \exp\left\{-i\omega\left(\frac{t_{DC}+t_{BA}}{4}+\frac{t_{JB}}{2}\right)\right\}, \tag{2.83}$$

while in its presence,

$$e^{i\Omega(t_{DC}-t_{BA})}\langle\uparrow_A \mid \uparrow_B\uparrow_C\downarrow_D\rangle \sim \exp\left\{i\omega\left(\frac{t_{DC}-t_{BA}}{4}-\frac{t_{JB}}{2}\right)\right\}. \tag{2.84}$$

Equations (2.83) and (2.84) account for the constant phase of the overlap along lines of constant $t_{DC}+t_{BA}$ and $t_{DC}-t_{BA}$ seen in Figs. 21 and 23, respectively.

2.4.2 Signals

While the delay dependence of the individual overlaps is relatively easy to analyze in terms of wave-packet dynamics, the 2D-WPI signal (2.37) comprises a quantum-yield-weighted sum of the several contributing overlaps. Under the assumptions described on p. 17, the difference-phased whoopee signal from our model dimer becomes

$$S^{(d)} \propto Q_{one}P^{(d)}_{one} + Q_{two}P^{(d)}_{two} = 2\mathrm{Re}\{e^{-i\varphi_{BA}+i\varphi_{DC}}\xi_d\}\,, \tag{2.85}$$

where the relevant quadrilinear populations are given by Eqs. (2.56) and (2.57). Since one of the equal-and-opposite overlaps involving access to the doubly excited state contributes to $P^{(d)}_{one}$ and the other determines $P^{(d)}_{two}$, their degree of cancellation will depend on the relative quantum yield from populations in the singly- and doubly-excited manifolds. As described on p. 39, we shall examine calculated signals for $Q_{two}/Q_{one} = 0, 1$, and 2.

Figure 25 presents the 2D interferogram determined by the calculated overlaps in the case $Q_{two}/Q_{one} = 0$. In the top (bottom) row are the real part and absolute value of ξ_d without (with) an exciton shift. Although $\langle\uparrow_A\uparrow_D \mid \uparrow_B\uparrow_C\rangle$ fails to contribute in this case, the interferogram remains sensitive to the exciton shift through

$\langle\uparrow_A \mid \uparrow_B\uparrow_C\downarrow_D\rangle$; both complex-valued and absolute interferograms differ markedly in the two cases.

If $Q_{two}/Q_{one} = 1$, the case of equal fluorescence yields from the singly- and doubly-excited manifolds, then $\langle\uparrow_A \mid \uparrow_B\uparrow_C\downarrow_D\rangle$ and $\langle\uparrow_A\uparrow_D \mid \uparrow_B\uparrow_C\rangle$ cancel each other exactly; the interference signal becomes independent of any exciton shift. The 2D WPI signal, illustrated in Fig. 26, is now determined by the two remaining overlaps contributing to $P^{(d)}_{one}$.

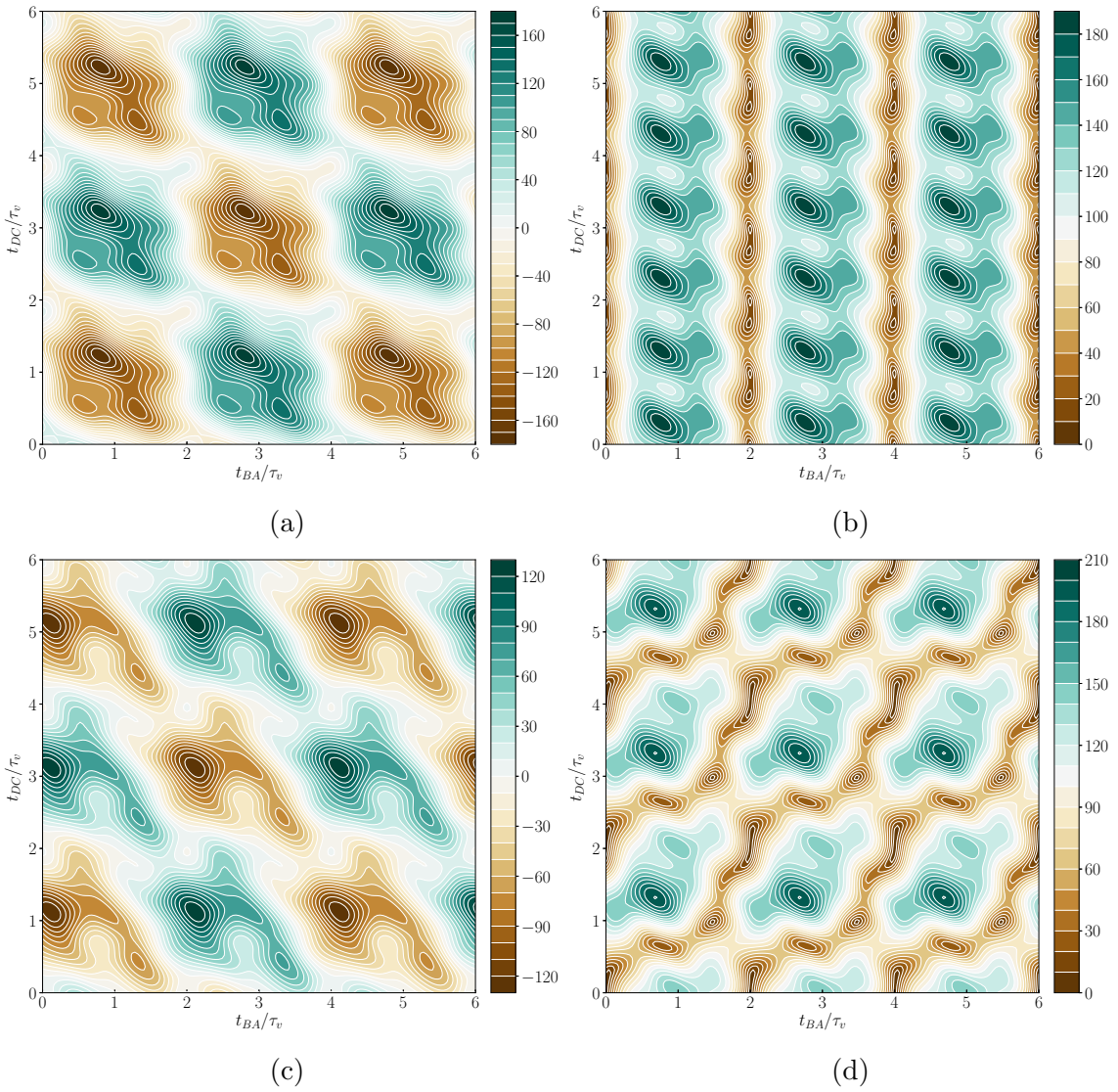

Figure 25. The top two panels exhibit $\mathrm{Re}\{\xi_d\} = \xi_d'$ and $|\xi_d|$ for the EET dimer with $Q_{two}/Q_{one} = 0$ in the absence of an exciton shift. Their forms in the presence of a small, negative shift are shown in the bottom row.

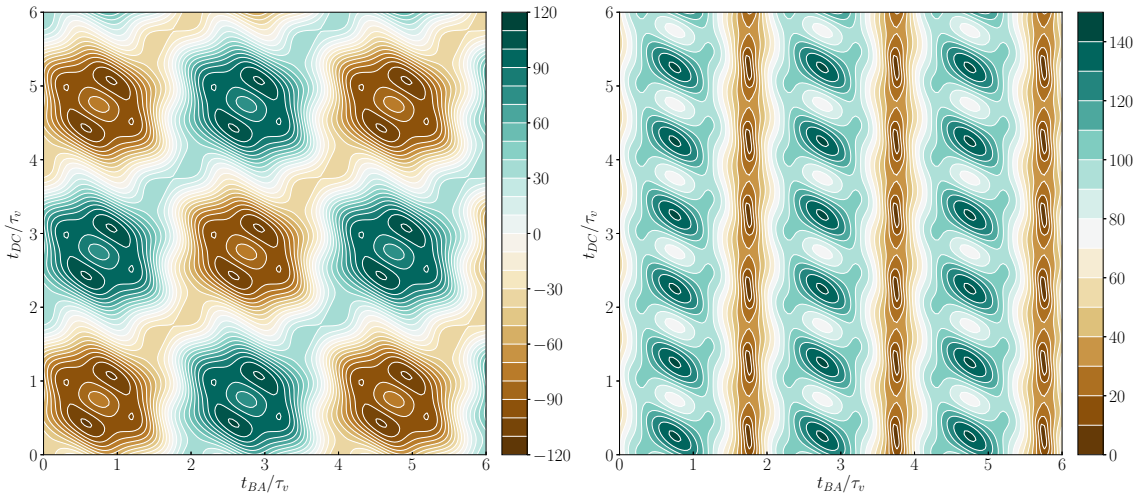

Figure 26. The real part and absolute value of the WPI signal for $Q_{two}/Q_{one} = 1$, which is not affected by an exciton shift.

Sensitivity to the exciton shift returns when $Q_{two}/Q_{one} = 2$, meaning that the doubly-excited state is twice as productive of fluorescent photons as a singly-excited state. Here, the contribution from $\langle\uparrow_A\uparrow_D | \uparrow_B\uparrow_C\rangle$ outweighs that from $\langle\uparrow_A | \uparrow_B\uparrow_C\downarrow_D\rangle$. ξ_d for the EET dimer for this yield ratio is shown in Fig. 27.

The calculations presented in this section illustrate the physical information content and dynamical interpretation of two-dimensional wave-packet interferometry signals from an energy-transfer dimer for a specific set of molecular features and experimental parameters. Many elaborations and generalizations remain to be investigated. While the present illustrative calculations yield interferograms of undiminished signal intensity with increasing t_{BA} and t_{DC}, more realistic simulations including (perhaps weak) electronic-nuclear coupling for a large number of intra- and intermolecular modes would of course exhibit "optical dephasing." As a result, increasing intrapulse-pair delays would be accompanied by decreasing signal size [6].

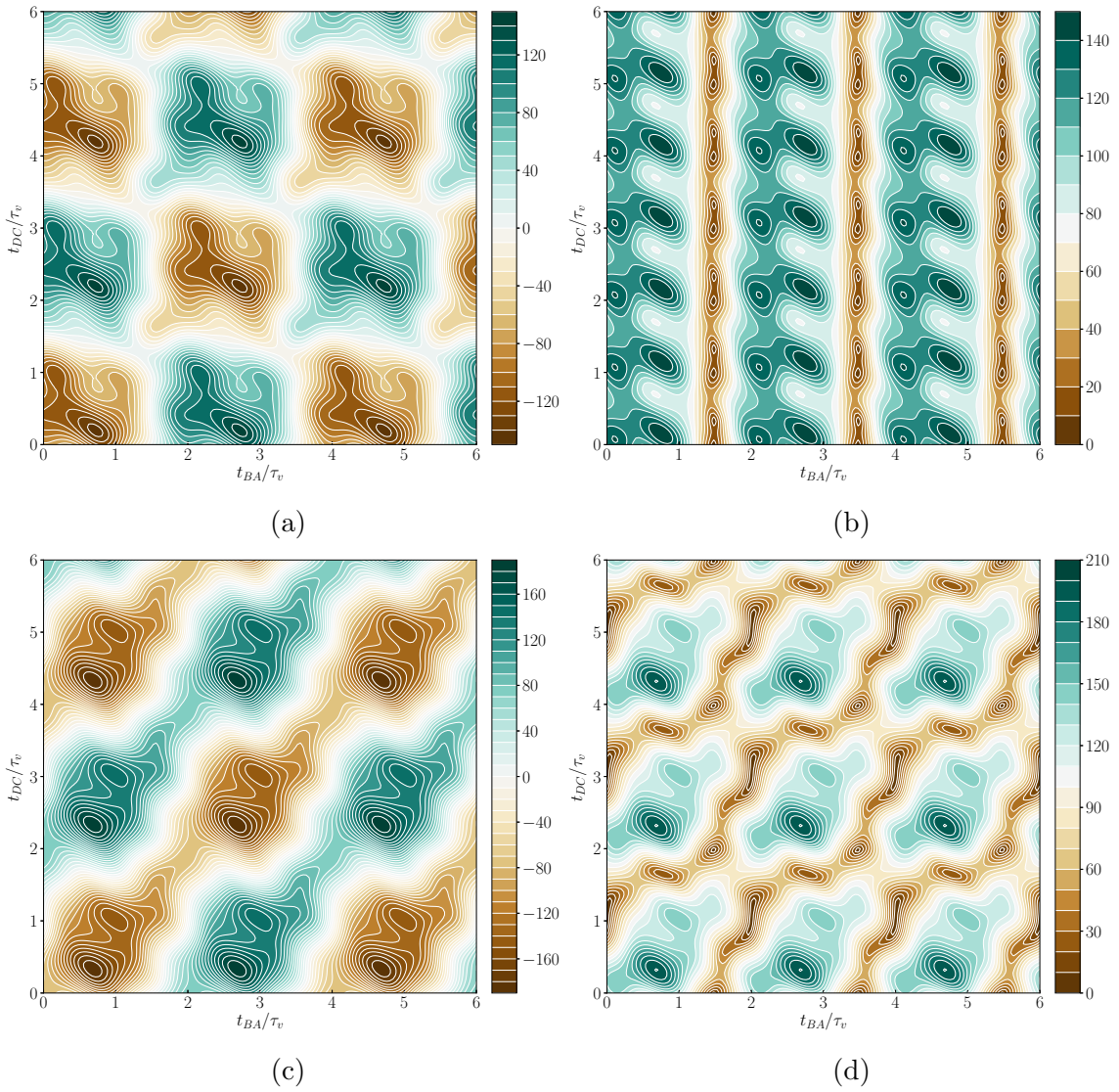

Figure 27. The top panels show ξ_d with $Q_{two}/Q_{one} = 2$ and no exciton shift. The bottom two include a small down-shift for singly-to-doubly excited transitions.

2.5 Conclusion

This chapter spells out a straightforward, general framework for calculating and interpreting multidimensional electronic spectroscopy signals in terms of the wave-packet-shaping, amplitude-transferring effects of femtosecond laser pulses on time-dependent molecular states. It sets up the basic expressions for two-dimensional wave-packet interferometry experiments on an energy-transfer system as a quantum yield-weighted sum of contributing overlaps between multi-pulse wave packets, and identifies the ranges of interpulse delay within which each overlap is not excluded by its order of pulse action from contributing to the WPI signal.

Example calculations are presented for a spatially oriented, weakly coupled EET dimer for whose individual overlaps physical interpretations are readily found using semiclassical analyses of the necessary conditions for phase-space coincidence between the bra and ket, the dynamical consequences of a site-energy difference between to two chromophores, and the sensitivity of contributions accessing or originating from doubly electronically excited states of the dimer to the possible presence of an exciton shift.

The version of the model used for illustration is among the simplest conceivable for basic examination of the information content of 2D ES in the context of electronic excitation transfer, and many possibilities exist for increasing its complexity. One possible change would be to incorporate electronic decoherence by adding site-state-dependent electronic-nuclear coupling to a multiplicity of intra- and intermolecular modes of various frequencies [6]. Another natural step is to increase the number of participating monomers. For example, a tetramer of chromophores arranged in a square geometry could give rise to a conical intersection between single-exciton states, which would in principle generate

geometric-phase effects in the EET dynamics. In addition, the occurrence of excitation transfer to more than one neighboring chromophore could result in spatial interference akin to that seen in double-slit experiments. For instance, excitation could transfer from an individual chromophore to the non-adjacent one by taking more than one pathway. Of interest would be the extent to which electronic-nuclear coupling suppresses the resulting interference in excitation transfer by "observing" through which of the neighboring chromophores the excitation was passed. Possibilities may also exist for altering the interference by prior preparation of nuclear motion in the electronic ground state via impulsive stimulated Raman excitation.

2.6 Bridge

This chapter has introduced a general framework for the calculation of two-dimensional wave-packet interferometry signals. This framework puts the dynamics of the system at the forefront of the theory, highlighting the motion of the wave packets prepared by the laser pulses. Also introduced in this chapter is a spatially-oriented, energy transfer dimer. This model is used to study the appearance of electronic energy transfer in WPI signals. The following chapter expands on this work, making use of both the same theoretical framework and the same model dimer to devise an experiment that allows for the direct observation of electronic coherence.

CHAPTER III

MONITORING THE EVOLUTION OF INTERSITE AND INTEREXCITON COHERENCE IN ELECTRONIC EXCITATION TRANSFER VIA WAVE-PACKET INTERFEROMETRY

This work is currently in press in the Journal of Chemical Physics. Both Jeffrey Cina and Alexis Kiessling derived the expressions, computed the signals appearing in the chapter, and wrote the paper. Jeffrey Cina was the principal investigator during this work.

3.1 Introduction

The linear optical spectroscopy of oriented molecular samples is widely practiced and highly informative [20]. Although ultrafast nonlinear optical spectroscopy with variably polarized pulse sequences has been very effectively applied to many complex isotropic samples [21, 22, 23, 24], experiments on ensembles of oriented chromophores, such as macromolecular single crystals, are rare [25]. This remains the case despite the fact that in measurements of that kind, individual pulses can be made to address specific chromophores based on their transition-dipole moment direction [26, 27]. By contrast, multi-pulse femtosecond polarization spectroscopy experiments in isotropic media "burn" at least one pulse in rendering the sample anisotropic, yet fail to fully fix the spatial orientations in the optically activated ensemble [28, 29].

Here we explore a general situation in which ultrafast polarization spectroscopy experiments on oriented samples could directly access a key feature of widespread interest in chemical dynamics, namely the time development of electronic coherence in electronic excitation transfer (EET). The manifestations of electronic, vibrational, and vibronic coherence in two-dimensional electronic

and other ultrafast spectroscopy signals from multi-chromophore complexes and their significance for excitation transport have been the subject of extensive recent consideration [30, 31, 32, 33, 34, 35, 36, 37, 38, 39, 40, 41, 42, 43, 44, 45].[1] Using a wave-packet interferometry (WPI) approach, we investigate 2D spectroscopy signals for a spatially oriented EET dimer with nonparallel site transition-dipole moments. We find that it is possible to isolate from 2D-WPI signals of certain polarizations the time-evolving intersite or interexciton electronic coherence.

The present study builds on previous work by Cina and Kiessling [27], which put forward a general framework for calculating and interpreting 2D-WPI signals with an emphasis on the entanglement of electronic and nuclear dynamics.[2] We consider measurements carried out on an oriented EET dimer of the same kind considered previously and show where salient information on electronic coherence "lives" within a 2D data set. The basic approach is found to be viable under both weak and strong EET coupling. It enables the tracking of electronic coherence

[1]The issue of long-lived signal oscillations from the Fenna-Matthews-Olson complex, in particular, has recently been incisively addressed by Scholes and co-workers.[33] They reported broadband pump-probe spectroscopy data from wild-type FMO complexes as well as complexes perturbed by site-directed mutagenesis. In all cases, oscillatory contributions to the signal traces at selected probe wavelengths exhibited contributions from common frequencies of about 160 and 199 cm^{-1}. These signal oscillations were shown to be predominantly vibrational in nature. Specifically, they make a similar appearance throughout the broadband probe spectrum in signals generated with a spectrally narrowed pump pulse providing access only to the red-most edge of the electronic absorption spectrum; this arrangement should preclude the preparation of a time-zero superposition between different excitonic levels.

[2]Equation (39) in Cina and Kiessling's book chapter [27] is incorrect. The sixth term in braces on the right-hand side of that equation should be $\langle\uparrow_D\downarrow_C\uparrow_A \quad |\xi\rangle\langle\xi| \quad \uparrow_B\rangle$, rather than $\langle\uparrow_C\downarrow_D\uparrow_A \quad |\xi\rangle\langle\xi| \quad \uparrow_B\rangle$. This error does not affect any of the calculations presented in the chapter, because the term vanishes when pulses C and D follow A and B by a delay longer than the pulse duration, as they are assumed to do in the WPI signals presented there. In addition, the $(\omega\langle q_b\rangle, \langle p_b\rangle)$ trajectory shown in the lower right panel of Fig. 22 in that chapter is incomplete. It should continue by circling clockwise about the phase-space origin for a time t_{DJ}, with the correct final phase-point being given by $\omega d e^{-i\omega t_{DJ}}(1 - e^{-i\omega t_{JA}})$. This correction does not alter the stated b-mode coincidence requirement. Finally, Eq. (10) of the chapter would be better replaced by $\sin\theta(Q) = J(Q)/M(Q)$ and $\cos\theta(Q) = K(Q)/M(Q)$.

using the preferred description in each case—intersite for weak coupling and interexcitonic for strong.

The paper continues by introducing the Hamiltonian for the oriented EET dimer and its interaction with a WPI sequence of four femtosecond laser pulses. Physical motivation is provided for the choice of pulse polarizations and timings in the weak- and strong-coupling cases, explaining their capacity to reveal the generation and evolution of intersite and interexcitonic coherence, respectively. Specific Hamiltonian parameters are chosen for illustrative signal calculations on dimers with various numbers of vibrational degrees of freedom. The resulting signals are then presented, and the time-course of the observed electronic coherence is discussed in each case. Various practical approaches to WPI coherence-detection experiments are then considered, and comparisons are made to related theoretical and experimental work. The last section concludes with a summary of our findings and worthwhile questions for future investigation.

3.2 Energy-Transfer Dimer

We can illustrate our strategy for electronic coherence tracking by treating a model molecular dimer whose Hamiltonian is given by

$$H = T + H_{\mathrm{el}}(Q)\,, \tag{3.1}$$

where T is the nuclear kinetic energy and $H_{\mathrm{el}}(Q)$ is the electronic Hamiltonian, parametrized by a collection Q of intramonomer, intermonomer, and bath-mode nuclear coordinate operators. In a basis of site-excited states in which neither, one or the other, or both of the chromophores are excited, the electronic Hamiltonian

may be written as

$$H_{\rm el}(Q) = |gg\rangle\, V_{gg}(Q)\, \langle gg| + |eg\rangle\, V_{eg}(Q)\, \langle eg| + |ge\rangle\, V_{ge}(Q)\, \langle ge| \\ + J\left(|eg\rangle\langle ge| + |ge\rangle\langle eg|\right) + |ee\rangle\, V_{ee}(Q)\, \langle ee| \,. \quad (3.2)$$

Here, the diabatic potential energy surface for the electronic ground state (gg) is V_{gg}, those for the singly excited states eg and ge are V_{eg} and V_{ge}, respectively, and that for the doubly excited ee state is V_{ee}. We regard the excitation-transfer coupling J as being independent of nuclear coordinates, but this need not be true in general. In a WPI experiment, this dimer is subject to four ultrashort laser pulses comprising two phase-locked pulse-pairs, with which it interacts via the perturbation

$$V(t) = \sum_{I=A,B,C,D} V_I(t)\,, \quad (3.3)$$

where

$$V_I(t) = -\hat{\mathbf{m}} \cdot \mathbf{E}_I(t)\,. \quad (3.4)$$

For the purpose of intersite coherence observation, it is essential that it be possible to separately address the two monomers by the choice of laser polarization. They must therefore have nonparallel molecular transition dipole moments whose orientations are fixed. Here we treat the simplest case, in which the two transition moments are mutually perpendicular, and accordingly take the complete dipole moment operator to be

$$\hat{\mathbf{m}} = \mathbf{m}_a\left(|eg\rangle\langle gg| + |ee\rangle\langle ge|\right) + \mathbf{m}_b\left(|ge\rangle\langle gg| + |ee\rangle\langle eg|\right) + H.c.\,, \quad (3.5)$$

where $\mathbf{m}_a = m\hat{\mathbf{x}}$ and $\mathbf{m}_b = m\hat{\mathbf{y}}$. The electric fields associated with the pulses take the form

$$\mathbf{E}_I(t) = \mathbf{e}_I E_I f(t - t_I)\cos\left[\Omega(t - t_I) + \varphi_I\right]\,, \quad (3.6)$$

where $\mathbf{e}_I$ is the polarization, E_I is the field strength, $f(t)$ is the common pulse envelope, Ω is the common carrier frequency, t_I is the arrival time of the pulse at the target dimer, and φ_I is the optical phase.

The site basis is a convenient choice for a dimer with weak energy-transfer coupling; that is, one whose EET coupling J is small in size compared to the difference between the site energies $V_{eg}(Q)$ and $V_{ge}(Q)$ for most relevant values of the nuclear coordinates. When J is *large* by this criterion, the exciton basis, defined as the eigenstates of $H_{\rm el}(Q)$ for the equilibrium configuration of nuclei $Q = 0$, provides a better zeroth-order description. Making use of the functions

$$K(Q) = \frac{1}{2}\left(V_{eg}(Q) - V_{ge}(Q)\right) , \tag{3.7}$$

$$L(Q) = \frac{1}{2}\left(V_{eg}(Q) + V_{ge}(Q)\right) , \tag{3.8}$$

and

$$M(Q) = \sqrt{J^2 + K^2(Q)}\,, \tag{3.9}$$

the Hamiltonian of Eq. (3.2) becomes

$$\begin{aligned} H_{\rm el}(Q) = {} & |0\rangle\langle 0|\, V_{gg}(Q) + |\bar{1}\rangle\langle\bar{1}|\left\{L(Q) + M + \frac{K}{M}\left[K(Q) - K\right]\right\} \\ & + |1\rangle\langle 1|\left\{L(Q) - M - \frac{K}{M}\left[K(Q) - K\right]\right\} - \left(|\bar{1}\rangle\langle 1| + |1\rangle\langle\bar{1}|\right)\frac{J}{M}\left[K(Q) - K\right] \\ & + |2\rangle\langle 2|\, V_{ee}(Q)\,, \end{aligned} \tag{3.10}$$

where $K = K(0)$ and $M = M(0)$. The exciton states appearing in Eq. (3.10) are

$$|0\rangle = |gg\rangle , \tag{3.11}$$

$$|\bar{1}\rangle = \frac{1}{\sqrt{2}}\left[|eg\rangle\sqrt{1 + \frac{K}{M}} + |ge\rangle\,\mathrm{sign}(J)\sqrt{1 - \frac{K}{M}}\right] , \tag{3.12}$$

$$|1\rangle = \frac{1}{\sqrt{2}}\left[|ge\rangle\sqrt{1 + \frac{K}{M}} - |eg\rangle\,\mathrm{sign}(J)\sqrt{1 - \frac{K}{M}}\right] , \tag{3.13}$$

and

$$|2\rangle = |ee\rangle \ . \tag{3.14}$$

The dipole operator in the exciton basis is

$$\begin{aligned}
\hat{\mathbf{m}} = {} & |\bar{1}\rangle\langle 0| \, \frac{1}{\sqrt{2}} \left[\mathbf{m}_a \sqrt{1 + \frac{K}{M}} + \mathbf{m}_b \, \mathrm{sign}(J) \sqrt{1 - \frac{K}{M}} \right] \\
& + |1\rangle\langle 0| \, \frac{1}{\sqrt{2}} \left[-\mathbf{m}_a \, \mathrm{sign}(J) \sqrt{1 - \frac{K}{M}} + \mathbf{m}_b \sqrt{1 + \frac{K}{M}} \right] \\
& + |2\rangle\langle \bar{1}| \, \frac{1}{\sqrt{2}} \left[\mathbf{m}_a \, \mathrm{sign}(J) \sqrt{1 - \frac{K}{M}} + \mathbf{m}_b \sqrt{1 + \frac{K}{M}} \right] \\
& + |2\rangle\langle 1| \, \frac{1}{\sqrt{2}} \left[\mathbf{m}_a \sqrt{1 + \frac{K}{M}} - \mathbf{m}_b \, \mathrm{sign}(J) \sqrt{1 - \frac{K}{M}} \right] + \mathrm{H.c.} \, .
\end{aligned} \tag{3.15}$$

In order that it be possible to selectively address the $\bar{1} \leftarrow 0$ and $1 \leftarrow 0$ electronic transitions of the spatially oriented dimer by a choice of laser polarization, it is necessary that $\langle \bar{1}| \, \hat{\mathbf{m}} \, |0\rangle$ and $\langle 1| \, \hat{\mathbf{m}} \, |0\rangle$ be nonparallel. In the case of perpendicular site-transition moments $\mathbf{m}_a = m\hat{\mathbf{x}}$ and $\mathbf{m}_b = m\hat{\mathbf{y}}$, we see that absorptive transitions to the single-exciton states are also perpendicularly polarized. We shall deal in a later section with a complication that arises in seeking to track interexciton coherence, namely that the transition moments $\langle 2| \, \hat{\mathbf{m}} \, |\bar{1}\rangle$ and $\langle 2| \, \hat{\mathbf{m}} \, |1\rangle$ for excited-state absorption, though again mutually perpendicular in the simple case at hand, do not generally lie along the same directions as those for absorption from the electronic ground state.

3.3 Electronic Coherence

In seeking to follow the time-evolution of electronic coherence in an excitation-transfer complex, it is important to emphasize that we wish to make measurements of the off-diagonal elements of the reduced electronic density matrix in the singly-excited subspace. It is essential to be specific concerning the basis

with respect to which the density matrix is to be represented; coherences in one basis contribute to populations (diagonal matrix elements) in another basis, and vice versa.

Consider first the coherence between singly-excited site states. The portion of the dimer's state that is linear in E_A and independent of the other fields can be written as

$$|\uparrow_A(t)\rangle = |eg\rangle\ |\phi_{eg}^{(A)}(t)\rangle + |ge\rangle\ |\phi_{ge}^{(A)}(t)\rangle\ . \tag{3.16}$$

This ket gives the amplitude in the singly excited manifold that would be generated by linear absorption were the A pulse unaccompanied by the B, C, and D pulses; the nuclear wave packets $|\phi_{eg}^{(A)}(t)\rangle$ and $|\phi_{ge}^{(A)}(t)\rangle$ could be calculated by time-dependent perturbation theory of first order in E_A. Under weak EET coupling (small J) and sufficiently short $t - t_A$, the nuclear wave packet $|\phi_{eg}^{(A)}(t)\rangle$ describing the amplitude in, say, an initially excited eg-state will be of zeroth order in J, while the wave packet $|\phi_{ge}^{(A)}(t)\rangle$ in the ge-state will be first order in J. The reduced electronic density operator corresponding to the state-ket (3.16) is

$$\begin{aligned}\rho_{\rm el}^{(A)}(t) &= \mathrm{Tr}_{\rm nuc}\left[\,|\uparrow_A(t)\rangle\langle\uparrow_A(t)|\right] \\ &= |eg\rangle\ \langle\phi_{eg}^{(A)}(t)|\phi_{eg}^{(A)}(t)\rangle\ \langle eg| + |eg\rangle\ \langle\phi_{ge}^{(A)}(t)|\phi_{eg}^{(A)}(t)\rangle\ \langle ge| \\ &\quad + |ge\rangle\ \langle\phi_{eg}^{(A)}(t)|\phi_{ge}^{(A)}(t)\rangle\ \langle eg| + |ge\rangle\ \langle\phi_{ge}^{(A)}(t)|\phi_{ge}^{(A)}(t)\rangle\ \langle ge|\ .\end{aligned} \tag{3.17}$$

The intersite electronic coherence at a certain time is given by either of the (complex conjugate) off-diagonal elements of $\rho_{\rm el}^{(A)}$. Thus,

$$\langle ge|\rho_{\rm el}^{(A)}(t)|eg\rangle = \langle\uparrow_A(t)|\,eg\rangle\langle ge\,|\uparrow_A(t)\rangle = \langle\phi_{eg}^{(A)}(t)|\phi_{ge}^{(A)}(t)\rangle \tag{3.18}$$

quantifies the overlap, or lack thereof, between the nuclear wave packet prepared in the "donor" state by short-pulse excitation and that generated in the "acceptor" state by excitation transfer. For given donor and acceptor populations, larger

or smaller magnitudes of this coherence herald lesser or greater entanglement, respectively, between the electronic site states and the nuclear "environment."

In the strong EET-coupling case, the coherence between the single-exciton states $|\bar{1}\rangle$ and $|1\rangle$ is more convenient to prepare and monitor. The physical significance of this quantity,

$$\langle 1|\rho_{\mathrm{el}}^{(A)}(t)|\bar{1}\rangle = \langle \uparrow_A (t)|\bar{1}\rangle\langle 1|\uparrow_A (t)\rangle = \langle \phi_{\bar{1}}^{(A)}(t)|\phi_1^{(A)}(t)\rangle\,, \tag{3.19}$$

with respect to the exciton basis states and their nuclear environment is entirely analogous to that of the intersite coherence with respect to the site states. At short enough times $t - t_A$, this coherence will be linear in the interexciton coupling (see Eq. (3.10)). Once constructed in a particular basis, the reduced electronic density matrix can readily be converted to another basis by a unitary transformation.

3.4 WPI Signal

3.4.1 Setup

Let us find out where information on the electronic coherence (3.18) or (3.19) resides in the data from a 2D-WPI experiment on the spatially oriented dimer, investigate the physical basis for its contribution to signal formation, and determine whether and to what extent these evolving, complex-valued coherences can be reliably isolated. The measured quantity in such an experiment is the portion of the time- and frequency-integrated fluorescence proportional to a quantum-yield-weighted sum of quadrilinear electronic state populations (i.e., those parts proportional to $E_A E_B E_C E_D$). The intrapulse-pair optical phase shifts $\varphi_{BA} = \varphi_B - \varphi_A$ and $\varphi_{DC} = \varphi_D - \varphi_C$ are assumed to be under experimental control (see Eq. (3.6)), while the *inter*pulse-pair shifts, such as $\varphi_C - \varphi_B$, vary "randomly" from shot to shot over the many realizations of the pulse sequence required to accumulate a single data-point.

A "two-dimensional" dataset contains the quadrilinear fluorescence signal as a function of the two intrapulse-pair delays t_{BA} and t_{DC}, for a range in waiting times t_{CB}[27]. The sum- and difference-phased components, proportional to $e^{-i\varphi_{BA}-i\varphi_{DC}}$ and $e^{-i\varphi_{BA}+i\varphi_{DC}}$, respectively, can be collected and analyzed separately [46, 47, 18, 48]. Here it is sufficient to examine the dimer's difference-phased 2D-WPI signal, using the notation of Cina and Kiessling [27]. In the situation where t_A and t_B precede t_C and t_D by more than the pulse duration, it takes the stripped-down form

$$\begin{aligned} S_{\rm d} = 2Q_{\rm one}{\rm Re}\big\{ &\langle\uparrow_A\downarrow_B\uparrow_D \mid \uparrow_C\rangle + \langle\uparrow_A\downarrow_C\uparrow_D \mid \uparrow_B\rangle + \langle\uparrow_D \mid \uparrow_B\downarrow_A\uparrow_C\rangle \\ &+ \langle\uparrow_A \mid \uparrow_B\downarrow_D\uparrow_C\rangle + \langle\uparrow_A\uparrow_D\downarrow_C \mid \uparrow_B\rangle + \langle\uparrow_A \mid \uparrow_B\uparrow_C\downarrow_D\rangle\big\} \\ &+ 2Q_{\rm two}{\rm Re}\big\{\langle\uparrow_A\uparrow_D \mid \uparrow_B\uparrow_C\rangle\big\}\,, \end{aligned} \tag{3.20}$$

where $Q_{\rm one}$ ($Q_{\rm two}$) is the quantum yield of the singly-excited (doubly-excited) manifold.

We will show that a sequence of "zero-dimensional" data-points extracted from the 2D signal (3.20)—a pump-probe sequence in which the delay t_{CB} is scanned while the two pulses in each phase-locked pair are made contemporaneous—houses the sought-after coherences. Physical motivation for this notion can be provided by considering the contributing overlap $\langle\uparrow_A\downarrow_C\uparrow_D \mid \uparrow_B\rangle$ when $t_A = t_B = 0$ and $t_C = t_D \equiv t$ under weak EET coupling. For this small-J case, we choose $\mathbf{e}_A = \mathbf{e}_B = \mathbf{e}_C = \hat{\mathbf{x}}$ and $\mathbf{e}_D = \hat{\mathbf{y}}$, so that A, B, and C address the donor chromophore, while D addresses the acceptor.

The B-pulse, now identical to the A-pulse except for phase, copies the ground-state nuclear wave packet from the *gg*-state to the donor-excited *eg*-state. Figure 28 illustrates this wave function prior to electronic excitation for a simple situation in which each monomer has just one Franck-Condon-active vibrational

mode (Sec. 3.5 specifies the relevant model Hamiltonian). This nuclear distribution is shown in the top panel of Fig. 29 after it has accompanied the pulse-induced change in electronic state. Following a certain delay (here, three quarters of a vibrational period), most of the evolving amplitude, shown in the middle frame, remains on the donor-excited surface. The small amplitude resulting from energy transfer to the acceptor-excited *ge*-state is illustrated in the bottom panel. It is the overlap between the nuclear wave packets appearing in the bottom and middle panels of Fig. 29 that we want to measure; but because both of these are linear in E_B and because, in any case, they reside on different electronic surfaces, their overlap does not contribute directly to the whoopee signal.

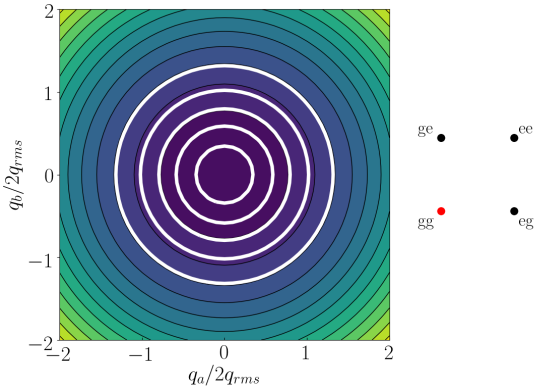

Figure 28. The stationary nuclear wave function $\phi_0(q_a, q_b)$ in the electronic ground state of a model dimer is shown in white contours and the *gg*-potential surface—both monomers unexcited—is rendered in color. Distance is reckoned in units of $2q_{\rm rms} = 2\sqrt{\hbar/2\omega}$, where ω is the vibrational frequency.

Instead, the bra in $\langle\uparrow_A\downarrow_C\uparrow_D \mid \uparrow_B\rangle$ acts as a surrogate for the propagated *eg*-state wave packet in the middle of Fig. 29. As shown in Fig. 30, it is prepared by the *A*-pulse and reproduced in the *ge*-state by a Raman-like process driven by the *C* and *D* pulses. The resulting quadrilinear overlap manifests the quantum mechanical interference between this reference wave packet and the target packet which results from excitation transfer, as pictured in Fig. 31.

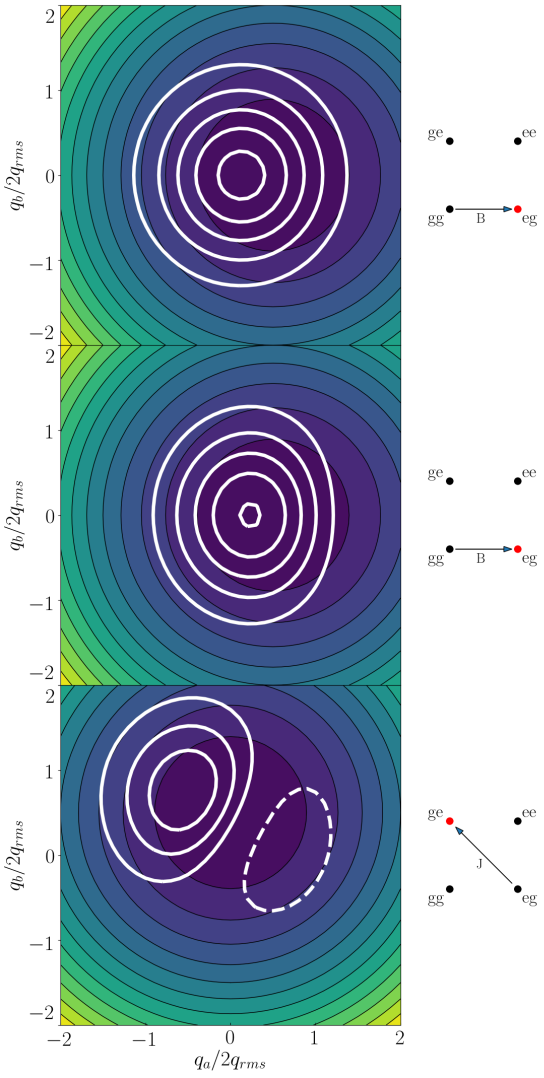

Figure 29. Nuclear wave packets associated with $|\uparrow_B\rangle$. An x-polarized B-pulse of duration $\sigma = 0.09\tau_v$ prepares the time-zero eg-state packet shown in the top panel, where $\tau_v = 2\pi/\omega$ is the vibrational period. Middle panel portrays the amplitude remaining on the eg-surface at $t = 0.75\tau_v$. Bottom panel shows the nuclear wave packet generated by energy transfer on the acceptor-excited ge-surface as it appears at this same time.

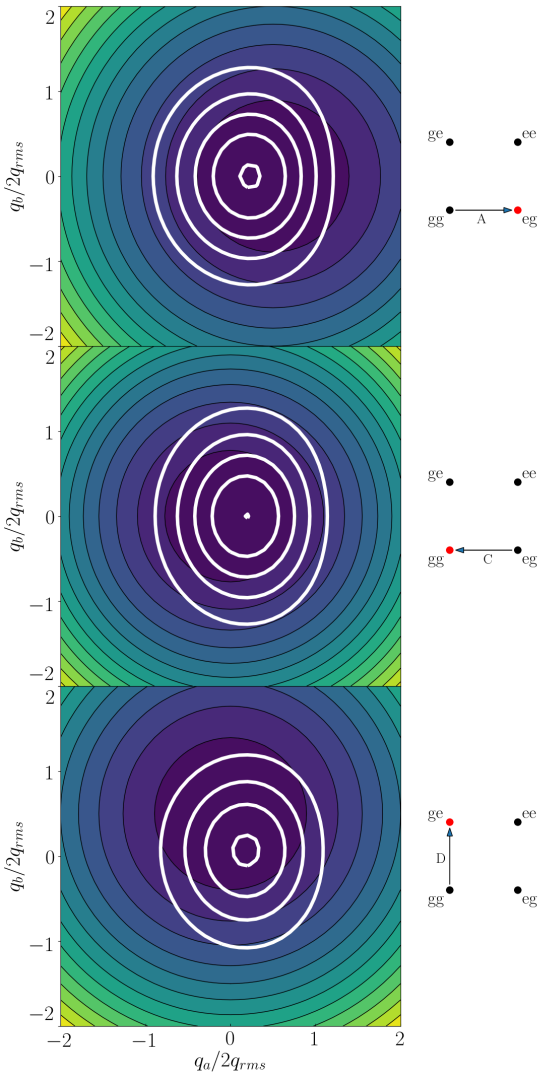

Figure 30. Nuclear wave packets associated with $|\ \uparrow_A\downarrow_C\uparrow_D\rangle$. The top panel depicts the packet prepared by the short, x-polarized A pulse and $0.75\tau_v$ of eg-state evolution. It is identical within a phase-factor to that shown in the middle panel of Fig. 29. The middle panel shows this wave packet after it has been dumped to the gg-state by the x-polarized C-pulse. The bottom frame displays the copy prepared in ge upon re-excitation by the simultaneous, y-polarized D-pulse. Although the final ge-state wave packet would actually be produced by the nested action of the C and D pulses, the bottom frame shows one that would be generated by separately occurring de- and reexcitation processes, with a neglect of temporal pulse overlap.

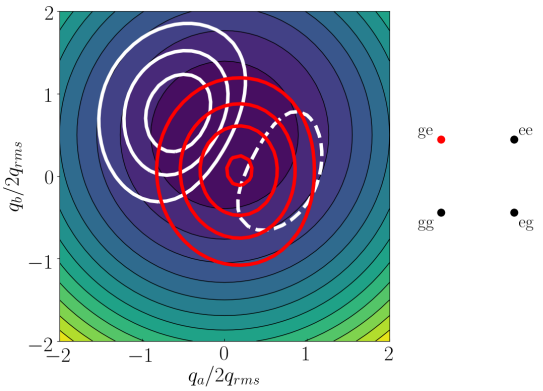

Figure 31. The *eg*-state target (white) and reference (red) wave packets whose quantum mechanical overlap determines the value of $\langle\uparrow_A\downarrow_C\uparrow_D \;\mid\; \uparrow_B\rangle$. This overlap contributes to the 2D-WPI signal and quantifies the intersite electronic coherence at $t = 0.75\tau_v$.

Under strong EET coupling (J larger than the total Franck-Condon energy), a similar argument demonstrates that $\langle\uparrow_A\downarrow_C\uparrow_D \;\mid\; \uparrow_B\rangle$ reveals the interexciton coherence. In this case, we align the polarization of pulses A, B, and C with $\langle\bar{1}|\,\hat{\mathbf{m}}\,|0\rangle$ and that of pulse D with $\langle 1|\,\hat{\mathbf{m}}\,|0\rangle$, as explained below Eq. (3.15). Now the target wave packet resides in state-1, having been prepared by B-pulse excitation to state-$\bar{1}$ followed by first-order interexciton amplitude transfer. The three-pulse reference wave packet generated by A-pulse excitation to $|\bar{1}\rangle$ and Raman-transfer to $|1\rangle$ through the combined action of the perpendicularly polarized C and D pulses mimics the B-pulse amplitude left behind in the $\bar{1}$ state.

Two of the contributing overlaps become negligible along the $t_{BA} = t_{DC} = 0$ slice of the 2D signal (3.20). We shall assume that in the small-J case, the pulse durations are very short on the timescale $h/|J|$ of energy transfer. In the large-J case, they will be assumed short on the timescale $hM/|J\,[K(Q) - K]\,|$ of interexciton amplitude transfer. With the polarization combinations we are choosing, the overlaps $\langle\uparrow_A\downarrow_B\uparrow_D \;\mid\; \uparrow_C\rangle$ and $\langle\uparrow_D \;\mid\; \uparrow_B\downarrow_A\uparrow_C\rangle$ both vanish, because they require energy transfer (or an interexciton transition) *during* the simultaneous

C and D pulses. In addition, we can make use of two identities,

$$\langle\uparrow_A \mid \uparrow_B\downarrow_D\uparrow_C\rangle + \langle\uparrow_A\downarrow_C\uparrow_D \mid \uparrow_B\rangle = -\langle\uparrow_A\downarrow_C \mid \uparrow_B\downarrow_D\rangle\,, \tag{3.21}$$

and

$$\langle\uparrow_A\uparrow_D\downarrow_C \mid \uparrow_B\rangle + \langle\uparrow_A \mid \uparrow_B\uparrow_C\downarrow_D\rangle = -\langle\uparrow_A\uparrow_D \mid \uparrow_B\uparrow_C\rangle\,. \tag{3.22}$$

Eqs. (3.21) and (3.22) record the fact that population of one manifold in a given process leads to equal depopulation of another (and can be proved directly using explicit formulas for the overlaps of the kind to be developed shortly). We arrive at a simplified working expression for the 2D-WPI signal along the pump-probe slice on which we wish to focus:

$$S_{\rm d}(t) = 2{\rm Re}\big\{\big(Q_{\rm two} - Q_{\rm one}\big)\langle\uparrow_A\uparrow_D \mid \uparrow_B\uparrow_C\rangle - Q_{\rm one}\langle\uparrow_A\downarrow_C \mid \uparrow_B\downarrow_D\rangle\big\}\,. \tag{3.23}$$

3.4.2 Explicit Overlaps

3.4.2.1 Weak EET Coupling

The next task is to obtain explicit expressions for the overlaps appearing in Eq. (3.23). We consider first the weak EET-coupling case in which polarizations $\mathbf{e}_A = \mathbf{e}_B = \mathbf{e}_C = \hat{\mathbf{x}}$ and $\mathbf{e}_D = \hat{\mathbf{y}}$ are to be adopted. In this situation, both $\mid\uparrow_A\uparrow_D\rangle$ and $\mid\uparrow_A\downarrow_C\rangle$ can be regarded as zeroth-order in J, while $\mid\uparrow_B\uparrow_C\rangle$ and $\mid\uparrow_B\downarrow_D\rangle$ are first order. Accordingly, we may use

$$\mid\uparrow_A\uparrow_D\rangle^{(0)} = -|ee\rangle e^{-i\varphi_A - i\varphi_D} m^2 F_A F_D p^{(ee\,eg)}[t]^{(0)}_{eg\,eg} p^{(eg\,gg)}|\phi_0\rangle\,, \tag{3.24}$$

and

$$\mid\uparrow_A\downarrow_C\rangle^{(0)} = -|gg\rangle e^{-i\varphi_A + i\varphi_C} m^2 F_A F_C p^{(gg\,eg)}[t]^{(0)}_{eg\,eg} p^{(eg\,gg)}|\phi_0\rangle\,, \tag{3.25}$$

as well as

$$\mid\uparrow_B\uparrow_C\rangle^{(1)} = -|ee\rangle e^{-i\varphi_B - i\varphi_C} m^2 F_B F_C p^{(ee\,ge)}[t]^{(1)}_{ge\,eg} p^{(eg\,gg)}|\phi_0\rangle\,, \tag{3.26}$$

and

$$|\uparrow_B\downarrow_D\rangle^{(1)} = -|gg\rangle e^{-i\varphi_B+i\varphi_D} m^2 F_B F_D p^{(gg\,ge)}[t]^{(1)}_{ge\,eg} p^{(eg\,gg)}|\phi_0\rangle\,; \tag{3.27}$$

here, $|\phi_0\rangle$ is the initial vibrational state in $|gg\rangle$ and $F_I = E_I\sigma/2\hbar$ (where σ is the pulse-duration parameter). These formulas also employ reduced pulse propagators

$$p^{(\bar{\xi}\,\xi)} = \frac{1}{\sigma}\int_{-\infty}^{\infty} d\tau f(\tau) e^{\mp i\Omega\tau}[-\tau]^{(0)}_{\bar{\xi}\,\bar{\xi}}[\tau]^{(0)}_{\xi\,\xi}\,, \tag{3.28}$$

in which the upper (lower) sign is to be used for an absorptive (emissive) transition $\bar{\xi} \leftarrow \xi$ ($\xi \rightarrow \bar{\xi}$), along with the portions of the free-evolution operators $[t]_{\bar{\xi}\,\xi} = \langle\bar{\xi}|[t]|\xi\rangle \equiv \langle\bar{\xi}|\exp\{-itH/\hbar\}|\xi\rangle$ which are zeroth- or first-order with respect to the EET coupling.

Substituting Eqs. (3.24) through (3.27) in Eq. (3.23) yields

$$\begin{aligned} S_{\rm d}(t) = 2m^4 F_A F_B F_C F_D \mathrm{Re}\big\{ & e^{-i\varphi_{BA}+i\varphi_{DC}} \\ & \times \big[(Q_{\rm two}-Q_{\rm one})\langle\phi_0|p^{(gg\,eg)}[-t]^{(0)}_{eg\,eg}p^{(eg\,ee)}p^{(ee\,ge)}[t]^{(1)}_{ge\,eg}p^{(eg\,gg)}|\phi_0\rangle \\ & - Q_{\rm one}\langle\phi_0|p^{(gg\,eg)}[-t]^{(0)}_{eg\,eg}p^{(eg\,gg)}p^{(gg\,ge)}[t]^{(1)}_{ge\,eg}p^{(eg\,gg)}|\phi_0\rangle\big]\big\}\,; \end{aligned} \tag{3.29}$$

this is the formula by which the signal is actually calculated in weak EET-coupling cases. But $mF_A e^{-i\varphi_A}[t]^{(0)}_{eg\,eg}p^{(eg\,gg)}|\phi_0\rangle = -i\langle eg|\ \uparrow_A\ (t)\rangle$ and $mF_B e^{-i\varphi_B}[t]^{(1)}_{ge\,eg}p^{(eg\,gg)}|\phi_0\rangle$ $= -i\langle ge|\ \uparrow_B\ (t)\rangle = -i(F_B/F_A)e^{-i\varphi_{BA}}\langle ge|\ \uparrow_A\ (t)\rangle$, so Eq. (3.29) can be re-expressed as

$$\begin{aligned} S_{\rm d}(t) = 2m^2\frac{F_B}{F_A}F_C F_D \mathrm{Re}\big\{ & e^{-i\varphi_{BA}+i\varphi_{DC}} \\ & \times \langle\uparrow_A(t)|eg\rangle\big[(Q_{\rm two}-Q_{\rm one})p^{(eg\,ee)}p^{(ee\,ge)} - Q_{\rm one}p^{(eg\,gg)}p^{(gg\,ge)}\big]\langle ge|\uparrow_A(t)\rangle\big\}\,. \end{aligned} \tag{3.30}$$

The square-bracketed quantity in Eq. (3.30) differs from a scalar only to the extent that the pulse duration σ—though assumed to be abrupt compared to

energy transfer—may not turn out to be brief on the shorter timescale of nuclear dynamics. Within this small limitation, this expression reveals that the 2D-WPI signal allows the direct experimental isolation of the complex-valued intersite electronic coherence $\langle \uparrow_A (t)|eg\rangle\langle ge| \uparrow_A (t)\rangle$.

3.4.2.2 Strong EET Coupling

In the case of strong EET coupling, we can again work from the starting formula (3.23) to obtain an explicit expression for the pump-probe slice of the WPI signal. Now we take $\mathbf{e}_A = \mathbf{e}_B = \mathbf{e}_C = \frac{1}{\sqrt{2}}\left[\hat{\mathbf{x}}\sqrt{1+\frac{K}{M}} + \hat{\mathbf{y}}\,\mathrm{sign}(J)\sqrt{1-\frac{K}{M}}\right]$, parallel to $\langle\bar{1}|\hat{\mathbf{m}}|0\rangle$, and $\mathbf{e}_D = \frac{1}{\sqrt{2}}\left[-\hat{\mathbf{x}}\,\mathrm{sign}(J)\sqrt{1-\frac{K}{M}} + \hat{\mathbf{y}}\sqrt{1+\frac{K}{M}}\right]$, parallel to $\langle 1|\hat{\mathbf{m}}|0\rangle$. One of the contributing overlaps takes the simple form

$$\langle \uparrow_A\downarrow_C \mid \uparrow_B\downarrow_D\rangle = m^2 F_C F_D e^{i\varphi_{DC}} \langle \uparrow_A (t)|\bar{1}\rangle\, p^{(\bar{1}0)} p^{(01)} \langle 1| \uparrow_B (t)\rangle\,, \tag{3.31}$$

where $| \uparrow_A (t)\rangle = i[t]|\bar{1}\rangle m F_A e^{-i\varphi_A} p^{(\bar{1}0)}|\phi_0\rangle$ and $| \uparrow_B (t)\rangle = (F_B/F_A)e^{-i\varphi_{BA}}| \uparrow_A (t)\rangle$. In the signal calculation, $\langle \uparrow_A (t)|\bar{1}\rangle$ is to be evaluated at zeroth order in the interexciton coupling, and $\langle 1| \uparrow_B (t)\rangle$ at first order.

The other overlap is more complicated due to the fact that $\langle 2|\hat{\mathbf{m}}|\bar{1}\rangle$ and $\langle 2|\hat{\mathbf{m}}|1\rangle$ may not be aligned with the laser polarizations:

$$\begin{aligned}
&\langle \uparrow_A\uparrow_D \mid \uparrow_B\uparrow_C\rangle = m^2 F_C F_D e^{i\varphi_{DC}} \\
&\times \left\{ \tfrac{JK}{M^2} \langle \uparrow_A (t)|\bar{1}\rangle\, p^{(\bar{1}2)} p^{(2\bar{1})} \langle \bar{1}| \uparrow_B (t)\rangle + \tfrac{K^2}{M^2} \langle \uparrow_A (t)|\bar{1}\rangle\, p^{(\bar{1}2)} p^{(21)} \langle 1| \uparrow_B (t)\rangle \right. \\
&\left. - \tfrac{J^2}{M^2} \langle \uparrow_A (t)|1\rangle\, p^{(12)} p^{(2\bar{1})} \langle \bar{1}| \uparrow_B (t)\rangle - \tfrac{JK}{M^2} \langle \uparrow_A (t)|1\rangle\, p^{(12)} p^{(21)} \langle 1| \uparrow_B (t)\rangle \right\},
\end{aligned} \tag{3.32}$$

in which the nuclear wave packets in the $\bar{1}$- and 1-states are to be evaluated at zeroth and first order, respectively, with respect to the interexciton coupling. Since K is assumed to be smaller in size than J, we see that the overlap (3.32) gives less weight to the desired $|\bar{1}\rangle\langle 1|$ coherence than to the populations $|\bar{1}\rangle\langle\bar{1}|$ and $|1\rangle\langle 1|$, and still less than to the conjugate coherence $|1\rangle\langle\bar{1}|$.

Substitution in Eq. (3.23) gives the large-J signal

$$
\begin{aligned}
S_{\mathrm{d}}(t) = 2m^2 \frac{F_B}{F_A} F_C F_D \mathrm{Re}\Big\{ & e^{-i\varphi_{BA}+i\varphi_{DC}} \\
& \times \langle \uparrow_A (t)| \Big[\big(Q_{\mathrm{two}} - Q_{\mathrm{one}}\big) \Big(\frac{JK}{M^2} \, |\bar{1}\rangle \, p^{(\bar{1}2)} p^{(2\bar{1})} \langle \bar{1}| + \frac{K^2}{M^2} \, |\bar{1}\rangle \, p^{(\bar{1}2)} p^{(21)} \langle 1| \\
& - \frac{J^2}{M^2} \, |1\rangle \, p^{(12)} p^{(2\bar{1})} \langle \bar{1}| - \frac{JK}{M^2} \, |1\rangle \, p^{(12)} p^{(21)} \langle 1| \Big) \\
& - Q_{\mathrm{one}} |\bar{1}\rangle \, p^{(\bar{1}0)} p^{(01)} \langle 1| \Big] | \uparrow_A (t)\rangle \Big\} .
\end{aligned}
\tag{3.33}
$$

In the plausible situation where $Q_{\mathrm{two}} \approx Q_{\mathrm{one}}$, as happens when internal conversion from the doubly to the singly excited manifold occurs more rapidly than fluorescence (or any competing process by which population might leak from the doubly excited manifold), $S_{\mathrm{d}}(t)$ becomes an unobscured measure of the $|\bar{1}\rangle\langle 1|$ coherence (with greater fidelity to the degree that the pulse duration beats the energy-transfer timescale in addition to the slower timescale of interexciton amplitude transfer, and the reduced pulse propagators become scalars). In more general cases of unequal Q_{two} and Q_{one}, one could explore the possibility of combining signals with several different polarizations and hence different weightings of the contributing populations and coherences.

3.5 Illustrative Calculations

In this section we calculate WPI signals revealing the intersite and interexciton electronic coherence for several realizations of our spatially oriented EET dimer. As tests of the efficacy of the proposed strategy, these signals are compared to the actual coherence that develops and evolves between site or exciton states following short-pulse excitation to the dimer's singly excited manifold.

For an EET dimer with N identical internal vibrational modes for each of the monomers a and b, the site-state potential energies appearing in Eq. (3.2) are

$$V_{gg}(Q) = \sum_{i=1}^{N} \frac{\omega_i^2}{2} \left(q_{ai}^2 + q_{bi}^2 \right) , \tag{3.34}$$

$$V_{eg}(Q) = \epsilon_{eg} + \sum_{i=1}^{N} \frac{\omega_i^2}{2} \left[(q_{ai} - d_i)^2 + q_{bi}^2 \right] , \tag{3.35}$$

$$V_{ge}(Q) = \epsilon_{ge} + \sum_{i=1}^{N} \frac{\omega_i^2}{2} \left[q_{ai}^2 + (q_{bi} - d_i)^2 \right] , \tag{3.36}$$

$$V_{ee}(Q) = \epsilon_{ee} + \sum_{i=1}^{N} \frac{\omega_i^2}{2} \left[(q_{ai} - d_i)^2 + (q_{bi} - d_i)^2 \right] ; \tag{3.37}$$

we use mass-weighted coordinates and momenta q_{ai}, q_{bi}, p_{ai}, and p_{bi}. In cases of multiple modes per monomer ($N > 1$), the vibrational frequency ω_i is taken to decrease with increasing index i. The period of the highest frequency vibration $\tau_v = 2\pi/\omega_1$ serves as the unit of time in this section. The offset in bare electronic transition energy between "donor" and "acceptor" is usually assigned a value $\Delta\epsilon = \epsilon_{eg} - \epsilon_{ge} = \hbar\omega_1/2$, equal to half a quantum in the highest frequency vibration, but it is given other values in particular instances. We arbitrarily divide a fixed total Franck-Condon energy $\hbar\omega_1/4$ equally among the N modes in each monomer, so that $\omega_i^2 d_i^2/2 = \hbar\omega_1/4N$ or $d_i = \sqrt{\hbar\omega_1/2N\omega_i^2}$.

In all signal and coherence calculations, the pulse envelope takes the Gaussian form $f(t) = \exp\{-t^2/2\sigma^2\}$ for some pulse duration σ, and the carrier frequency is set to the average of the bare site-excitation frequencies, i.e., $\hbar\Omega = (\epsilon_{eg} + \epsilon_{ge})/2 \equiv \bar{\epsilon}$. Additionally, we assign an arbitrary, nonzero quantum yield Q_{one} to the singly excited manifold, while making the physically reasonable assumption $Q_{\text{two}} = Q_{\text{one}}$. The latter assumption simplifies the calculations by eliminating the contribution of the overlap $\langle \uparrow_A \uparrow_D \mid \uparrow_B \uparrow_C \rangle$ to the WPI signal (3.23).

In tracking electronic coherence within the singly excited manifold, we want to eliminate contributions due to the electric field strength of the laser pulses and to find the coherence that would result from a normalized initial wave packet. To accomplish this task in the small-J case, we abstract from the measured signal of Eq. (3.23) an "observed intersite coherence"

$$-\frac{S_{\rm d}(t;\varphi_{BA}-\varphi_{DC}=0)+iS_{\rm d}(t;\varphi_{BA}-\varphi_{DC}=\frac{\pi}{2})}{2Q_{\rm one}m^2\frac{F_B}{F_A}F_CF_D|p^{(eg\,gg)}_{\sigma=0}p^{(gg\,ge)}_{\sigma=0}|\langle\uparrow_A(t)|\uparrow_A(t)\rangle}=\frac{\langle\uparrow_A(t)|eg\rangle p^{(eg\,gg)}p^{(gg\,ge)}\langle ge|\uparrow_A(t)\rangle}{|p^{(eg\,gg)}_{\sigma=0}p^{(gg\,ge)}_{\sigma=0}|\langle\uparrow_A(t)|\uparrow_A(t)\rangle}\,, \tag{3.38}$$

noting that the reduced pulse propagators become scalars in the $\sigma = 0$ limit and that $\langle\uparrow_A\ (t)|\ \uparrow_A\ (t)\rangle$ is the population of the singly excited manifold generated by the A-pulse. In the large-J case, we correspondingly monitor the "observed interexciton coherence"

$$-\frac{S_{\rm d}(t;\varphi_{BA}-\varphi_{DC}=0)+iS_{\rm d}(t;\varphi_{BA}-\varphi_{DC}=\frac{\pi}{2})}{2Q_{\rm one}m^2\frac{F_B}{F_A}F_CF_D|p^{(\bar{1}0)}_{\sigma=0}p^{(01)}_{\sigma=0}|\langle\uparrow_A(t)|\uparrow_A\ (t)\rangle}=\frac{\langle\uparrow_A(t)|\bar{1}\rangle\, p^{(\bar{1}0)}p^{(01)}\,\langle 1|\uparrow_A(t)\rangle}{|p^{(\bar{1}0)}_{\sigma=0}p^{(01)}_{\sigma=0}|\langle\uparrow_A(t)|\uparrow_A(t)\rangle}\,. \tag{3.39}$$

In the small-J case, we compare the observed coherence (3.38) to the "actual intersite coherence" $\langle\uparrow_A\ (t)|eg\rangle\langle ge|\ \uparrow_A\ (t)\rangle/\langle\uparrow_A\ (t)|\ \uparrow_A\ (t)\rangle$. For large J, we compare (3.39) to the actual interexciton coherence $\langle\uparrow_A\ (t)|\bar{1}\rangle\langle 1|\ \uparrow_A\ (t)\rangle/\langle\uparrow_A\ (t)|\ \uparrow_A\ (t)\rangle$. These actual coherences serve as points of reference unaffected by the fidelity of the WPI coherence-detection process. The magnitudes of the observed and actual coherences are further compared with the maximum value $\sqrt{\langle\uparrow_A\ (t)|ge\rangle\langle ge|\ \uparrow_A\ (t)\rangle/\langle\uparrow_A\ (t)|\ \uparrow_A\ (t)\rangle}$ or $\sqrt{\langle\uparrow_A\ (t)|1\rangle\langle 1|\ \uparrow_A\ (t)\rangle/\langle\uparrow_A\ (t)|\ \uparrow_A\ (t)\rangle}$ consistent with the positive-definite nature of the reduced electronic density matrix.

3.5.1 Weak EET Coupling

In the weak EET-coupling case, the WPI signal is first-order in J, so we need not specify its value other than to require that it be smaller than $\hbar\omega_1/4$. The weak-EET plots in this subsection therefore display the normalized WPI-detected,

actual, and maximum coherences described above additionally divided by $J/\hbar\omega_1$ in order to remove dependence on the small, but otherwise unspecified J-value.

In the limit of arbitrarily short laser pulses, the A- and B-pulses faithfully copy the ground-state vibrational wave function into the eg-state, and the inverse Raman process later driven by C and D transfers a perfect copy of the propagated eg-state wave packet to ge. As an initial illustration, we therefore consider the WPI signal from our oriented EET model, which coincides exactly with the actual intersite coherence, in the simple instance where each monomer has just one Franck-Condon displaced vibrational mode.

It is possible to derive a semi-analytic expression for the WPI signal/actual coherence in this limiting case. With a change to center-of-mass and relative vibrational coordinates $Q = (q_b + q_a)/\sqrt{2}$ and $q = (q_b - q_a)/\sqrt{2}$ and their corresponding momenta, we see that the forms of the site potentials V_{eg} and V_{ge} differ only along the energy-transfer "reaction coordinate" q. The first-order approximation to the normalized overlap extracted from the whoopee signal (3.29) reduces to

$$\begin{aligned}\langle\phi_{eg}(t)|\phi_{ge}(t)\rangle &= -\frac{iJ}{\hbar}\int_0^t d\tau\,\langle\phi_0|[-t]^{(0)}_{eg\,eg}[t-\tau]^{(0)}_{ge\,ge}[\tau]^{(0)}_{eg\,eg}|\phi_0\rangle \qquad (3.40)\\ &= -\frac{iJ}{\hbar}\int_0^t d\tau\, e^{\frac{i\Delta\epsilon}{\hbar}(t-\tau)}\langle 0_{gg}|e^{-\beta(a^\dagger-a)}e^{2\beta(e^{i\omega t}a^\dagger-e^{-i\omega t}a)}e^{-2\beta(e^{i\omega\tau}a^\dagger-e^{-i\omega\tau}a)}e^{\beta(a^\dagger-a)}|0_{gg}\rangle\\ &= -\frac{iJ}{\hbar}\int_0^t d\tau\,\exp\left\{\frac{i\Delta\epsilon}{\hbar}(t-\tau)+4\beta^2\left(i\sin\omega t - i\sin\omega\tau + e^{-i\omega(t-\tau)}-1\right)\right\},\end{aligned}$$

where $|0_{gg}\rangle$ is the relative vibrational-mode ground state; $a^\dagger$ and a are the relative-mode creation and annihilation operators, respectively; $\beta \equiv \frac{d}{2}\sqrt{\frac{\omega}{\hbar}}$ is a dimensionless displacement parameter in the relative coordinate; and we let ω and d stand for ω_1 and d_1, respectively. The reduction to one dimension of relevant nuclear dynamics occurs only in the short-pulse limit. For example, since the $V_{eg} - V_{gg}$ difference

potential is a function of q_a alone, a nonzero-duration laser pulse produces an eg-state nuclear distribution in which the q and Q degrees of freedom are correlated.

Figure 32 depicts the absolute value and real and imaginary parts of the intersite coherence given by Eq. (3.40). That the coherence vanishes at even multiples of the vibrational period is a consequence of $\Delta\epsilon$'s half-quantum value. For

$$\begin{aligned}\langle\phi_{eg}(2\tau_v)|\phi_{ge}(2\tau_v)\rangle &= -\frac{iJ}{\hbar}\int_0^{2\tau_v} d\tau\ \exp\Big\{-\tfrac{i\omega\tau}{2}+4\beta^2(-i\sin\omega\tau+e^{i\omega\tau}-1)\Big\} \qquad (3.41)\\ &= -\frac{iJ}{\hbar}\int_0^{\tau_v} d\tau\ \exp\Big\{-\tfrac{i\omega\tau}{2}+4\beta^2(-i\sin\omega\tau+e^{i\omega\tau}-1)\Big\}\\ &\quad -\frac{iJ}{\hbar}e^{-i\frac{\omega}{2}\tau_v}\int_0^{\tau_v} d\bar{\tau}\ \exp\Big\{-\tfrac{i\omega\bar{\tau}}{2}+4\beta^2(-i\sin\omega\bar{\tau}+e^{i\omega\bar{\tau}}-1)\Big\};\end{aligned}$$

because $e^{-i\frac{\omega}{2}\tau_v}=-1$, the ge-state wave packet generated by energy transfer during the second τ_v interval cancels that generated during the first.

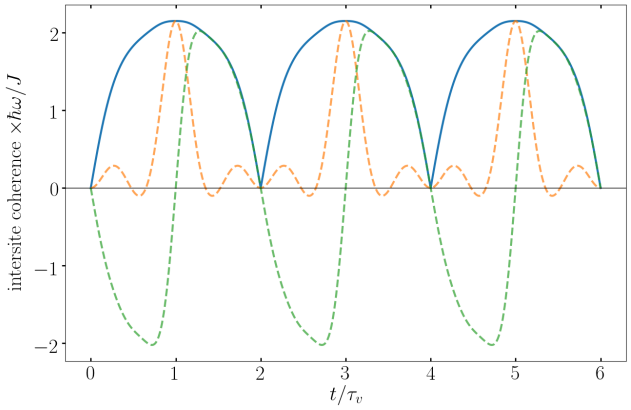

Figure 32. Short-pulse limit of WPI signal for weakly coupled EET model with one vibrational degree of freedom per monomer, coinciding with the actual intersite electronic coherence. Shown are the absolute value (blue), real part (gold), and imaginary part (green) of the overlap (3.40) divided by $J/\hbar\omega_1$.

Next we look into the viability of our intersite coherence-detection technique using more realistic, nonzero-duration pulses which remain abrupt compared to $h/|J|$, but are a longer-than-minuscule fraction of a vibrational period. Fig. 33

shows the absolute values of the "normalized" WPI signal, the actual coherence, and the maximum coherence for the model with one vibrational mode per monomer and a pulse length $\sigma = 0.09\tau_v$. Not only is the WPI signal different from that

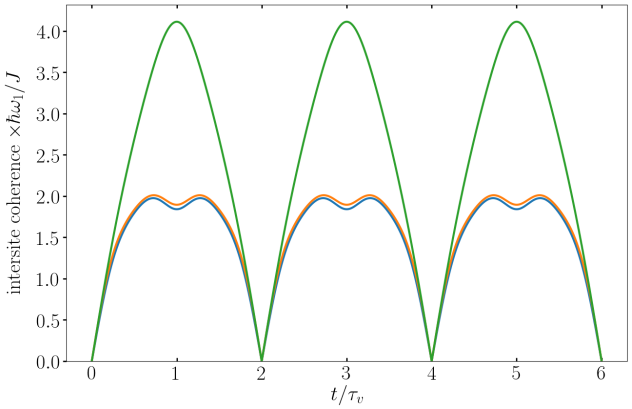

Figure 33. Absolute value of intersite coherence signal (blue), actual coherence (orange), and maximum possible coherence (green) from oriented, weak EET-coupling model with pulse durations $\sigma = 0.09\tau_v$.

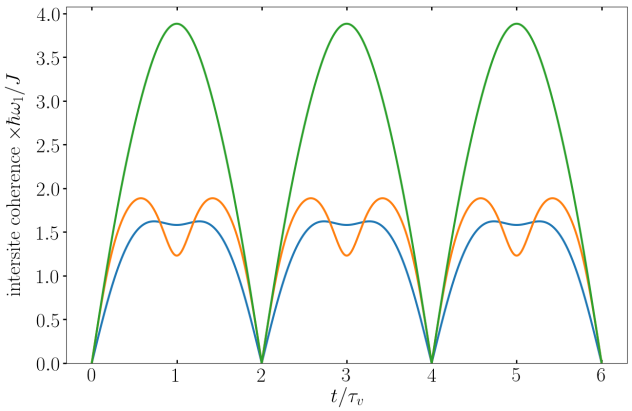

Figure 34. Intersite coherence signal (blue), actual coherence (orange), and maximum possible coherence (green) from oriented, weak EET-coupling model with pulse durations $\sigma = 0.27\tau_v$.

seen in Fig. 32, but the actual coherence generated by the A-pulse is changed as well because of the wave-packet-shaping effects of a nonzero-duration electronic excitation. The slight disparity between these two curves reflects imperfect

coherence detection due to the finite bandwidth of pulses C and D. Both of these absolute values are significantly smaller than the maximum size consistent with the positive-definiteness of the reduced electronic density matrix; this is a manifestation of intersite electronic decoherence born of differing wave-packet dynamics on the *eg*- and *ge*-surfaces. Fig. 34 further demonstrates the effects of pulse duration on the measurement. In this calculation with $\sigma = 0.27\tau_v$—a sizable fraction of the vibrational period—the signal becomes a less accurate measure of the actual intersite electronic coherence.

The presence of additional Franck-Condon-active vibrational degrees of freedom is expected to affect the evolution of intersite coherence. Cases of two and three modes per monomer, with the reorganization energy apportioned as described above and $\sigma = 0.09\tau_v$, are plotted in Figs. 35 and 36, respectively. In the $N = 2$ case of Fig. 35, for which $\omega_2 = \omega_1/5$, the signal remains reminiscent of the $N = 1$ case of Fig. 33 at short delays. But the scale is larger, because the higher-frequency vibration now carries less of the Franck-Condon energy. A complete period of motion in the lower-frequency mode occurs after $5\tau_v$. At twice this value, $t = 10\tau_v$, the signals vanish, as they did at $t = 2\tau_v$ for the single-mode-per-monomer case. The explanation for this vanishing is analogous to that for the $N = 1$ case. Figure 36 displays the results with $N = 3$, $\omega_2 = \omega_1/5$, and $\omega_3 = \omega_1/11$, up to the overall vibrational recurrence time $5 \times 11\tau_v$. After this time, all the plotted quantities diminish symmetrically with their earlier values and vanish at $t = 110\tau_v$ (not shown). At delay times shorter than its period of $11\tau_v$, the presence of the Franck-Condon displaced lowest frequency mode can be regarded as a stand-in for inhomogeneous broadening. By comparing Figs. 33, 35, and 36, we see that the highest value of the observed and actual intersite coherence increases as the

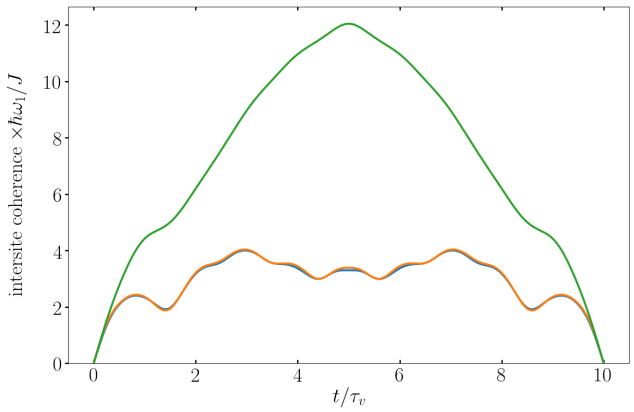

Figure 35. Intersite coherence signal, actual coherence, and maximum possible coherence from oriented, weak EET-coupling model with $N = 2$ modes per monomer and pulse durations $\sigma = 0.09\tau_v$. Color conventions are as in Figs. 33 and 34.

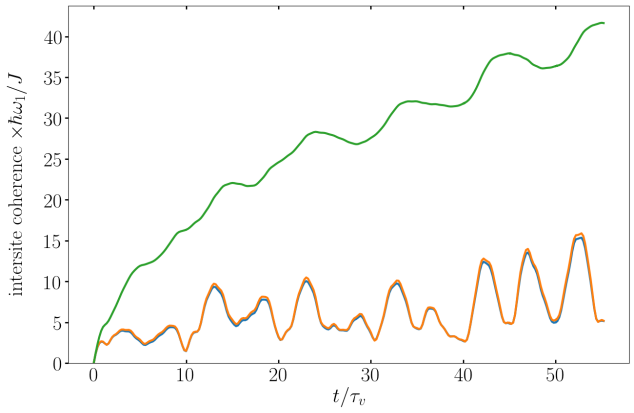

Figure 36. Intersite coherence signal, actual coherence, and maximum possible coherence from small-J model with $N = 3$ and the common pulse duration $\sigma = 0.09\tau_v$. Color conventions are those used previously.

Franck-Condon energy is divided among a larger number of vibrational modes; but these also become a smaller fraction of the highest value taken by the maximum coherence consistent with a positive-definite density matrix and the given intersite population transfer.

In light of recent interest in the effects of vibronic resonance on energy-transfer dynamics [49, 50], we return briefly to the simplest, one-mode-per-monomer case and consider alternative values, $\Delta\epsilon = 0$ and $\hbar\omega$, for the site-energy difference. In the first, equal-energies case, any difference-mode eigenstate in the donor well with vibrational quantum number n_{eg} is degenerate with the corresponding state in the acceptor well having $n_{ge} = n_{eg}$. When $\Delta\epsilon = \hbar\omega$, on the other hand, the vibronic resonance is between corresponding states obeying $n_{ge} = n_{eg} + 1$. Figure 37 reports semi-analytic calculations of the absolute value of the coherence signals for each of these cases with $N = 1$ and arbitrarily short pulses. In contrast with what is seen for the preceding $\Delta\epsilon = \hbar\omega/2$ cases, both of these oscillatory intersite coherence signals exhibit steady cycle-averaged growth, with the $\Delta\epsilon = 0$ coherence increasing roughly three times as fast as the one with $\Delta\epsilon = \hbar\omega$. In the presence of vibronic resonance, the first-order perturbative treatment underlying Eq. (3.40) would, however, become insufficient beyond some time inversely proportional to the actual size of the coupling constant J.

Qualitative semiclassical consideration of the dynamics of the eg and ge wave packets, whose overlap determines the coherence, provides some insight into the differences between the two signals in Fig. 37. Figure 38 shows phase-space trajectories for the donor- and acceptor-state wave packets in both cases. We consider only the difference mode, as this vibration mediates energy transfer. Ignoring the nonzero (in fact, quite sizeable) spatial widths of the wave packets,

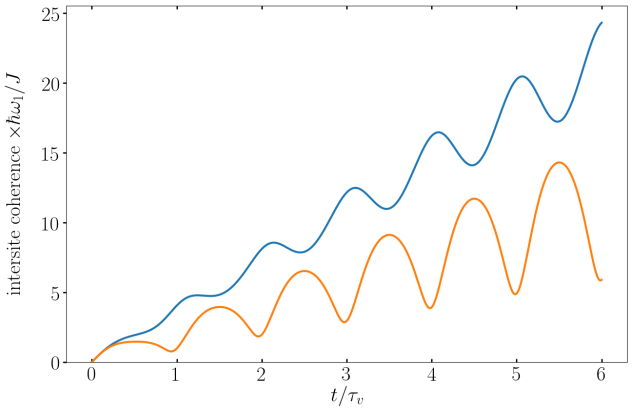

Figure 37. Short-pulse intersite coherence signal from small-J model with $N = 1$ for the cases of equal site energies (blue) and $\Delta\epsilon = \hbar\omega$ (gold).

energy transfer would be expected to occur when the center of the eg wave packet is near the crossing seam between the eg and ge potentials. This point on the eg trajectories, marked by a red dot in each panel, is also the semiclassical point of origin of the EET-born ge trajectory. The crossing seam lies at $q = 0$ for $\Delta\epsilon = 0$ and at $q = -\sqrt{2}d$ for $\Delta\epsilon = \hbar\omega$.

In the case of equal site energies, the donor trajectory $(\omega\langle q\rangle_{eg}, \langle p\rangle_{eg})$ circles the point $(-\frac{\omega d}{\sqrt{2}}, 0)$ in clockwise fashion, while $(\omega\langle q\rangle_{ge}, \langle p\rangle_{ge})$ circles clockwise about $(\frac{\omega d}{\sqrt{2}}, 0)$. The crossing region is indicated by a grey swath of (perhaps exaggerated) width $\frac{\omega d}{\sqrt{2}}$ straddling the $\omega q = 0$ line in the left panel of Fig. 38. At the edges of this stripe, the site potentials differ by plus or minus $\omega^2 d^2/2 = \hbar\omega/4$, a splitting more than large enough to preclude EET under weak coupling. In the $\Delta\epsilon = \hbar\omega$ situation, both trajectories still circulate in the same sense about the same centers. But with the crossing seam now at $\omega q = -\omega\sqrt{2}d$, the phase-space path of the ge wave packet has a radius three times larger than the eg wave packet's.

Considering the limiting case of a phase-space path of radius r and a crossing stripe of much smaller width w, a trignometric argument shows that,

after passing the crossing point, the phase point remains in the resonance region for a time $\frac{1}{\omega}\sqrt{\frac{w}{r}}$. We therefore expect an amplitude increment on the acceptor potential to remain accessible for constructive accumulation with subsequent or prior increments for a time that is about $\sqrt{3}$ longer in the $\Delta\epsilon = 0$ case than when $\Delta\epsilon = \hbar\omega$. This reasoning is at least qualitatively consistent with the faster cycle-averaged growth of intersite coherence in the former instance.

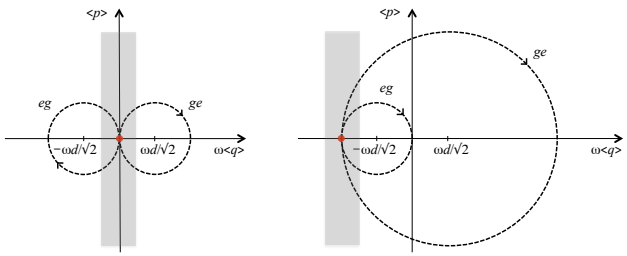

Figure 38. Qualitative difference-mode phase-space trajectories for the wave packets $|\phi_{eg}\rangle$ and $|\phi_{ge}\rangle$ which underlie the signals in Fig. 37. In the left plot, $\Delta\epsilon = 0$, while $\Delta\epsilon = \hbar\omega$ on the right. Red dots mark the points on these trajectories at which $V_{eg} = V_{ge}$, where energy transfer is most facile. The shaded regions are those within which potential-energy difference may be small enough to allow energy transfer. Difference coordinates at the potential minima are indicated by tick marks.

It is seen in Fig. 37 that the change in the absolute value of the intersite coherence signal between successive local minima in the $\Delta\epsilon = 0$ case also exceeds that between successive minima for $\Delta\epsilon = \hbar\omega$. Successive minima occur at $t \approx (n - \frac{1}{2})\tau_v$ and $(n + \frac{1}{2})\tau_v$ in the first instance and at $t \approx n\tau_v$ and $(n + 1)\tau_v$ in the second. Straightforward calculations starting from Eq. (3.40) show that for our weakly coupled $\Delta\epsilon = 0$ dimer, we have

$$\begin{aligned}
&\big\langle \phi_{eg}\big((n+\tfrac{1}{2})\tau_v\big)\big|\phi_{ge}\big((n+\tfrac{1}{2})\tau_v\big)\big\rangle - \big\langle \phi_{eg}\big((n-\tfrac{1}{2})\tau_v\big)\big|\phi_{ge}\big((n-\tfrac{1}{2})\tau_v\big)\big\rangle \\
&= -\frac{iJ}{\hbar}\int_{(n-\frac{1}{2})\tau_v}^{(n+\frac{1}{2})\tau_v} d\tau\, \exp\big\{-4\beta^2(1+e^{i\omega\tau}+i\sin\omega\tau)\big\} \\
&= -\frac{2iJ}{\hbar\omega}\int_0^{\pi} d\theta\, e^{-\frac{1}{2}(1+\cos\theta)}\cos(\sin\theta) \cong -\frac{iJ}{\hbar\omega}3.129\,, \qquad (3.42)
\end{aligned}$$

while for the dimer with $\Delta\epsilon = \hbar\omega$, we find

$$\begin{aligned}
&\big\langle \phi_{eg}\big((n+1)\tau_v\big)\big|\phi_{ge}\big((n+1)\tau_v\big)\big\rangle - \big\langle \phi_{eg}(n\tau_v)\big|\phi_{ge}(n\tau_v)\big\rangle \\
&= -\frac{iJ}{\hbar}\int_{n\tau_v}^{(n+1)\tau_v} d\tau\, \exp\big\{-i\omega\tau + 4\beta^2(\cos\omega\tau - 1)\big\} \\
&= \frac{2iJ}{\hbar\omega}\int_0^{\pi} d\theta\, e^{-\frac{1}{2}(1+\cos\theta)}\cos\theta \cong \frac{iJ}{\hbar\omega}0.9828\,. \qquad (3.43)
\end{aligned}$$

The difference in magnitude between the last members of Eqs. (3.42) and (3.43) is accounted for by the fact that $\sin\theta < \theta$ for θ between zero and π, an interval on which $\cos\theta$ is a monotonically decreasing function.

3.5.2 Strong EET Coupling

We now consider a situation in which the energy-transfer coupling is larger than the electronic-vibrational interaction. Specifically, we keep the other molecular parameters the same as before (including $\Delta\epsilon = \hbar\omega_1/2$), but set $J = \sqrt{\frac{3}{2}}\,\hbar\omega_1$. The pulse polarizations are different for the large-J case, in order to target the single-exciton electronic states. For the chosen $\Delta\epsilon$ and J, the polarizations become $\mathbf{e}_A = \mathbf{e}_B = \mathbf{e}_C = \sqrt{\frac{3}{5}}\,\hat{\mathbf{x}} + \sqrt{\frac{2}{5}}\,\hat{\mathbf{y}}$, aligned with $\mathbf{m}_{\bar{1}0}$, and $\mathbf{e}_D = -\sqrt{\frac{2}{5}}\,\hat{\mathbf{x}} + \sqrt{\frac{3}{5}}\,\hat{\mathbf{y}}$, aligned with $\mathbf{m}_{10}$ (see Section 3.2). The singly-to-doubly-excited transition moments $\mathbf{m}_{2\bar{1}} = \sqrt{\frac{2}{5}}\,\hat{\mathbf{x}} + \sqrt{\frac{3}{5}}\,\hat{\mathbf{y}}$ and $\mathbf{m}_{21} = \sqrt{\frac{3}{5}}\,\hat{\mathbf{x}} - \sqrt{\frac{2}{5}}\,\hat{\mathbf{y}}$ are mutually perpendicular, but do not coincide with the ground-to-singly-excited moments.

Appendix B spells out a perturbation theory treatment of the strong-coupling case. We calculate the WPI-coherence signal at first order in the coupling between the $\bar{1}$ and 1 excitonic states (see Eq. (3.10)). In the short-pulse limit, the observed interexciton coherence (3.39) following initial excitation of the $\bar{1}$-state

coincides with the actual coherence. In this limit, the signal becomes,

$$\frac{\langle\phi_0|p^{(0\bar{1})}[-t]^{(0)}_{\bar{1}\bar{1}}[t]^{(1)}_{1\bar{1}}p^{(\bar{1}0)}|\phi_0\rangle}{\langle\phi_0|p^{(0\bar{1})}p^{(\bar{1}0)}|\phi_0\rangle} = \langle\phi_0|[-t]^{(0)}_{\bar{1}\bar{1}}[t]^{(1)}_{1\bar{1}}|\phi_0\rangle$$
$$= i\frac{J}{M}\sum_{j=1}^{N}\beta_j\frac{\omega_j d_j}{2}\sqrt{\frac{\omega_j}{\hbar}}\int_0^t d\tau e^{\frac{2iM}{\hbar}(t-\tau)}\left(e^{i\omega_j\tau} - 2e^{-i\omega_j(t-\tau)} + e^{-i\omega_j\tau}\right)$$
$$\times\prod_{k=1}^{N} e^{4\beta_k^2(e^{-i\omega_k(t-\tau)}+i\sin\omega_k t - i\sin\omega_k\tau - 1)}, \tag{3.44}$$

where $|\phi_0\rangle$ is the N-dimensional vibrational ground state, and $\beta_j = \frac{K}{M}\frac{d_j}{2}\sqrt{\frac{\omega_j}{\hbar}}$.

The coherence signal (3.44) is plotted in Fig. 39 for the case in which each monomer has a single vibrational mode. The interexciton coherence vanishes at

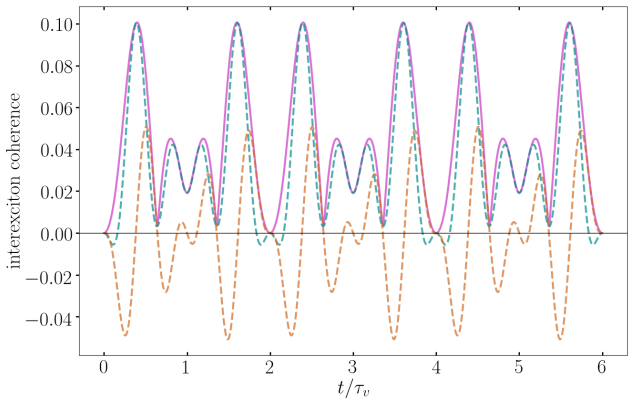

Figure 39. Interexciton coherence signal from a dimer with one internal vibrational mode per monomer in the case of arbitrarily abrupt laser pulses. Shown are the absolute value (purple), the real part (cyan), and the imaginary part (brown) of the electronic coherence following excitation of the $\bar{1}$-state at $t = 0$.

integer multiples of $2\tau_v$ for a different reason than in the weak-coupling case. With the chosen values of J and $\Delta\epsilon$, the interexciton splitting works out to $2M = 5\hbar\omega/2$ (we let ω stand for ω_1 in the rest of this subsection). Since the difference-mode displacement parameter takes the small value $\beta = 1/10\sqrt{2}$, we can approximate Eq.

(3.44) at first order in β and carry out the τ-integration, finding

$$\langle\phi_0|[-t]^{(0)}_{\bar{1}\bar{1}}[t]^{(1)}_{1\bar{1}}|\phi_0\rangle \cong -\frac{J}{M}\beta d\sqrt{\frac{\omega}{\hbar}}e^{i\frac{5}{2}\omega t}\left\{\tfrac{1}{3}\left(e^{-i\frac{3}{2}\omega t}-1\right)\left(1-2e^{-i\omega t}\right)+\tfrac{1}{7}\left(e^{-i\frac{7}{2}\omega t}-1\right)\right\}. \tag{3.45}$$

The splitting $2M$ between the excitonic states happens to be a half-odd multiple of $\hbar\omega$, and the interexciton coupling is linear in $a^\dagger + a$ (see Appendix B). The electronic nutation process [51] that governs interexciton amplitude transfer also involves the gain or loss of a vibrational quantum in the difference-mode, occurring here at frequencies $\frac{5}{2}\omega \pm \omega$. Contributions at both of these frequencies simultaneously complete nutation cycles at $t = 2n\tau_v$; both terms in curly brackets in Eq. (3.45) vanish at these times, corresponding to no net transfer of amplitude.

Figure 40 shows the absolute value of the coherence signal for the same system as it would be prepared by photoexcitation of the $\bar{1}$-state and observed using pulses of duration $\sigma = 0.05\tau_v$. Also plotted is the maximum value the interexciton coherence could take at as a function of time, consistent with a positive-definite reduced electronic density matrix and the population that has been transferred from the $\bar{1}$- to the 1-state. Both are calculated numerically using the methods of Appendix B. It is seen that the coherence signal observed with finite-duration pulses offers an accurate account of that which would be prepared and measured ideally with much shorter pulses.

Figure 41 explores the effects on the observed interexciton coherence of additional vibrational modes. Plotted there is the magnitude of the coherence signal for cases with one, two, and three vibrational modes per monomer, as it would be measured with arbitrarily short pulses. Each monomer's total Franck-Condon energy is partitioned equally among its modes by the same prescription as described above for the weak-coupling case, and again the mode frequencies

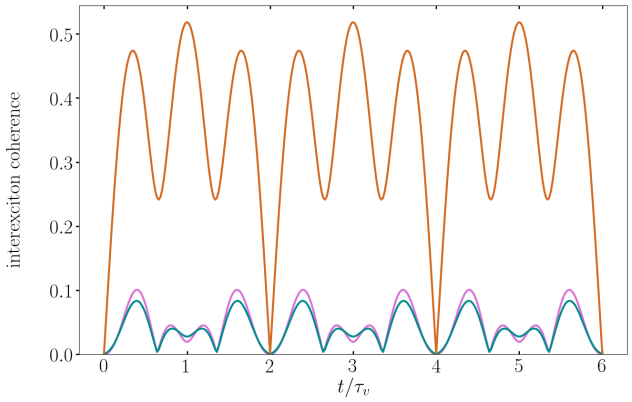

Figure 40. Calculated interexciton coherence signal from the dimer with one mode per monomer, as it would be generated and observed in wave-packet interferometry experiments with laser pulses of duration $\sigma = 0.05\tau_v$. The absolute value of the coherence signal and the corresponding maximum coherence consistent with a positive-definite reduced electronic density matrix are plotted as cyan and brown lines, respectively. The purple curve (coinciding with that shown in Fig. 39) is the coherence signal generated with arbitrarily short pulses; the corresponding maximal coherence (not shown) is almost indistinguishable from the brown line.

are $\omega_1 = \omega$, $\omega_2 = \omega/5$, and $\omega_3 = \omega/11$. When equally dividing the Franck-Condon energy among the modes, the prefactors $\beta_j \frac{\omega_j d_j}{2} \sqrt{\frac{\omega_j}{\hbar}} = \frac{K}{M} \frac{\omega}{8N}$ in Eq. (3.44) become uniform. Adding the lower frequency modes introduces new electronic nutation frequencies $\frac{5}{2}\omega \pm \omega_j$ which are closer but not equal to the exciton splitting $2M/\hbar = 5\omega/2$; the periodic disappearance of interexciton coherence observed in the one-mode-per-monomer case is extinguished. In the case of two vibrational modes per monomer, for instance, the interexciton coherence signal (giving rise to the cyan trace in Fig. 41) can be approximated at first order in β_1 and β_2 as

$$\langle \phi_0 | [-t]^{(0)}_{\bar{1}\bar{1}} [t]^{(1)}_{1\bar{1}} | \phi_0 \rangle = -\frac{J}{80M} e^{i\frac{5}{2}\omega t} \left[\frac{e^{-i\frac{3}{2}\omega t} - 1}{3/2} \left(1 - 2e^{-i\omega t}\right) + \frac{e^{-i\frac{7}{2}\omega t} - 1}{7/2} + \frac{e^{-i\frac{23}{10}\omega t} - 1}{23/10} \left(1 - 2e^{-\frac{i}{5}\omega t}\right) + \frac{e^{-i\frac{27}{10}\omega t} - 1}{27/10} \right]. \quad (3.46)$$

A similar approximate expression can be worked out for the $N = 3$ situation.

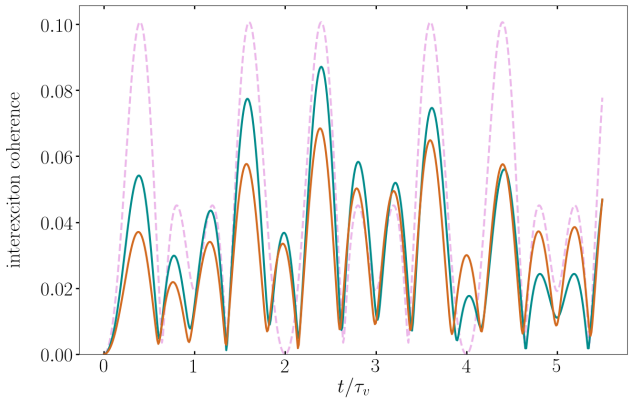

Figure 41. The magnitude of the interexciton coherence signal in a dimer with three (brown), two (cyan), and one (dashed purple) internal vibrational mode(s) equally sharing a fixed total Franck-Condon energy. All pulses are taken to be arbitrarily short.

The special case of monomers with equal site energy proves to be an interesting one under strong EET coupling. Without changing the other parameters, we set $\Delta\epsilon = 0$. The interexciton transition moments now become $\mathbf{m}_{\bar{1}0} = \mathbf{m}_{2\bar{1}} = \frac{m}{\sqrt{2}}(\hat{\mathbf{x}} + \hat{\mathbf{y}})$ and $\mathbf{m}_{10} = -\mathbf{m}_{21} = \frac{m}{\sqrt{2}}(-\hat{\mathbf{x}} + \hat{\mathbf{y}})$. We align $\mathbf{e}_A$, $\mathbf{e}_B$, and $\mathbf{e}_C$ with the former and $\mathbf{e}_D$ with the latter. Figure 42 displays semi-analytic calculations for dimers with one, two, and three vibrational modes in each monomer. Although amplitude transfer from $\bar{1}$ to 1 occurs via electronic nutation, as manifested in the nonzero maximum-coherence traces, no interexciton coherence develops, regardless of the number of vibrational modes. This behavior is predicted by Eq. (3.44), where it is seen that any contribution to the coherence must be proportional to one of the β_j; these in turn are proportional to $K = \Delta\epsilon/2$, which vanishes when the site energies are equal.

A more physical picture follows from the analysis in Appendix B: Equation (B.3) shows that when the site energies are equal ($K = 0$), the diabatic potential surfaces in the $\bar{1}$- and 1-states have the same form and are not displaced from

the electronic ground-state potential along the difference-mode coordinates q_j. Since every contribution to the interexciton coupling Hamiltonian of Eq. (B.4) is linear in one of the q_j, amplitude transfer between the exciton states is always accompanied by a change in vibrational quantum number in the equal site-energies case. Amplitude transferred from one exciton state to the othere is therefore "born completely entangled" with the vibrational environment and cannot give rise to interexcitonic coherence.

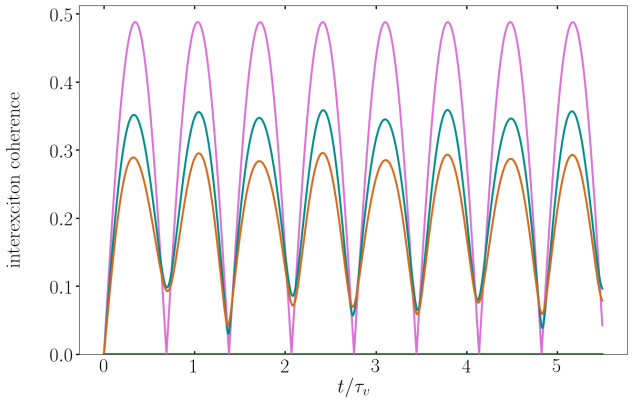

Figure 42. Flat green line shows the vanishing interexciton coherence, regardless of the number of vibrational modes, for the case of equal site energies. The maximum amount of interexciton coherence that would be consistent with the interexciton population transfer and a positive-definite reduced electronic density matrix is plotted in purple, cyan, and brown for dimers with one, two, and three vibrational mode(s) per monomer, respectively. All pulses are arbitrarily short.

The physical dynamics of interexciton amplitude transfer and coherence generation, elaborated here and in Appendix B, are qualitatively different from those of intersite amplitude transfer and coherence illustrated in Section 3.5.1. The upper and lower exciton states under consideration in the strong EET-coupling case are well separated in energy compared to the size of the interexciton coupling (see Eq. (3.10)), and interexciton amplitude transfer is therefore electronically nonresonant and occurs by a nutation process. On the other hand, the site states

used as an electronic basis in the case of weak EET coupling are energetically well separated for *most* nuclear coordinate values (see Eq. (3.2)), but the intersection seam between the site-excited potential energy surfaces is the location of the most efficient, resonant intersite amplitude transfer. In addition, whereas the interexciton amplitude-transfer coupling is linear in each of the nuclear coordinate operators, the intersite coupling operator has a leading zeroth order component. These differences account, in particular, for the differing trends observed in the dependence of the maximum possible coherence on the number of Franck-Condon active vibrations in each monomer. In the strong EET-coupling case seen in Fig. 41, the maximum interexciton coherence tends to decrease with an increasing number of vibrational modes. In the weak-coupling cases of Figs. 33, 35, and 36, the maximum intersite coherence increases with an increasing number of modes.

3.6 Discussion

The preceding sections outline a strategy for observing the off-diagonal elements of the reduced electronic density matrix within the singly excited manifold of a spatially oriented EET dimer. Electronic coherence detection in either the site or the exciton basis would support reconstruction of the time-evolving reduced electronic density matrix; determination of the corresponding diagonal elements—site-state or excitonic populations—can be accomplished using time-resolved pump-probe or fluorescence up-conversion spectroscopy [52, 53, 28].

It emerged from our analysis that the sought-after intersite or interexciton coherences reside in the pump-probe slice through a 2D-WPI data set, the $t_{BA} = t_{DC} = 0$ trace within a collection of signals spanning $\{t_{BA}, t_{CB}, t_{DC}\}$. But revealing the reduced electronic density matrix in the singly excited manifold is not the be-all and end-all of ultrafast spectroscopy on energy-transfer systems; much additional

information on the nuclear dynamics accompanying EET is to be gained from the full 2D-WPI signal over variable ranges in all three interpulse delays. Several interesting patterns are seen in our signal calculations, but these are meant to illustrate the capabilities of electronic coherence detection; the dimer models are simple, and the calculated signals are not likely to accurately portray those from more realistic systems.

An oriented ensemble of EET multimers could consist of the visible light-absorbing chromophores in a single crystal of macromolecular light-harvesting antennas from a photosynthetic organism [54] or an inorganic crystal dyed with synthetic organic dimers or higher multimers [55, 56, 57]. With the advent of fluorescence-detected single-molecule multidimensional electronic spectroscopy [58],[3] it should also become possible to perform measurements of the kind advocated here on individual EET dimers embedded in a solid medium. In the related context of inverting pump-probe data to effect quantum-state tomography (see below), Hoyer and Whaley have investigated how the absence of inhomogeneous broadening in a single-molecule experiment can improve the fidelity of the reconstruction compared with oriented or isotropic macroscopic ensembles [59].

If experiments of the kind proposed are to be carried out on macroscopic ensembles, inhomogeneities in the site-energies and intermonomer coupling would likely come into play. Both forms of inhomogeneity would be expected generally to diminish the size and limit the longevity of either intersite or interexciton coherence. These issues are addressed only obliquely here (in Section 3.5.1) and deserve further detailed investigation.

[3] Andy Marcus, private communication.

As is detailed above, it is preferable to track electronic coherence in the site-excited basis when the EET coupling is smaller in size than the local difference in site-state energies over most of the dynamically accessed range of nuclear motion. An excitonic description is more appropriate when the inter-exciton splitting (roughly twice the EET coupling) exceeds the magnitude of the interexciton couplng (which is itself similar in size the electronic-vibrational interaction). In the intermediate regime where neither criterion applies, it would be about equally practical to monitor the electronic coherence in either of these two nuclear coordinate-independent bases. In this case, however, amplitude transfer between the singly excited electronic states in either basis would have to be treated nonperturbatively, as it could not be accurately accounted for with low-order time-dependent perturbation theory.

Experimental determination of either the intersite or interexciton coherence, along with the corresponding electronic state populations, as envisaged here, can be compared with various techniques for quantum process tomography [60, 61, 62]. Both undertakings make use of optically phase-coherent ultrafast spectroscopy data to follow the open-system dynamics in the singly excited manifold of an energy-transfer system. Under consideration in the present study is the design of experiments to monitor as directly as possible the elements of the evolving reduced electronic density matrix. We wish to mobilize procedures for molecular state determination, akin to those originally developed for isolated systems [63, 64], to apply to an open quantum "subsystem" comprising the singly excited states of an energy-transfer complex embedded in the "environment" of the its intra- and intermolecular nuclear degrees of freedom. In contrast, quantum process tomography outlines a procedure for inverting polarization and pulse-spectrum

dependent multidimensional electronic or other ultrafast spectroscopy data to obtain a completely positive, trace-preserving map for the one-exciton manifold. The underlying theory has been worked out in several spectroscopic contexts. This procedure has been successfully implemented using transient-grating data from organic double-walled nanotubes [65]. The description of the nuclear dynamics underlying the observed optical signals as well as the treatment of pulsed-laser excitation remain somewhat idealized in existing treatments. Datta and co-workers have investigated the possibility of implementing a simplified test for the role of interexciton coherence in energy transfer based on partial quantum process tomography [66].

The assumed existence in quantum process tomography of a map χ specifying the reduced electronic density matrix $\rho_{\mathrm{el}}(t) = \chi(t)\rho_{\mathrm{el}}(0)$ depends on the preparation of an initially photo-excited state $\rho_{\mathrm{total}}(0) = \rho_{\mathrm{el}}(0) \otimes \rho_{\mathrm{nuc}}(0)$ in which the electronic and nuclear degrees of freedom are uncorrelated. It applies only to arbitrary $\rho_{\mathrm{el}}(0)$ accompanied by the same particular nuclear distribution $\rho_{\mathrm{nuc}}(0)$. In practice, the preparation of such an uncorrelated initial state would appear to require excitation pulses of duration short enough to "freeze" nuclear motion entirely. In comparison, although the fidelity of the coherence-detection procedure presented here relies on the brevity of the detection pulses C and D, it should function as desired regardless of the spectral and temporal properties of the pulses which create the initial electronically excited state.

Apart from its intrinsic interest, reconstruction of the reduced electronic density matrix would enable evaluation of a variety of correlation functions that enter the so-called Leggett-Garg parameters [67]. These quantities obey certain inequalities under the postulates of macroscopic realism; their violation would

signify the presence of intrinsically quantum mechanical behavior in energy transfer. Recent simulations of Leggett-Garg parameters for the Fenna-Matthews-Olson light-harvesting complex predict some violations of the requisite inequalities even at room temperature [67]. These simulations made a number of dynamical assumptions, including Markovian behavior in energy transport. In addition, this work did not adduce a specific experimental strategy for evaluating the simulated Leggett-Garg parameters.

Interestingly, account has been taken of *xxxy*-polarized two-dimensional electronic spectroscopy signals from a chiral light-harvesting multimer [68, 69]. In simulations of an isotropic ensemble of Fenna-Matthews-Olson complexes, this polarization was included along with several other chirally-induced contributions to 2D interferograms. The authors employed a genetic algorithm in a successful search for combinations of differently polarized signals which emphasize peaks associated with selected energy-transfer pathways and de-emphasize others. Better spectral resolution was achieved than with the nonchiral *xxxx* polarization combination alone, but no discussion was given of the possible use of *xxxy* or other polarizations on spatially oriented, not necessarily chiral complexes to track the evolution of intersite or interexciton electronic coherence.

3.7 Conclusions

In the theoretical study reported here, we identify an experimental strategy for isolating the off-diagonal elements of an energy-transfer dimer's reduced electronic density matrix in the singly excited subspace. We show that with appropriately chosen polarizations, the pump-probe limit of the two-dimensional wave-packet interferometry signal from a spatially oriented ensemble or an individual dimer with nonparallel site-transition moments faithfully tracks either

the intersite coherence—in the case of weak energy-transfer coupling—or the interexciton coherence—under strong coupling. Although the model dimer used for illustrative signal calculations is a simple one, the signals exhibited interesting and interpretable dependence on the number and frequencies of the vibrational modes coupled to each site-transition, the difference in monomer site energies, and the energy-transfer coupling strength.

Signal calculations based on the electronic potential energy surfaces and transition dipole moments determined via an *ab initio* electronic structure treatment of an experimentally targeted species would be a natural next step for theoretical development. Another question of interest for future investigation might be the discernibility of intersite and interexciton electronic coherence from isotropic samples of chiral energy-transfer systems.

3.8 Bridge

This chapter has provided a wave-packet interferometry experiment that allows for the detection of electronic coherence. The utility of dynamical approaches to the calculation of spectroscopic signals is highlighted by this work; devising an experiment to detect the coherence follows naturally from framing the theory on the dynamics of wave packets and realizing that the electronic coherence is simply the overlap of particular wave packets. The next chapter, though no longer focused on spectroscopy, provides a dynamical framing of electronic structure theory, a subject that is traditionally considered from the point of view of stationary wave functions.

CHAPTER IV

EXPLORING A SPECTRAL-FILTERING APPROACH TO ELECTRONIC STRUCTURE CALCULATIONS

This work is currently unpublished with a manuscript in preparation. Alexis Kiessling derived the expressions, performed the calculations, and wrote the manuscript; Jeffrey Cina provided much help with all aspects of the work. Jeffrey Cina was the principal investigator for this work.

4.1 Introduction

The electronic structure of a molecule holds useful information and is capable of providing a great deal of chemical insight. This structure is a spectrum of eigenstates of the molecule's electronic Hamiltonian, and though this structure is static in nature, it can be used to gain insight into dynamical phenomena. For example, electronic structure can help provide interpretations of such observable quantities as absorption spectra or reaction products [70, 71]. Solving for these eigenstates analytically is essentially impossible except for one-electron systems, and an enormous effort has been made over the past eighty years to develop approximate numerical solutions [72, 73]. One of the earliest approximations, the Hartree-Fock approximation (HF) [74], is still used today. HF uses a set of basis functions to find the single Slater determinant with a minimum energy, calculated as the determinant's expectation value of the Hamiltonian. Taking advantage of the variational principle, the determinant is iteratively improved to approximate the ground-state wave function [75].

HF serves as the starting point for many calculations; some examples include configuration interaction calculations and coupled cluster theory [72]. These calculations use many configurations of the "excited" form of the HF ground-state

Slater determinant to better approximate the ground state. In some sense, these methods are biased towards the ground state, starting from the best HF ground state to further the approximation. Additionally, for many-electron systems, these methods require combining a large number of terms. While the success of these techniques in calculating observables is apparent [76], requiring so many corrections suggests that it remains worthwhile to investigate alternative approaches. There are already several methods that do not start from a HF ground state, such as Quantum Monte Carlo (QMC) and Density Functional Theory (DFT) [77, 78]. These methods face some challenges as well, however. Similarly to HF-based methods, DFT must attempt to approximate electron correlation [78], and QMC methods require modifications to retrieve excited states [79, 80]. Ultimately, the effectiveness of these tools relative to each other depends on many practical considerations. Here, we explore another potential tool to numerically approximate eigenstates of an electronic Hamiltonian.

We attempt to build upon an idea originally proposed by Heller in the context of semiclassically-propagated nuclear wave packets [81, 82]. Though the focus of that work was dynamics, Heller noted that one could obtain eigenstates from a wave packet's time evolution by Fourier transformation from the time domain to the frequency domain. This approach could be thought of as a spectral filtering technique. In the following, we apply this technique to fermionic systems, which follow antisymmetry rules. The requirement of antisymmetry can be easily imposed in spectral filtering; as long as the initial wave packet is antisymmetric (that is, for example, a Slater determinant), the resulting eigenstates will have the correct antisymmetry. What is more, the dynamical approach automatically fully incorporates the effects of electron correlation without its separate consideration.

Initially approximating the electron-electron interaction as an interaction with an averaged field, as is done in methods based on HF, is unnecessary. This approach lends itself to semiclassical approaches to time evolution (or other strategies based on approximate trial wave functions defined by time-dependent parameters), and we compare the simplest such possibility to an exact approach.

This paper is outlined as follows: Section 4.2 presents a brief theoretical background on this technique and the example system to be explored; Section 4.3 describes a direct numerical integration approach and its results; Section 4.4 implements a semiclassical implementation; Section 4.5 compares the results obtained from a simple Hartree-Fock calculation to those obtained by direct numerical integration; Section 4.6 considers the simplest application of Section 4.4's semiclassical implementation to a Coulomb potential; and Section 4.7 ends the paper with a discussion of the possible merits of this approach and its limitations.

4.2 Theory

The general strategy of the approach is to approximate the unnormalized kets $|\tilde{\Psi}(\omega)\rangle$, which are given by

$$|\tilde{\Psi}(\omega)\rangle \equiv \int_{-\infty}^{\infty} dt\, e^{i\omega t} |\Psi(t)\rangle \,. \tag{4.1}$$

If the time evolution of $|\Psi(t)\rangle$ is governed by a time-independent Hamiltonian, then

$$|\tilde{\Psi}(\omega)\rangle = 2\pi \sum_n c_n \delta(\omega - \omega_n) |n\rangle \,, \tag{4.2}$$

where $c_n \equiv \langle n|\Psi(0)\rangle$ and the eigenstates $|n\rangle$ obey $H|n\rangle = E_n|n\rangle = \omega_n|n\rangle$; $\hbar = 1$ throughout. If no degenerate eigenstates exist, the Fourier coefficients each correspond to a single eigenstate $|n\rangle$ and eigenenergy E_n, and a portion of the eigenspectrum of H is given by $|\tilde{\Psi}(\omega)\rangle$. The c_ns determine whether or not a given eigenstate is recovered by the Fourier transformation.

In practice, we numerically approximate $|\tilde{\Psi}(\omega)\rangle$ using the Riemann sum

$$|\tilde{\Psi}(\omega)\rangle \cong \sum_{k=-N_t}^{N_t} \delta t \, e^{i\omega t_k} g(t_k) \, |\Psi(t_k)\rangle \,, \tag{4.3}$$

where $t_{\pm N_t} = \pm T$ and $\delta t = t_i - t_{i-1}$. The window function, $g(t)$, converges the sum between $t = -T$ and $t = T$. There are many possible choices of window function; here, we set $g(t) = \gamma \cos \frac{\pi t}{2T} \Theta(T+t)\Theta(T-t)$, where $\Theta(t)$ denotes the Heaviside step function and $\gamma = \frac{1}{\sqrt{2\pi T}}$ ensures that

$$\int_{-\infty}^{\infty} d\omega \; \langle \tilde{\Psi}(\omega) | \tilde{\Psi}(\omega) \rangle = 1. \tag{4.4}$$

The function $\tilde{f}(\omega)$, given by

$$\tilde{f}(\omega) \equiv \langle \tilde{\Psi}(\omega) | \tilde{\Psi}(\omega) \rangle \,, \tag{4.5}$$

is reminiscent of a power spectrum. This 'power spectrum' provides information concerning the resonance of $|\Psi(t)\rangle$ with the frequency ω. For a given $g(t)$,

$$\tilde{f}(\omega) = \sum_n |c_n \, \tilde{g}(\omega - \omega_n)|^2 \,. \tag{4.6}$$

The Fourier transform of the window function, $\tilde{g}(\omega)$, is peaked at $\omega = 0$. $\tilde{f}(\omega)$, then, is peaked at frequencies that equal any ω_n, provided that $c_n \neq 0$. Eigenstates are found by finding $\tilde{f}(\omega)$ using Eq. 4.5, searching $\tilde{f}(\omega)$ for peaks, and taking the corresponding kets $|\tilde{\Psi}(\omega)\rangle$ to be the unnormalized eigenstates. Wave packets for which many c_n are nonzero lead to more eigenstates, as illustrated by Fig. 43.

To specialize the strategy to electronic structure problems, we simply restrict the choice of $|\Psi(0)\rangle$ to wave packets that are antisymmetric with respect to interchange of any two electrons. This is easily done with a Slater determinant, but the determinant need not be built from Fock orbitals.

We use a model Hamiltonian representing two spinless, charged fermions in a harmonic well. The repulsion between the two fermions is simplified to be

harmonic. Similar models have been used to explore alternative approaches to electronic structure [83]. The Hamiltonian is

$$H = \frac{1}{2}\{p_1^2 + p_2^2 + \Omega^2(q_1^2 + q_2^2) - \omega^2(q_1 - q_2)^2\}\,, \tag{4.7}$$

where q_i and p_i are the coordinate and momentum of fermion i, and the mass is taken to be the mass of an electron, set to 1. The Hamiltonian is separable, and may be written in the normal coordinates $q = \frac{1}{\sqrt{2}}(q_1 + q_2)$ and $\bar{q} = \frac{1}{\sqrt{2}}(q_1 - q_2)$ as

$$H = h + \bar{h} = \frac{1}{2}(p^2 + \bar{p}^2 + \Omega^2 q^2 + \xi^2 \bar{q}^2). \tag{4.8}$$

The normal mode frequency associated with $\bar{h}$ is $\xi = \sqrt{\Omega^2 - 2\omega^2}$. We set $\Omega = 2\pi$ fs^{-1} and $\omega = \pi$ fs^{-1}, leading to $\xi = \sqrt{2}\,\pi$ fs^{-1}; the eigenstates $|n, \bar{n}\rangle$ obey

$$\begin{aligned} h\,|n, \bar{n}\rangle &= \Omega(\frac{1}{2} + n)\,|n, \bar{n}\rangle \text{ and} \\ \bar{h}\,|n, \bar{n}\rangle &= \xi(\frac{1}{2} + \bar{n})\,|n, \bar{n}\rangle\,. \end{aligned} \tag{4.9}$$

To find the electronic eigenstates of this system using the described strategy, we will obtain the Fourier transform of the time evolution of the Slater determinant given by

$$\langle q_1, q_2|\Psi(0)\rangle = N(\langle q_1, q_2|\phi\rangle - \langle q_2, q_1|\phi\rangle)\,, \tag{4.10}$$

where $N = (2 - 2e^{-\frac{\xi}{2}(\delta q_{rms})^2})^{-\frac{1}{2}}$ normalizes $|\Psi(0)\rangle$ and

$$\langle q_1, q_2|\phi\rangle = \langle q_1, q_2|\, e^{-i\delta\, q_{rms} p_1}\, |0, 0\rangle\ ; \tag{4.11}$$

$q_{rms} \equiv \sqrt{\langle 0, 0|\, q_1^2\, |0, 0\rangle} = \sqrt{\langle 0, 0|\, q_2^2\, |0, 0\rangle}$ and $\delta \approx 3.59849$ ($\delta\, q_{rms} = \sqrt{10} \times 120$ pm). The potential energy surface and $\langle q_1, q_2|\Psi(0)\rangle$ are shown in Fig. 44.

The fidelity of a state $|\tilde{\Psi}(\omega)\rangle$ taken with respect to an eigenstate $|n, \bar{n}\rangle$ gives a measure of the accuracy of the spectral filtering strategy. The fidelity is given by

$$F(\omega, n, \bar{n}) \equiv \frac{|d_{n\bar{n}}(\omega)|^2}{\tilde{f}(\omega)}\,; \tag{4.12}$$

$d_{n\bar{n}}(\omega) \equiv \langle n, \bar{n}|\tilde{\Psi}(\omega)\rangle$. In the case of the model system characterized by the Hamiltonian in Eq. 4.7, both $\tilde{f}(\omega)$ and $F(\omega, n, \bar{n})$ have analytical expressions. Noting that $\tilde{f}(\omega) = \sum_{n\bar{n}} |d_{n,\bar{n}}(\omega)|^2$, we have

$$d_{n\bar{n}}(\omega) = c_{n\bar{n}}\tilde{g}(\omega - \omega_n - \omega_{\bar{n}})\,, \tag{4.13}$$

where

$$\tilde{g}(\omega) = \gamma T\{\mathrm{sinc}(\frac{\omega T}{\pi} + \frac{1}{2}) + \mathrm{sinc}(\frac{\omega T}{\pi} - \frac{1}{2})\}\,, \tag{4.14}$$

and

$$c_{n\bar{n}} \equiv \langle n, \bar{n}|\Psi(0)\rangle = Ne^{-\frac{(\delta\, q_{rms})^2}{8}(\Omega+\xi)}(\frac{\delta\, q_{rms}}{2})^{n+\bar{n}}\sqrt{\frac{\Omega^n\xi^{\bar{n}}}{n!\bar{n}!}}(1-(-1)^{\bar{n}})\,. \tag{4.15}$$

The sinc function in the expression for $\tilde{g}(\omega)$ is the normalized one: $\mathrm{sinc}(x) = \sin(\pi x)/\pi x$. Equation 4.15 is related to the familiar expression for a Glauber coherent state in the eigenbasis.

4.3 Direct Numerical Integration

We use a discrete position basis to determine $|\Psi(t_k)\rangle$ by direct numerical integration of the Schrödinger equation using the Riemann sum given by

$$\begin{aligned}\langle q_{1_i}, q_{2_j}|\Psi(t_k)\rangle &= \langle q_{1_i}, q_{2_j}|\, e^{-iHt_k}\,|\Psi(0)\rangle \\ &\cong \sum_{m=-N_q}^{N_q}\sum_{n=-N_q}^{N_q}\delta q^2\,\langle q_{1_i}, q_{2_j}|e^{-iHt_k}|q_{1_m}, q_{2_n}\rangle\langle q_{1_m}, q_{2_n}|\Psi(0)\rangle\end{aligned} \tag{4.16}$$

$\delta q = q_{1_i} - q_{1_{i-1}} = q_{2_j} - q_{2_{j-1}}$ and $\langle q_{1_i}, q_{2_j}|\Psi(t_k)\rangle$ has its conventional meaning. The summation limits are chosen so that $\langle q_{1_{\pm N_q}}, q_{2_{\pm N_q}}|\Psi(t_k)\rangle \cong 0$ for all t_k.

The approximate completeness relation

$$\sum_{m=-N_q}^{N_q}\sum_{n=-N_q}^{N_q}\delta q^2\,|q_{1_m}, q_{2_n}\rangle\langle q_{1_m}, q_{2_n}| = 1 \tag{4.17}$$

leads to expressions for the p_i^2 and q_i operators. The expressions are

$$\langle q_{1_i}, q_{2_j}|\, p_1^2\,|q_{1_m}, q_{2_n}\rangle \cong -\delta q^{-4}(\delta_{m,i+1} - 2\delta_{mi} + \delta_{m,i-1})\delta_{nj} \tag{4.18}$$

Table 1. Calculated energies of eigenstates in Figure 46 and the analytical energies.

State	Calculated Energy (eV)	Analytical Energy (eV)	Percent Error
$\|\tilde{\Psi}(\omega_{0,1})\rangle$	6.4522	6.4544	0.035
$\|\tilde{\Psi}(\omega_{1,1})\rangle$	10.5841	10.5900	0.056
$\|\tilde{\Psi}(\omega_{0,3})\rangle$	12.2961	12.3031	0.057
$\|\tilde{\Psi}(\omega_{2,1})\rangle$	14.7146	14.7257	0.075
$\|\tilde{\Psi}(\omega_{1,3})\rangle$	16.4244	16.4388	0.086

and

$$\langle q_{1_i}, q_{2_j}|\, q_1\, |q_{1_m}, q_{2_n}\rangle \cong \delta q^{-2} q_{1_i} \delta_{im} \delta_{jn}\,. \tag{4.19}$$

Analogous expressions hold for p_2^2 and q_2. These formulas in turn lead to an expression for the matrix elements of the model Hamiltonian in Eq. 4.7. That is,

$$\begin{aligned}\langle q_{1_i}, q_{2_j}|\, H\, |q_{1_m}, q_{2_n}\rangle \cong \frac{1}{2}\{&\delta q^{-2}[\,(q_{1_i}\Omega)^2 + (q_{2_j}\omega)^2]\,\delta_{im}\delta_{jn} - \\ &\delta q^{-4}[\,(\delta_{m,i+1} - 2\delta_{mi} + \delta_{m,i-1})\delta_{nj} + \\ &(\delta_{n,j+1} - 2\delta_{nj} + \delta_{n,j-1})\delta_{mi}]\,\}\,.\end{aligned} \tag{4.20}$$

We may therefore approximate $\langle q_{1_i}, q_{2_j}|\, e^{-iHt_k}\, |q_{1_m}, q_{2_n}\rangle$ and calculate the necessary $|\Psi(t_k)\rangle$s.

We set $T = 22\tau$ and $\delta t = 10^{-3}\tau$, where $\tau = 2\pi/\Omega$ is the period of the one-dimensional oscillator described by h (Eq. 4.8). The resulting 'power spectrum' is shown in Fig. 45.

Due to the antisymmetry of $|\Psi(0)\rangle$ with respect to reflection across q, $c_{n\bar{n}}$ is nonzero only for odd values of $\bar{n}$ (see Eq. 4.15), and the determined eigenstates have the antisymmetry necessary for electronic states. The five lowest-energy eigenstates are shown in Fig. 46. The energies of these states are displayed in Table 1 along with the analytical values.

To investigate the accuracy of the spectral filtering approach, the same five eigenstates were found for various different values of T to determine their fidelity (Eq. 4.12) as a function of T. The fidelities were numerically approximated by a Riemann sum using the analytical eigenstates and are plotted in Fig. 47. When $T \approx 0$, larger fidelity corresponds to larger $c_{n\bar{n}}$. This trend is seen in $\tilde{f}(\omega)$ as well. As T increases, each fidelity begins to increase, but at different rates. The rate of fidelity increase depends both on $c_{n\bar{n}}$ and on the proximity of state $|n, \bar{n}\rangle$ to other eigenkets. As seen in Fig. 45, states $|1, 1\rangle$ and $|2, 1\rangle$ make the largest contributions to $|\Psi(0)\rangle$. These two states are closest in energy to $|0, 3\rangle$ and $|1, 3\rangle$, respectively (Table 1). This proximity dampens the fidelity growth rate of $|\tilde{\Psi}(\omega_{0,3})\rangle$ and $|\tilde{\Psi}(\omega_{1,3})\rangle$; their fidelities require $2T \approx 3\tau$ before reaching at least 0.9. In contrast, the antisymmetric ground state, $|\tilde{\Psi}(\omega_{0,1})\rangle$ reaches a high fidelity after $2T \approx 1.5\tau$.

Through these fidelities, we have illustrated a key feature of this approach. *To obtain accurate eigenfunctions, $2T$ must be long compared to the inverse of the eigenfrequency spacing*, as expected from the time-energy uncertainty principle.

4.4 Semiclassical treatment

Due to its computational demands for memory, direct numerical integration of the Schrödinger equation would be a challenging route to finding the set of $|\tilde{\Psi}(\omega)\rangle$s, even for small systems. Parametrization of the initial wave packet may be helpful in reducing this demand. Instead of storing an amplitude for each basis ket as required by direct numerical integration, parametrization requires storing only a small number of parameters. One possible parametrization is a semiclassical approach, in which the time evolution of some of the parameters resemble classical trajectories.

We use a semiclassical approach derived from the Dirac-Frenkel-McLachlan functional [1, 2, 3], given by

$$F[\,|\dot{\Psi}\rangle] = (i\,\langle\dot{\Psi}| + \langle\Psi|\,H)(H\,|\Psi\rangle - i\,|\dot{\Psi}\rangle). \tag{4.21}$$

In this approach, which was pioneered by Heller [84, 85] in the calculation of nuclear dynamics underlying absorption spectra and adapted by Kovac and Cina [86] to a system-bath framework, we express $|\Psi(0)\rangle$ as a function of a set of real, time-dependent parameters $\lambda_i(t)$. Minimization of the DFM functional leads to parameter equations of motion specified by

$$\dot{\lambda} = \mathbf{M}^{-1} \cdot \chi, \tag{4.22}$$

where $\dot{\lambda}$ is a vector of parameter time derivatives, $M_{ij} = \mathrm{Re}\,\langle\frac{\partial\psi}{\partial\lambda_i}|\frac{\partial\psi}{\partial\lambda_j}\rangle$, and $\chi_i = \mathrm{Im}\,\langle\frac{\partial\psi}{\partial\lambda_i}|\,H\,|\psi\rangle$; $|\frac{\partial\psi}{\partial\lambda_i}\rangle$ satisfies $\langle\mathbf{q}|\frac{\partial\psi}{\partial\lambda_i}\rangle = \frac{\partial}{\partial\lambda_i}\langle\mathbf{q}|\psi\rangle$. The expressions for the elements of $\mathbf{M}$ and χ are given in Appendix C.

The initial state used is a sum of Gaussians (see equation 4.10), and may be parametrized using

$$\langle\mathbf{q}|\phi\rangle = Ze^{(\mathbf{q}-\mathbf{q_0})\cdot(i\mathbf{a'}-\mathbf{a''})\cdot(\mathbf{q}-\mathbf{q_0})+i\mathbf{p}\cdot(\mathbf{q}-\mathbf{q_0})+i\gamma}, \tag{4.23}$$

where $\mathbf{q}$, $\mathbf{q_0}$, $\mathbf{p}$ are n-dimensional vectors, $\mathbf{a'}$ and $\mathbf{a''}$ are $n \times n$ symmetric matrices, and γ and z are scalars. All components of the matrices and vectors are real, as are the scalars. The state is assumed to be expressible by Eq. 4.23 for all time, which is rigorously true for $|\Psi(0)\rangle$. Equations of motion are found for the parameters Z, $\mathbf{q_0}$, $\mathbf{a'}$, $\mathbf{a''}$, $\mathbf{p}$, and γ according to Eq. 4.22, and are integrated using a fourth-order Runge-Kutta algorithm [87]. As expected for this system, $\tilde{f}(\omega)$ and $F(\omega, n, \bar{n})$, calculated with $\delta t = 10^{-5}\tau$, are indiscernible from those calculated analytically. The energies of the first five eigenstates determined semiclassically are identical to those determined analytically in Table 1 to four decimal places.

4.5 Comparison to Hartree-Fock

To compare this approach to more traditional electronic structure calculations, we calculate the HF ground state using the steps outlined in Szabo and Ostlund [72]. The basis set used for the calculation is the same discrete-position basis used during direct numerical integration. The fidelity of the HF ground state with respect to the analytical ground state gives a measure of the accuracy of the calculation, and is found to be about 0.997. The energy of the HF ground state is found to be 6.4744 eV, which is within 0.31% of the analytical energy. Applying the spectral filtering method using the HF ground state as $|\Psi(0)\rangle$ reveals $|1,1\rangle$'s small contribution to the HF answer. The HF ground state and its spectrum are shown in Fig. 48.

For the model system, the HF approach works well, and more quickly than the spectral filtering approach explored here. However, the spectral filtering method retrieves a more accurate ground state with a fidelity of 0.999. As shown in Table 1, spectral filtering also determined a more accurate ground state energy, with an error of 0.035%.

4.6 Semiclassical treatment with a regularized Coulomb potential

Up to this point, as a proof of concept, we have made use of a simple model involving only harmonic potentials. While this model was useful in demonstrating how a spectral filtering technique could account for the antisymmetry required of electronic wave functions, electronic structure calculations are of course concerned with Coulombic interactions, not harmonic ones. In this section, we explore the possibility of a simple ansatz that could be used in the application of spectral filtering to systems with Coulombic potentials. As a first step, we consider the simplest case by limiting the system to only one dimension, which removes the

requirement of antisymmetry. We further simplify matters by considering a regularized Coulomb potential.

The Hamiltonian, in atomic units, is

$$H = \frac{p^2}{2} - \frac{1}{|q| + \epsilon}\,; \tag{4.24}$$

we set $\epsilon = 0.2a_0$, where a_0 is the Bohr radius. In anticipation of the kinds of integrals required to solve the parameter equations of motion derived from the Dirac-Frenkel-McLachlan variational principle, we fit the regularized Coulomb potential to a sum of three Gaussians,

$$-\frac{1}{|q| + \epsilon} \cong \sum_{i=1}^{3} C_i e^{-c_i q^2} \tag{4.25}$$

and substitute that potential into the Hamiltonian. The regularized Coulomb potential and its Gaussian fit are shown in Fig. 49.

We make use of an ansatz of the form

$$\psi(q) = \sum_{n=0}^{N} (A_n q^n) e^{\alpha q^2 + \beta q + i\gamma}\,, \tag{4.26}$$

where N is the order of the ansatz. Expressed in the real λ_i of Eq. 4.22, the parameters are

$$A_0 = \lambda_0\,, \tag{4.27}$$

$$A_{n\neq 0} = \lambda_{2n-1} + i\lambda_{2n}\,, \tag{4.28}$$

$$\gamma = \lambda_{2N+1}\,, \tag{4.29}$$

$$\beta = \lambda_{2N+2} + i\lambda_{2N+3}\,, \tag{4.30}$$

and

$$\alpha = \lambda_{2N+4} + i\lambda_{2N+5}\,. \tag{4.31}$$

The following results are obtained from the time evolution of a ninth-order ansatz, again using a fourth-order Runge-Kutta algorithm but now with a variable

time step. The initial values of the parameters are determined by fitting a fifth-order ansatz to the superposition

$$\langle q|\psi\rangle = \sqrt{0.9}\,\langle q|0\rangle + \sqrt{0.1}\,\langle q|1\rangle \ , \tag{4.32}$$

where $|0\rangle$ and $|1\rangle$ are the ground and first-excited states of the Hamiltonian, determined by diagonalization in a discrete position representation, respectively. Despite the accuracy of the initial fit, and in contrast to the ansatz used in Section 4.4, the state is found to not be expressible by a fifth-order ansatz for all time. To compensate, the order of the ansatz is increased to $N = 9$, setting parameters not involved in the fifth-order fit to initial values of 0. Figure 50 shows the difference in accuracy of the solutions to the equations of motion between the two wave packets, using position as a diagnostic, for $T = 10\bar{\tau}$ and $\delta t \leq 10^{-3}\bar{\tau}$, where $\bar{\tau}$ is the period of motion determined by the energetic difference between $|0\rangle$ and $|1\rangle$.

The parameters of the normalized ansatz at $t = 0$ are shown in Table 2, and as before, the expressions for the elements of $\mathbf{M}$ and χ for the ansatz defined in Eq. 4.26 are shown in Appendix D.

For these calculations, regularization of $\mathbf{M}$ is required for its inversion. Instead of inverting $\mathbf{M}$, we invert $\mathbf{M} + \bar{\epsilon}\exp\{-\frac{\mathbf{M}}{\bar{\epsilon}}\}$, in a manner similar to the regularization of a density matrix in multi-configuration time-dependent Hartree calculations [88]. Here, the regularization parameter $\bar{\epsilon}$, not to be confused with the ϵ of Eq. 4.24, is set to $10^{-8} \times \mathrm{Tr}\,\mathbf{M}$. To get a sense of the influence of this regularization, Figure 51 plots the trace of the regularization matrix, $\exp\{-\frac{\mathbf{M}}{\bar{\epsilon}}\}$, for the length of the calculation. This trace roughly corresponds to the number of eigenvalues of $\mathbf{M}$ influenced by the regularization; if an eigenvalue of $\mathbf{M}$ is positive and sufficiently smaller than $\bar{\epsilon}$, the corresponding eigenvalue of $\exp\{-\frac{\mathbf{M}}{\bar{\epsilon}}\}$

Table 2. Parameters of the initial, normalized ansatz.

Parameter	Value
A_0	$0.8371\, a_0^{-\frac{1}{2}}$
A_1	$-0.4670\, a_0^{-\frac{3}{2}}$
A_2	$-0.3507\, a_0^{-\frac{5}{2}}$
A_3	$0.1175\, a_0^{-\frac{7}{2}}$
A_4	$0.1067\, a_0^{-\frac{9}{2}}$
A_5	$-0.04185\, a_0^{-\frac{11}{2}}$
A_6	0
A_7	0
A_8	0
A_9	0
γ	0
β	$0.3074 a_0^{-1}$
α	$-0.4535 a_0^{-2}$

approaches unity.[1] Considering that, for a ninth-order ansatz, there are a total of 24 eigenvalues, few eigenvalues are influenced by the regularization matrix at any given time. The number of affected eigenvalues frequently reduces to zero throughout the calculation, though it begins steadily climbing as t nears T.

$\tilde{f}(\omega)$ is shown in Fig. 52, and the two recovered eigenstates are shown in Fig. 53. The resulting eigenenergies, in units of Hartree, are shown in Table 3, and are compared to the eigenenergies determined via diagonalization. Table 3 also

[1] $\mathbf{M}$ is not necessarily a positive definite or positive semi-definite matrix. With the regularization scheme used here, a negative eigenvalue could cause an unintentional regularization. One possible solution is to instead make use of the equation $\dot{\lambda} = (\mathbf{M}^T\mathbf{M})^{-1}\mathbf{M}^T \cdot \chi$, which follows directly from equation 4.22. The product $\mathbf{M}^T\mathbf{M} = \mathbf{M}^2$ is positive semi-definite, so it removes the issue of negative eigenvalues and may be regularized and inverted in place of $\mathbf{M}$. However, it has a larger condition number than $\mathbf{M}$, which, if too large, could be a problem for accuracy due to the calculation of a matrix exponential. In each calculation presented here, we encounter only one negative eigenvalue, which is much smaller in magnitude than $\bar{\epsilon}$. Therefore, $\mathbf{M}^2$ is never inverted in place of $\mathbf{M}$, and accurate eigenstates and eigenenergies are still obtained. The small magnitudes of the negative eigenvalues actually seen suggest the possibility that these eigenvalues are really zero, but appear negative due to round-off error. This possibility, however, remains to be demonstrated.

Table 3. Spectral filtration results for Coulomb potential

State	Eigenenergy via diagonalization (E_h)	Eigenenergy via spectral filtration (E_h)	Eigenstate fidelity
$\|\tilde{\Psi}(\omega_0)\rangle$	-1.687	-1.670	0.999
$\|\tilde{\Psi}(\omega_1)\rangle$	-0.317	-0.298	0.973

shows the fidelities of the eigenstates determined by spectral filtration, calculated with respect to the same eigenstates determined by diagonalization. In obtaining these results, the window function defined above Eq. 4.4 is again used during the Fourier transform. We note that the resulting fidelities might seem to suggest the presence of the same ground state bias that we wish to remove. However, this bias is a consequence of the chosen initial wave packet, not a feature of the method itself.

The fact that a low-order ansatz is capable of obtaining these results is promising. In a multi-dimensional problem, the overall order may not need to increase to handle the extra dimensions, providing good scaling with dimensions; in particular, less than the exponential scaling of direct numeric integration.

4.7 Concluding discussion

Expressing the time evolution emanating from an initial, non-stationary Slater determinant as a Fourier series yields properly antisymmetrized eigenstates and their associated energies. The fidelity of the numerically determined states tends to unity with increasing T, though short propagations can give a reasonably high fidelity in some instances. This approach successfully recovers antisymmetric solutions to the time-independent Schrödinger equation for our simple, two-particle Hamiltonian.

The scaling of this approach with system size in the straightforward implementation using direct numerical integration is exponential. The $|\Psi(t_k)\rangle$s

are found by repeated multiplication of a matrix and a vector, which scales as $O(n^2)$, where n is the size of the vector. The size of the vector, in turn, is the size of the basis set used. For a position grid of b position kets, $n = b^N$, where N is the number of degrees of freedom. Therefore, this approach has exponential scaling in N, $O(b^{2N})$. This scaling is quite a bit worse than the scaling of methods like DFT and QMC, which scale by a power law in N [77].

Exponential scaling may not be as bad as it seems at first glance, however. We have not attempted any optimizations in the choice of basis. For example, the position grids used are evenly spaced and are not truncated based on total potential energy. Improvement in the efficiency of the spatial grid can be straightforwardly made, particularly in areas of the grid where the potential is high. In these areas, the de Broglie wavelength is large, and a wider grid spacing may recover the same salient information as a finer spacing. Steps towards optimization can be accomplished using a discrete variable representation [89]. These representations can be made manually if one knows where the grid spacing need not be fine. A more systematic approach to obtaining a discrete variable representation involves selecting a set of basis functions, perhaps harmonic oscillator eigenstates, and diagonalizing the position operator in that basis. The eigenkets of the position operator form the new discrete position basis.

A semiclassical method, or another approach based on a parametrized trial wave function, also holds promise. The memory requirements for the method described in Section 4.4 are much smaller than those of the direct numerical integration approach. The $\mathbf{a}$ matrix, the parameter requiring the most memory, scales as a power law in the number of particles. For N particles, $\mathbf{a}$ contains $(dN)^2$ entries, where d is the number of dimensions. As shown in Section 4.6,

parametrized wave packets are also capable of handling the simplest Coulombic potentials, though a more complex parametrization than Gaussian is necessary. The parametrization used here is reminiscent of Hagedorn wave packets [90], which also consist of polynomials multiplied by Gaussians. Spectral filtration of a more realistic Coulomb interaction remains to be demonstrated.

An issue remains in that semiclassical approaches tend to deviate from the true answer at longer times. Since the accuracy of eigenstates determined via the Fourier transformation increases with evolution time, finding an appropriate evolution time for a semiclassical approach may prove to be a central challenge to the spectral filtration methodology. Chapman, Cheng, and Cina used a related semiclassical approach to replace exponential scaling with power-law scaling when propagating Gaussian wave packets for bath states attached to fixed quantum-mechanical subsystem states [91]. The fidelities of the wave packets remained high after several periods, and the parameters determined by the approximation agreed with the exact solution for long times as well. While carrying out the calculations in Section 4.6 however, we encountered this problem. Even the ninth-order ansatz begins to fail beyond $T = 10\bar{\tau}$. Finding an appropriate evolution time will likely prove challenging in applying spectral filtering to a system where comparison to an accurate diagnostic is not available, as it was to us through the use of a discrete position basis. Perhaps parametrizations that do not include Gaussians will prove to be better suited for Coulombic potentials.

Another issue with spectral filtering is the possible occurrence of degeneracies and close-spaced eigenenergies. According to the time-energy uncertainty principle, greater propagation times are needed to resolve closely spaced levels. In their development of the filter-diagonalization method, Neuhauser

and Wall [92, 93] make note of this issue, and this is where the diagonalization piece of the filter-diagonalization method comes into play [92]. Instead of taking $|\tilde{\Psi}(\omega)\rangle$ to be the eigenstates, a set of $|\tilde{\Psi}(\omega)\rangle$s is found in a given energy range and used to form a matrix that can be diagonalized. Wang, Carrington, and Corey further investigated the influence of the time-energy uncertainty principle on the accuracy of filter diagonalization [94].

Determining eigenstates through the time evolution of wave packets offers some benefits. First, as mentioned in the introduction, this method completely removes the ground-state bias that HF-based methods experience. Second, correlation is accounted for automatically; there is no need to begin by representing an electron's interactions with other electrons as an interaction with an averaged field. Third, a single calculation is capable of revealing many eigenstates, depending on the choice of initial wave packet. Fourth, eigenenergy accuracy is controlled through propagation time. Finally, if a parametrized wave function is used, the memory scaling of the parameters could make spectral filtering an interesting avenue of exploration for larger systems [86].

The spectral filtering approach presented in Section 4.4 is thematically related to work by Meyer and Beck, who combined filter-diagonalization with a multi-configuration time-dependent Hartree methodology to obtain rovibrational spectra [95]. Our approach is also related to a combination of filter-diagonalization and time-dependent Hartree-Fock [96], where a Slater determinant is propagated in time with a time-dependent Hamiltonian. Differences to the present case include the application to the stationary states of a time-independent Hamiltonian as opposed to dynamics, as well as the lack of HF orbitals. The analogy to TDHF provides another avenue for improvement: an improved spectral filtering approach

could take advantage of TDHF or improved versions, such as multi-configuration time-dependent Hartree-Fock [97, 98]. Many other real-time methods exist for propagating electronic wave functions [99], which could provide increases in efficiency. However, electron correlation may need to be accounted for in an approximate way, sacrificing one of the advantages of the formulation presented here.

There seems to be merit in approaching the problem of electronic structure determination through time evolution of wave packets. Future work will focus on generating more efficient spatial grids and developing parametrized trial wave functions to lower the formidable scaling barrier and better handle Coulombic pair potentials.

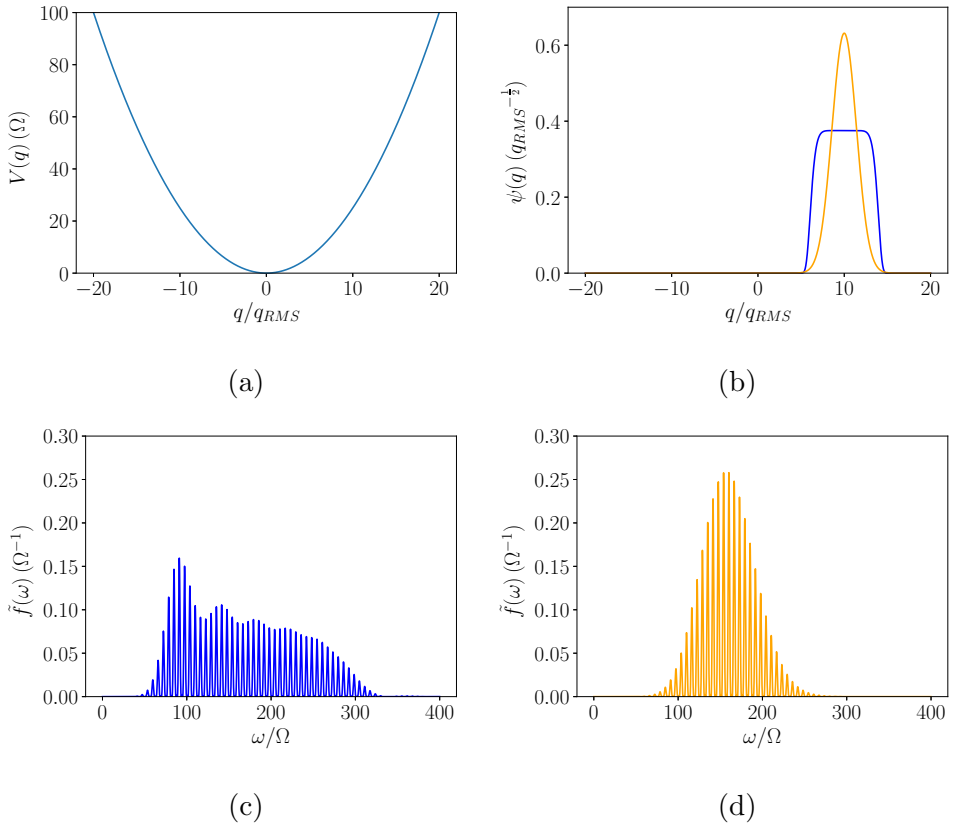

Figure 43. Demonstration of the effect of wave packet choice on $\tilde{f}(\omega)$, using a simple harmonic oscillator. The potential (a) is $V = \frac{1}{2}\Omega^2 q^2$ with $\Omega = 2\pi$ fs^{-1} and $m = 1$, and the initial wave packets are shown in (b). The initial wave packets have the form $\psi(q; n, \sigma) = N_{n,\sigma}\exp\{-(\frac{q-\delta q}{2\sigma\, q_{rms}})^{2n}\}$; $n = \sigma = 1$ for the orange wave packet, forming a Glauber coherent state, and $n = 5$ and $\sigma = 2$ for the blue wave packet, forming a squarish wave packet. We take the displacement to be $\delta q = 10 q_{rms}$. $N_{n,\sigma}$ is the normalization constant for the state parameterized by n and σ. The power spectrum (equation 4.5) of the blue wave packet's evolution in (c) shows resonance with more states than the spectrum of the orange wave packet's evolution in (d), as the square packet is a superposition of more eigenfunctions. The power spectra shown in (c) and (d) were calculated using $T = 1$ fs.

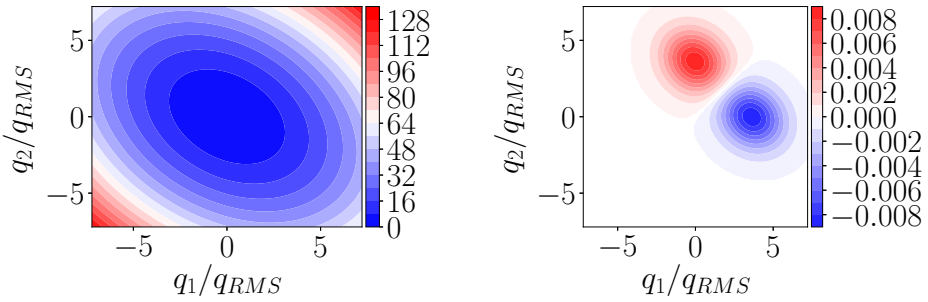

(a) (b)

Figure 44. Contour plot of the potential surface associated the model Hamiltonian (a). The contours show potential energy in eV. A contour plot of the initial Slater determinant (equation 4.10) is shown in (b). The contours show $\langle q_1, q_2 | \Psi(0) \rangle$ in units of pm^{-1}.

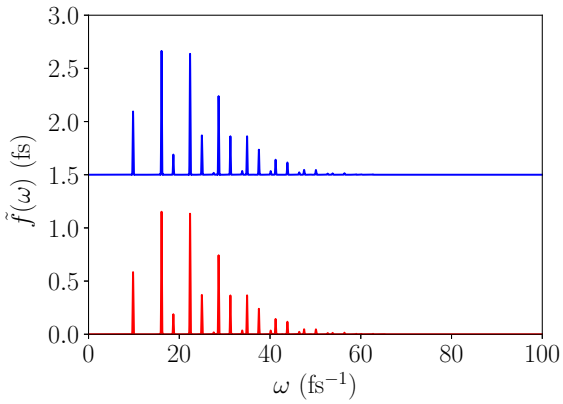

Figure 45. The 'power spectrum' determined for $T = 22\tau$, found both by direct numerical integration using a spatial grid (red) and analytically (blue, offset by 1.5 fs).

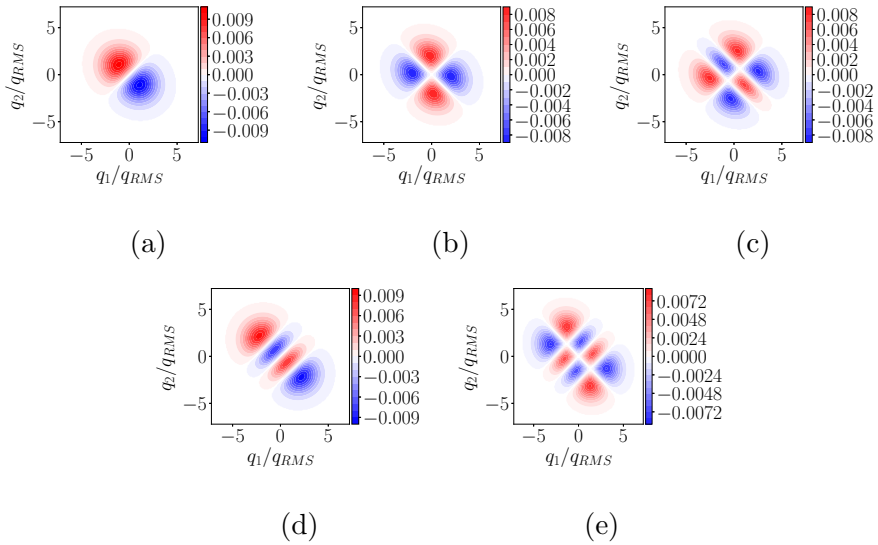

Figure 46. Contour plots of the normalized eigenstates determined using $T = 22\tau$ and $\delta t = 10^{-3}\tau$. The contours are in units of pm^{-1}. The states are $|\tilde{\Psi}(\omega_{0,1})\rangle$ (a), $|\tilde{\Psi}(\omega_{1,1})\rangle$ (b), $|\tilde{\Psi}(\omega_{2,1})\rangle$ (c), $|\tilde{\Psi}(\omega_{0,3})\rangle$ (d), and $|\tilde{\Psi}(\omega_{1,3})\rangle$ (e). Note the antisymmetry of each state with respect to reflection through the line $q_1 = q_2$.

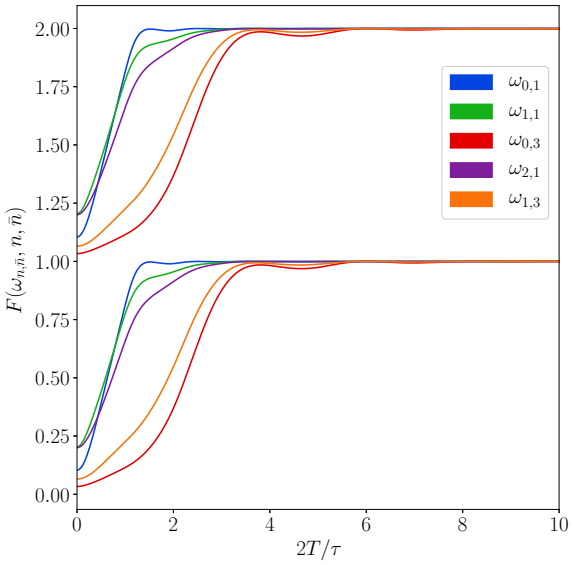

Figure 47. Fidelities of the five eigenstates shown in Figure 46, as determined by both direct numerical integration and analytically (offset by 1). Lines are included as guides to the eye.

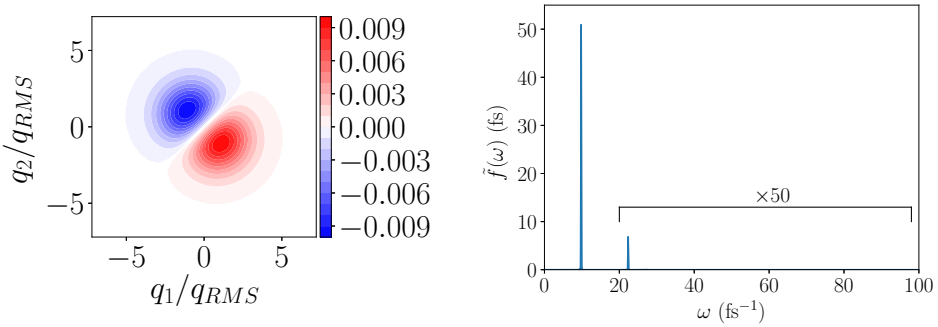

(a) (b)

Figure 48. The approximate ground state of the system as calculated by SCF-HF (a) (contours in units of pm^{-1}) and the 'power spectrum' of this state's time evolution (b), for which values of $\tilde{f}(\omega)$ have been scaled by a factor of 50 for $\omega > 20$ fs^{-1}. The power spectrum is strongly peaked at the frequency of the true ground state, reflecting the high fidelity of the HF ground state with the true ground state of the system. The spectrum is also peaked at the frequency of the third excited state.

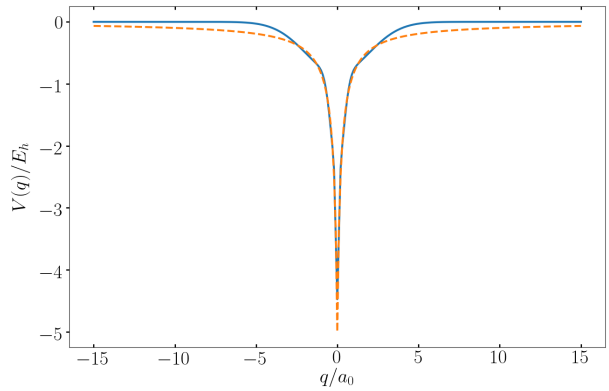

Figure 49. Gaussian-sum fit (blue) to the regularized Coulomb potential (dotted orange). Though the fit does not capture the gradual upward slope beginning around $\pm 2.5 a_0$, the steeper well is well described. The potentials are shown in energies of Hartree (E_h), with position in units of Bohr radii (a_0).

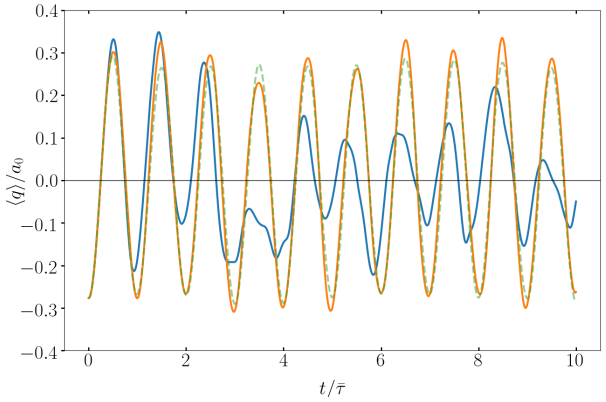

Figure 50. The expectation value of q as a function of evolution time for the fitted fifth-order ansatz (blue) and the same wave packet evolving under a ninth-order ansatz (orange) as described in the text. The dotted, green line shows $\langle q \rangle$ for the same wave packet but calculated using basis-set methods. The fifth-order ansatz is not capable of accurately solving the equations of motion, though increasing the order greatly increases the accuracy.

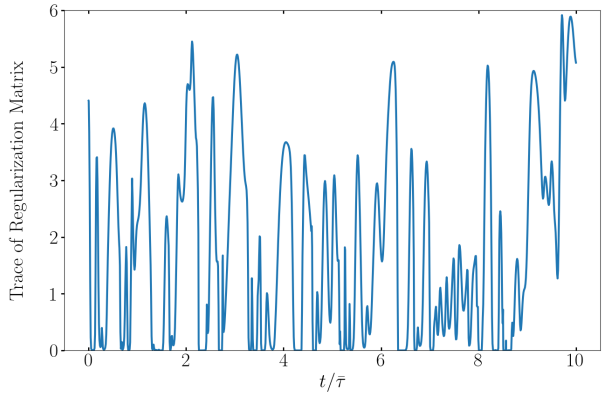

Figure 51. The trace of the regularization matrix, given by $e^{-\mathbf{M}/\bar{\epsilon}}$, at different points in the ansatz's time evolution.

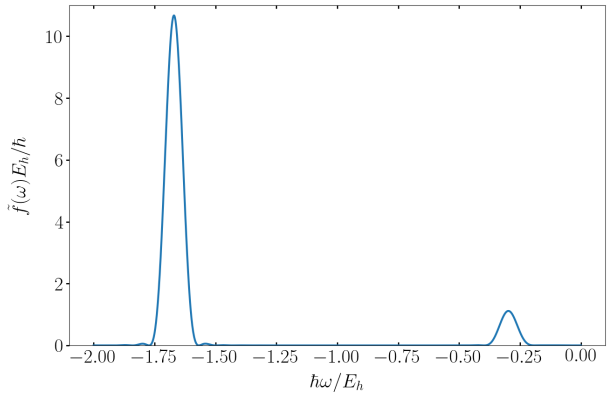

Figure 52. 'Power spectrum' resulting from the Fourier transform of the time evolution of the ansatz defined by the parameters listed in Table 2. The spectrum consists of two peaks, corresponding to the ground and first-excited states of the system. The lower-energy peak is the higher of the two, consistent with the ansatz's larger ground-state amplitude (see equation 4.32).

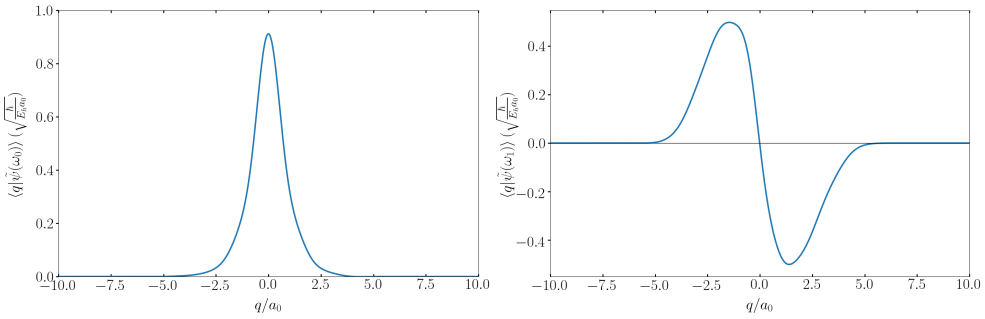

(a) (b)

Figure 53. The ground (a) and first-excited (b) states corresponding to the peaks in $\tilde{f}(\omega)$ in Figure 52. Though the fidelity of the state shown in (b) is high at 0.973, the state is visibly not quite antisymmetric. More accurate propagation of the equations of motion for longer times (larger T) may resolve this issue.

CHAPTER V

DISCUSSION

We have presented a dynamical approach to the calculation of two-dimensional electronic spectroscopy signals, observed the appearance of electronic energy transfer on said signals, seen where electronic coherence between singly-excited states appears in a WPI experiment, and presented a dynamical approach to electronic structure calculations. These works all make use of dynamics to develop theories and carry out calculations, whether they be for spectroscopic signals or for stationary electronic states.

Chapter II of this dissertation presents an exercise in reframing the basic theory of two-dimensional electronic spectroscopy with a focus on the wave packets set in motion by femtosecond laser pulses. The resulting signal expressions contain multi-pulse wave-packet overlaps, which are determined by a series of pulse propagators that describe the effects of the pulses on the wave packets. The wave packets also undergo intermittent periods of free evolution on various potential energy surfaces. Time-delay regions for which the various possible overlaps may make a contribution to the signal are determined, and the knowledge of these regions, along with pulse polarizations of yxxx and a spatially oriented model, is used to set up experimental conditions that dramatically reduce the number of contributing overlaps. This chapter introduces a model energy transfer dimer and presents calculations that help us understand the appearance of energy transfer in two-dimensional wave-packet interferometry signals. These signals are interpreted in terms of the underlying wave-packet dynamics using a semiclassical approach, considering phase-space diagrams to obtain time-delay conditions for large overlap between wave packets.

Chapter III takes the spatially oriented model dimer from the previous chapter and uses it to present a WPI experiment that can directly observe electronic coherence between site states and excitonic states in the singly-excited manifold. This experiment makes use of a different polarization scheme than that in Chapter II, namely xxxy instead of yxxx, which, combined with the fixed spatial orientation of the dimer model, allows for the probing of individual monomers. The nature of electronic coherence as overlaps between wave packets is shown, and the proposed experiment works by overlapping a wave packet that has moved to an "acceptor" state via energy transfer with a copy of the wave packet remaining on the "donor" state. This obtains the desired overlap. The decrease of the accuracy of the method with increasing pulse duration is shown. The influences both of multiple nuclear modes and of differing site-energy offsets on the time-development of the coherence are explored for both weak coupling (intersite coherence) and strong coupling (interexciton coherence).

A natural direction to take these works is increasing the complexity of the model, possibly by adding more monomers. A triangular trimer or square tetramer, for example, could be particularly interesting in that the symmetries of the systems could promote degeneracies in electronic states, which in turn allow for the observation of a geometric phase, also called a Berry phase, by inducing a pseudorotation [100]. Additionally, such systems could allow for the observation of which-path interference akin to double-slit experiments. In an energy transfer tetramer, for example, an electronic excitation generated at one monomer may take two paths to arrive at the monomer on the opposite corner. Vibrations in the multimer could change the length of the two paths, changing the interference.

Observing either which-path interference or geometric phases in two-dimensional electronic spectroscopy signals would be very exciting!

Chapter IV presents a spectral filtering approach to the calculation of electronic structure. This work adapts an idea presented by Heller in the context of nuclear dynamics to electronic states, which obey antisymmetry conditions. At the heart of the theory is the Fourier transformation of the time evolution of an arbitrary, antisymmetrized wave packet. Two different methods of time evolution are presented. The first is direct numeric integration using a discrete position basis. While obtaining good results, this approach is prohibitively expensive for many degrees of freedom. The second is a semiclassical parametrization, which performs just as well as the direct numerical integration in the model two-particle Hamiltonian studied there, but with the added benefit of power law scaling. The spectral filtering method allows for the recovery of many states at once, removes the ground-state bias of Hartree-Fock-based methods, accounts for electron correlation automatically, and allows for accuracy control via propagation time.

Both of these methods are applied to a two-particle model Hamiltonian that consists of harmonic potentials and harmonic interactions. To test the method on the Coulombic interactions of molecular Hamiltonians, parametrization of a slightly more complex ansatz, consisting of a product of a gaussian and a polynomial, is applied to the simplest Coulombic case. The ansatz is capable of accurate time evolution for long enough to obtain high fidelities at a low order, but accuracy suffers as the length of time evolution is increased. However, like the semiclasscal parametrization applied to harmonic potentials, this ansatz may not scale exponentially with the number of degrees of freedom, leaving open the possibility of its application to real molecules. Future work should focus on

improvement of parametrization for Coulombic potentials and application to atoms and molecules.

APPENDIX A

RELATIONSHIP BETWEEN POLARIZED PUMP-PROBE AND WPI SIGNALS

We have sought to isolate the electronic coherence within the singly excited manifold from the two-dimensional electronic spectroscopy signal of an energy-transfer dimer with non-parallel site transition moments. Eq. (3.30) for the 2D signal of a weakly coupled dimer with simultaneous A and B pulses, as well as simultaneous C and D pulses, provides the intersite electronic coherence as a function of t_{CB}. The equivalent formula of Eq. (3.29) is seen not to involve any nesting of the A and B or C and D reduced pulse propagators. These features suggest a direct examination of the fluorescence-detected pump-probe signal with an x-polarized pump pulse and a probe pulse with variously phased, equal-amplitude components of the electric field along the x and y axes.

A pump-probe signal of this kind is bi-quadratic in the incident fields

$$\mathbf{E}_u(t) = E_u f(t - t_u)\hat{\mathbf{x}} \cos[\Omega(t - t_u) + \varphi_u] \,, \tag{A.1}$$

and

$$\mathbf{E}_r(t) = E_r f(t - t_r)\frac{1}{\sqrt{2}}\big\{\hat{\mathbf{x}} \cos[\Omega(t - t_r) + \varphi_r] + \hat{\mathbf{y}} \cos[\Omega(t - t_r) + \varphi_r + \chi]\big\} \,, \tag{A.2}$$

of the pump and probe pulses, respectively. We shall assume that $t_r - t_u$ comfortably exceeds the pulse duration. If the laser pulses are assumed to travel in the positive z-direction, then the choices of 0 and π for χ correspond to probe polarization at plus and minus 45° with respect to the x-polarization of the pump pulse, respectively, while $\chi = \pi/2$ and $\chi = -\pi/2$ correspond to a left and right circularly polarized probe, respectively.

Under fluorescence detection, one need only consider first- through third-order contributions to the singly- and doubly-excited amplitudes. The relevant

portion of the time-dependent molecular state can then be written

$$|\Psi\rangle = |\uparrow_u\rangle + |\uparrow_r\rangle + \underline{|\uparrow_u\uparrow_u\rangle} + |\uparrow_u\uparrow_r\rangle + \underline{|\uparrow_r\uparrow_r\rangle} + |\uparrow_u\downarrow_u\uparrow_r\rangle + |\uparrow_u\downarrow_r\uparrow_r\rangle + \underline{|\uparrow_u\uparrow_u\downarrow_r\rangle} + |\uparrow_u\uparrow_r\downarrow_r\rangle\,. \tag{A.3}$$

The underlined amplitudes would make optically phase-unstable contributions to the bi-quadratic signal and will subsequently be ignored. The pump-probe signal is $S = Q_{\rm one}P_{\rm one} + Q_{\rm two}P_{\rm two}$, where the singly- and doubly-excited populations are

$$P_{\rm one} = 2{\rm Re}\big\{\langle\uparrow_u \mid \uparrow_u\downarrow_r\uparrow_r\rangle + \langle\uparrow_u \mid \uparrow_u\uparrow_r\downarrow_r\rangle + \langle\uparrow_u\downarrow_u\uparrow_r \mid \uparrow_r\rangle\big\}\,, \tag{A.4}$$

and

$$P_{\rm two} = \langle\uparrow_u\uparrow_r \mid \uparrow_u\uparrow_r\rangle\,, \tag{A.5}$$

respectively (compare Eq. (3.20)).

We explicitly identify the contributions of the x- and y-components of the probe pulse to each of the overlaps in Eqs. (A.4) and (A.5) and make use of a rotating-wave approximation in the probe-pulse propagators to obtain

$$\langle\uparrow_u \mid \uparrow_u\downarrow_r\uparrow_r\rangle \cong \tfrac{1}{2}\big[\langle\uparrow_u \mid \uparrow_u\downarrow_x\uparrow_x\rangle^{(0)} + \langle\uparrow_u \mid \uparrow_u\downarrow_x\uparrow_y\rangle^{(1)}e^{-i\chi} + \langle\uparrow_u \mid \uparrow_u\downarrow_y\uparrow_x\rangle^{(1)}e^{i\chi} + \langle\uparrow_u \mid \uparrow_u\downarrow_y\uparrow_y\rangle^{(2)}\big]\,, \tag{A.6}$$

$$\langle\uparrow_u \mid \uparrow_u\uparrow_r\downarrow_r\rangle \cong \tfrac{1}{2}\big[\langle\uparrow_u \mid \uparrow_u\uparrow_x\downarrow_x\rangle^{(2)} + \langle\uparrow_u \mid \uparrow_u\uparrow_x\downarrow_y\rangle^{(1)}e^{i\chi} + \langle\uparrow_u \mid \uparrow_u\uparrow_y\downarrow_x\rangle^{(1)}e^{-i\chi} + \langle\uparrow_u \mid \uparrow_u\uparrow_y\downarrow_y\rangle^{(0)}\big]\,, \tag{A.7}$$

$$\langle\uparrow_u\downarrow_u\uparrow_r \mid \uparrow_r\rangle \cong \tfrac{1}{2}\big[\langle\uparrow_u\downarrow_u\uparrow_x \mid \uparrow_x\rangle^{(0)} + \langle\uparrow_u\downarrow_u\uparrow_x \mid \uparrow_y\rangle^{(1)}e^{-i\chi} + \langle\uparrow_u\downarrow_u\uparrow_y \mid \uparrow_x\rangle^{(1)}e^{i\chi} + \langle\uparrow_u\downarrow_u\uparrow_y \mid \uparrow_y\rangle^{(0)}\big]\,, \tag{A.8}$$

and

$$\langle\uparrow_u\uparrow_r \mid \uparrow_u\uparrow_r\rangle \cong \tfrac{1}{2}\big[\langle\uparrow_u\uparrow_x \mid \uparrow_u\uparrow_x\rangle^{(2)} + \langle\uparrow_u\uparrow_x \mid \uparrow_u\uparrow_y\rangle^{(1)}e^{-i\chi} + \langle\uparrow_u\uparrow_y \mid \uparrow_u\uparrow_x\rangle^{(1)}e^{i\chi} + \langle\uparrow_u\uparrow_y \mid \uparrow_u\uparrow_y\rangle^{(0)}\big]\,. \tag{A.9}$$

The individual overlaps have been labeled according to the lowest order in J at which they do not vanish. In the weak EET-coupling regime considered here, we shall retain signal contributions only through first order in J.

Inserting Eqs. (A.6) - (A.9) in the signal expression gives

$$\begin{aligned} S(\chi) = Q_{\text{one}}\text{Re}\big\{ & \langle \uparrow_u \mid \uparrow_u\downarrow_x\uparrow_x\rangle^{(0)} + \langle \uparrow_u \mid \uparrow_u\uparrow_y\downarrow_y\rangle^{(0)} + \langle \uparrow_u\downarrow_u\uparrow_x \mid \uparrow_x\rangle^{(0)} + \langle \uparrow_u\downarrow_u\uparrow_y \mid \uparrow_y\rangle^{(0)} \\ & + e^{-i\chi}\big[\langle \uparrow_u \mid \uparrow_u\downarrow_x\uparrow_y\rangle^{(1)} + \langle \uparrow_u\downarrow_y\uparrow_x \mid \uparrow_u\rangle^{(1)} + \langle \uparrow_u \mid \uparrow_u\uparrow_y\downarrow_x\rangle^{(1)} \\ & + \langle \uparrow_u\uparrow_x\downarrow_y \mid \uparrow_u\rangle^{(1)} + \langle \uparrow_u\downarrow_u\uparrow_x \mid \uparrow_y\rangle^{(1)} + \langle \uparrow_x \mid \uparrow_u\downarrow_u\uparrow_y\rangle^{(1)}\big]\big\} \\ & + \frac{Q_{\text{two}}}{2}\langle \uparrow_u\uparrow_y \mid \uparrow_u\uparrow_y\rangle^{(0)} + Q_{\text{two}}\text{Re}\big\{e^{-i\chi}\langle \uparrow_u\uparrow_x \mid \uparrow_u\uparrow_y\rangle^{(1)}\big\}\,. \end{aligned} \tag{A.10}$$

The difference between signals with plus- and minus-45$^{\text{o}}$ linearly polarized probe pulses is

$$\begin{aligned} S(0)-S(\pi) = 2Q_{\text{one}}\text{Re}\big\{ & \langle \uparrow_u \mid \uparrow_u\downarrow_x\uparrow_y\rangle^{(1)} + \langle \uparrow_u\downarrow_y\uparrow_x \mid \uparrow_u\rangle^{(1)} + \langle \uparrow_u \mid \uparrow_u\uparrow_y\downarrow_x\rangle^{(1)} + \langle \uparrow_u\uparrow_x\downarrow_y \mid \uparrow_u\rangle^{(1)} \\ & + \langle \uparrow_u\downarrow_u\uparrow_x \mid \uparrow_y\rangle^{(1)} + \langle \uparrow_x \mid \uparrow_u\downarrow_u\uparrow_y\rangle^{(1)}\big\} + 2Q_{\text{two}}\text{Re}\big\{\langle \uparrow_u\uparrow_x \mid \uparrow_u\uparrow_y\rangle^{(1)}\big\}\,; \end{aligned} \tag{A.11}$$

the difference $S(\pi/2) - S(-\pi/2)$ between signals with left and right circularly-polarized probes is just the same, but with Re replaced by Im. Hence we see that the pump-probe difference signals $S(0) - S(\pi)$ and $S(\pi/2) - S(-\pi/2)$ from the weakly coupled dimer provide the same information on the dynamics of the intersite electronic coherence as the 2D-WPI signal (3.20) with $-\varphi_{BA} + \varphi_{DC} = 0$ and $-\pi/2$, respectively.

APPENDIX B

PERTURBATION THEORY FOR THE STRONG EET-COUPLING CASE

Here we detail our treatment of the WPI-signal expression (3.33) for the dimer with large J by means of time-dependent perturbation theory through first order in the interexciton coupling. It is useful to define center-of-mass and relative vibrational coordinates and momenta whose components combine the corresponding internal coordinates and momenta of the two monomers:

$$\mathbf{Q} = \frac{\mathbf{q}_b + \mathbf{q}_a}{\sqrt{2}}\,,\ \mathbf{q} = \frac{\mathbf{q}_b - \mathbf{q}_a}{\sqrt{2}}\,; \tag{B.1}$$

and

$$\mathbf{P} = \frac{\mathbf{p}_b + \mathbf{p}_a}{\sqrt{2}}\,,\ \mathbf{p} = \frac{\mathbf{p}_b - \mathbf{p}_a}{\sqrt{2}}\,. \tag{B.2}$$

Using these operators, we can write $H = H^{(0)} + H^{(1)}$, where $H^{(0)} = T + H_{\rm el}^{(0)}(\mathbf{Q},\mathbf{q})$ with $T = \sum_{i=1}^{N} \frac{1}{2}(P_i^2 + p_i^2)$. Referring to Eq. (3.10) gives

$$\begin{aligned} H_{\rm el}^{(0)}(\mathbf{Q},\mathbf{q}) = {} & |0\rangle V_{gg}(\mathbf{Q},\mathbf{q})\langle 0| + |\bar{1}\rangle\big[L(\mathbf{Q},\mathbf{q}) + M + \frac{K}{M}(K(\mathbf{q}) - K)\big]\langle\bar{1}| \\ & + |1\rangle\big[L(\mathbf{Q},\mathbf{q}) - M - \frac{K}{M}(K(\mathbf{q}) - K)\big]\langle 1| + |2\rangle V_{ee}(\mathbf{Q},\mathbf{q})\langle 2|\,, \end{aligned} \tag{B.3}$$

and

$$H^{(1)} = -\frac{J}{M}(K(\mathbf{q}) - K)\big(|\bar{1}\rangle\langle 1| + |1\rangle\langle\bar{1}|\big)\,. \tag{B.4}$$

Equations (B.3) and (B.4) feature

$$K(\mathbf{q}) = \frac{\Delta\epsilon}{2} + \sum_i \frac{\omega_i^2 d_i}{\sqrt{2}} q_i\,, \tag{B.5}$$

for the model dimer, with $\Delta\epsilon = \epsilon_{eg} - \epsilon_{ge}$;

$$L(\mathbf{Q},\mathbf{q}) = \bar{\epsilon} + \sum_i \frac{\omega_i^2}{2}\Big[\Big(Q_i - \frac{d_i}{\sqrt{2}}\Big)^2 + q_i^2 + \frac{d_i^2}{2}\Big]\,, \tag{B.6}$$

with $\bar{\epsilon} = (\epsilon_{eg} + \epsilon_{ge})/2$; and

$$M(\mathbf{q}) = \sqrt{J^2 + K^2(\mathbf{q})}\,. \tag{B.7}$$

We adopt the conventions $K = K(\mathbf{0})$, $L = L(\mathbf{0},\mathbf{0})$, and $M = M(\mathbf{0})$.

Because more explicit evaluations yield

$$L(\mathbf{Q},\mathbf{q}) \pm M \pm \frac{K}{M}(K(\mathbf{q}) - K) \tag{B.8}$$
$$= \bar{\epsilon} \pm M + \sum_i \frac{\omega_i^2}{2}\left[\left(Q_i - \frac{d_i}{\sqrt{2}}\right)^2 + \left(q_i \pm \frac{K}{M}\frac{d_i}{\sqrt{2}}\right)^2 + \frac{J^2}{M^2}\frac{d_i^2}{2}\right],$$

and

$$-\frac{J}{M}(K(\mathbf{q}) - K) = -\frac{J}{M}\sum_i \frac{\omega_i^2 d_i}{\sqrt{2}} q_i\,, \tag{B.9}$$

as these quantities appear in Eqs. (B.3) and (B.4), respectively, we see that the nuclear dynamics is separable between center-of-mass and relative degrees of freedom. The center-of-mass dynamics is the same in the $\bar{1}$- and 1-states, and the interexciton coupling coefficient (B.9) depends only on the relative nuclear coordinates. These features significantly simplify the calculation of the interexciton-coherence signals.

A perturbative formula for the WPI-observed interexciton coherence can now be obtained from Eq. (3.39) in the form

$$\frac{\langle\uparrow_A(t)|\bar{1}\rangle\, p^{(\bar{1}0)}p^{(01)}\,\langle 1|\uparrow_A(t)\rangle}{|p^{(\bar{1}0)}_{\sigma=0}\, p^{(01)}_{\sigma=0}|\,\langle\uparrow_A(t)|\uparrow_A(t)\rangle} = \frac{\langle\phi_0|p^{(0\bar{1})}[-t]^{(0)}_{\bar{1}\bar{1}}p^{(\bar{1}0)}p^{(01)}[t]^{(1)}_{1\bar{1}}p^{(\bar{1}0)}|\phi_0\rangle}{|p^{(\bar{1}0)}_{\sigma=0}\, p^{(01)}_{\sigma=0}|\,\langle\phi_0|p^{(0\bar{1})}p^{(\bar{1}0)}|\phi_0\rangle}\,. \tag{B.10}$$

The actual interexciton coherence is given perturbatively by

$$\frac{\langle\uparrow_A\,(t)|\bar{1}\rangle\langle 1|\uparrow_A(t)\rangle}{\langle\uparrow_A\,(t)|\uparrow_A(t)\rangle} = \frac{\langle\phi_0|p^{(0\bar{1})}[-t]^{(0)}_{\bar{1}\bar{1}}[t]^{(1)}_{1\bar{1}}p^{(\bar{1}0)}|\phi_0\rangle}{\langle\phi_0|p^{(0\bar{1})}p^{(\bar{1}0)}|\phi_0\rangle}\,, \tag{B.11}$$

and the maximum coherence becomes

$$\sqrt{\frac{\langle\uparrow_A\,(t)|1\rangle\langle 1|\uparrow_A(t)\rangle}{\langle\uparrow_A\,(t)|\uparrow_A(t)\rangle}} = \sqrt{\frac{\langle\phi_0|p^{(0\bar{1})}[-t]^{(1)}_{\bar{1}1}[t]^{(1)}_{1\bar{1}}p^{(\bar{1}0)}|\phi_0\rangle}{\langle\phi_0|p^{(0\bar{1})}p^{(\bar{1}0)}|\phi_0\rangle}}\,. \tag{B.12}$$

The superscripts (0) and (1) in Eqs. (B.10), (B.11), and (B.12) refer to the order of perturbation theory with respect to the interexciton coupling (B.4). It can be verified formally that the RHS of Eq. (B.12) is greater than or equal to the absolute value of the RHS of Eq. (B.11).

In order to calculate these quantities, it is convenient to switch from coordinates and momenta to creation and annihilation operators, in terms of which

$$Q_j = \sqrt{\frac{\hbar}{2\omega_j}}\left(A_j^\dagger + A_j\right) \quad \text{and} \quad P_j = \sqrt{\frac{\hbar\omega_j}{2}}\, i\big(A_j^\dagger - A_j\big)\,, \tag{B.13}$$

along with

$$q_j = \sqrt{\frac{\hbar}{2\omega_j}}\left(a_j^\dagger + a_j\right) \quad \text{and} \quad p_j = \sqrt{\frac{\hbar\omega_j}{2}}\, i(a_j^\dagger - a_j)\,. \tag{B.14}$$

Making use of displacement parameters

$$B_j \equiv \frac{d_j}{2}\sqrt{\frac{\omega_j}{\hbar}}\,, \tag{B.15}$$

and

$$\beta_j \equiv \frac{K}{M} B_j\,, \tag{B.16}$$

for the center-of-mass and relative degrees of freedom, respectively, we have

$$\begin{aligned}[t]_{\bar{1}\bar{1}}^{(0)} = e^{-\frac{it}{\hbar}\epsilon_{\bar{1}}} \prod_{j=1}^{N} & e^{B_j(A_j^\dagger - A_j)} e^{-i\omega_j t\left(A_j^\dagger A_j + \frac{1}{2}\right)} e^{-B_j(A_j^\dagger - A_j)} \\ & \times e^{-\beta_j(a_j^\dagger - a_j)} e^{-i\omega_j t\left(a_j^\dagger a_j + \frac{1}{2}\right)} e^{\beta_j(a_j^\dagger - a_j)}\,,\end{aligned} \tag{B.17}$$

and

$$\begin{aligned}[t]_{11}^{(0)} = e^{-\frac{it}{\hbar}\epsilon_{1}} \prod_{j=1}^{N} & e^{B_j(A_j^\dagger - A_j)} e^{-i\omega_j t\left(A_j^\dagger A_j + \frac{1}{2}\right)} e^{-B_j(A_j^\dagger - A_j)} \\ & \times e^{\beta_j(a_j^\dagger - a_j)} e^{-i\omega_j t\left(a_j^\dagger a_j + \frac{1}{2}\right)} e^{-\beta_j(a_j^\dagger - a_j)}\,.\end{aligned} \tag{B.18}$$

Here, $\epsilon_{\bar{1}} = \bar{\epsilon} + M + \frac{J^2}{M^2}\sum_{i=1}^{N}\frac{\omega_i^2 d_i^2}{4}$ and $\epsilon_1 = \bar{\epsilon} - M + \frac{J^2}{M^2}\sum_{i=1}^{N}\frac{\omega_i^2 d_i^2}{4}$. As expected, both zeroth-order evolution operators are direct products of commuting center-of-mass and relative factors, with dynamics under the former being identical in the $\bar{1}$- and 1-states.

The time-evolution operator of first order in the interexciton amplitude transfer can be determined from

$$[t]_{1\bar{1}}^{(1)} = -\frac{i}{\hbar}[t]_{11}^{(0)} \int_0^t d\tau \, [-\tau]_{11}^{(0)} \, \langle 1|H^{(1)}|\bar{1}\rangle \, [\tau]_{\bar{1}\bar{1}}^{(0)} \, , \tag{B.19}$$

where $\langle 1|H^{(1)}|\bar{1}\rangle = -\frac{J}{2M} \sum_{j=1}^{N} \omega_j d_i \sqrt{\hbar\omega_j}(a_j^\dagger + a_j)$. We find

$$\begin{aligned}[t]_{1\bar{1}}^{(1)} = [t]_{11}^{(0)} \, \frac{iJ}{2M} \sum_j \omega_j d_j \sqrt{\frac{\omega_j}{\hbar}} \int_0^t d\tau \, e^{-\frac{2i\tau}{\hbar}M} \prod_{k=1}^{N} e^{\beta_k(a_k^\dagger - a_k)} e^{i\omega_k \tau a_k^\dagger a_k} e^{-\beta_k(a_k^\dagger - a_k)} \\ \times (a_j^\dagger + a_j) \prod_{l=1}^{N} e^{-\beta_l(a_l^\dagger - a_l)} e^{-i\omega_l \tau a_l^\dagger a_l} e^{\beta_l(a_l^\dagger - a_l)} \, . \end{aligned} \tag{B.20}$$

Eq. (B.20) is once again a direct product of center-of-mass and relative factors, and the latter are solely responsible for the deviations from zeroth-order nuclear wave-packet dynamics.

The dynamical and signal calculations of the kind presented in Section 3.5.2 can be carried out using matrix representations of the zeroth- and first-order time-evolution operators in a basis of 0-state vibrational eigenkets $\{|\mathbf{N};\mathbf{n}\rangle = |N_1,\ldots,N_N;n_1,\ldots,n_N\rangle\}$; the matrix elements of these operators can be obtained from Eqs. (B.17), (B.18), and (B.20), and—upon expanding the spatial translation operators ($e^{\pm\beta(a^\dagger - a)}$ for example) in power-series—consist of sums of one-dimensional integrals of scalar functions which are readily evaluated numerically.

The necessary reduced pulse propagators can be found by similar means from Eq. (3.28). We find

$$\begin{aligned} p^{(\bar{1}0)} = \int_{-\infty}^{\infty} \frac{d\tau}{\sigma} f(\tau) \, e^{\frac{i\tau}{\hbar}(\epsilon_{\bar{1}} - \hbar\Omega)} \prod_{j=1}^{N} e^{B_j(A_j^\dagger - A_j)} e^{i\omega_j \tau A_j^\dagger A_j} e^{-B_j(A_j^\dagger - A_j)} e^{-i\omega_j \tau A_j^\dagger A_j} \\ \times e^{-\beta_j(a_j^\dagger - a_j)} e^{i\omega_j \tau a_j^\dagger a_j} e^{\beta_j(a_j^\dagger - a_j)} e^{-i\omega_j \tau a_j^\dagger a_j} \, , \end{aligned} \tag{B.21}$$

and

$$p^{(10)} = \int_{-\infty}^{\infty} \frac{d\tau}{\sigma} f(\tau)\, e^{\frac{i\tau}{\hbar}(\epsilon_1 - \hbar\Omega)} \prod_{j=1}^{N} e^{B_j(A_j^\dagger - A_j)} e^{i\omega_j \tau A_j^\dagger A_j} e^{-B_j(A_j^\dagger - A_j)} e^{-i\omega_j \tau A_j^\dagger A_j}$$
$$\times\, e^{\beta_j(a_j^\dagger - a_j)} e^{i\omega_j \tau a_j^\dagger a_j} e^{-\beta_j(a_j^\dagger - a_j)} e^{-i\omega_j \tau a_j^\dagger a_j}\,. \tag{B.22}$$

Unlike the zeroth- and first-order free evolution operators, the reduced pulse propagators are not direct products of center-of-mass and relative factors, except in the limit of arbitrarily short pulses. Although it is accurate to state that the relative-mode factor in Eq. (B.20) governs interexciton amplitude transfer, this factor becomes inextricably correlated with motion in the center-of-mass coordinate under realistic conditions of photo-excitation and photo-detection.

Equations (B.17) - (B.22) may be inserted in the overlap expressions (B.10) through (B.12) to obtain formulas for WPI-observed interexciton coherence which can be evaluated numerically. Alternatively, these formulas can be further simplified using basic rules of operator algebra, systematically moving $a^\dagger$'s to the left and a's to the right to develop semi-analytic expressions which require only the numerical integration of scalar-valued functions. In the short-pulse limit, this procedure becomes especially straightforward, and Section 3.5.2 quotes and makes use of some of the resulting expressions.

APPENDIX C

ELEMENTS OF $\mathbf{M}$ AND χ FOR THE ANSATZ APPLIED TO HARMONIC POTENTIALS

In writing the elements of M, it is useful to find the overlaps

$$I^{(0)} \equiv \langle\psi|\psi\rangle = Z^2\sqrt{(\frac{\pi}{2})^n \frac{1}{\det \mathbf{a''}}}\,, \tag{C.1}$$

$$I^{(2)}{}_{ij} \equiv \langle\psi|\,(\mathbf{q}-\mathbf{q_0})_i(\mathbf{q}-\mathbf{q_0})_j\,|\psi\rangle = \frac{1}{4}I^{(0)}\mathbf{a''}^{-1}_{ij}\,, \tag{C.2}$$

and

$$\begin{aligned} I^{(4)}{}_{ijkl} &\equiv \langle\psi|\,(\mathbf{q}-\mathbf{q_0})_i(\mathbf{q}-\mathbf{q_0})_j(\mathbf{q}-\mathbf{q_0})_k(\mathbf{q}-\mathbf{q_0})_l\,|\psi\rangle \\ &= \frac{1}{16}I^{(0)}(a''^{-1}_{ij}a''^{-1}_{kl} + a''^{-1}_{ik}a''^{-1}_{jl} + a''^{-1}_{jk}a''^{-1}_{il}). \end{aligned} \tag{C.3}$$

The elements of $\mathbf{M}$ can then be expressed as

$$M_{a'_{ij}a'_{kl}} = (2-\delta_{ij})(2-\delta_{kl})I^{(4)}{}_{ijkl} \tag{C.4}$$

$$M_{a'_{ij}a''_{kl}} = 0 \tag{C.5}$$

$$M_{a'_{ij}p_k} = 0 \tag{C.6}$$

$$M_{a'_{ij}q_k} = -(2-\delta_{ij})p_k I^{(2)}{}_{ij} \tag{C.7}$$

$$M_{a'_{ij}\gamma} = (2-\delta_{ij})I^{(2)}{}_{ij} \tag{C.8}$$

$$M_{a'_{ij}Z} = 0 \tag{C.9}$$

$$M_{a''_{ij}a''_{kl}} = M_{a'_{ij}a'_{kl}} \tag{C.10}$$

$$M_{a''_{ij}p_k} = 0 \tag{C.11}$$

$$M_{a''_{ij}q_k} = 0 \tag{C.12}$$

$$M_{a''_{ij}\gamma} = 0 \tag{C.13}$$

$$M_{a''_{ij}Z} = -\frac{1}{Z}(2-\delta_{ij})I^{(2)}{}_{ij} \tag{C.14}$$

$$M_{p_ip_j} = I^{(2)}{}_{ij} \tag{C.15}$$

$$M_{p_iq_j} = -2(\mathbf{I^{(2)}}\cdot\mathbf{a'})_{ij} \tag{C.16}$$

$$M_{p_i\gamma} = 0 \tag{C.17}$$

$$M_{p_iZ} = 0 \tag{C.18}$$

$$M_{q_iq_j} = -I^{(0)}((\mathbf{a'}\cdot\mathbf{a''}^{-1}\cdot\mathbf{a'})_{ij} + a''_{ij} + p_ip_j) \tag{C.19}$$

$$M_{q_i\gamma} = -p_iI^{(0)} \tag{C.20}$$

$$M_{q_iZ} = 0 \tag{C.21}$$

$$M_{\gamma\gamma} = I^{(0)} \tag{C.22}$$

$$M_{\gamma Z} = 0 \tag{C.23}$$

$$M_{\gamma\gamma} = \frac{I^{(0)}}{Z^2} \tag{C.24}$$

$$\tag{C.25}$$

For writing χ, we use the overlaps

$$X_i^{(1)} \equiv \langle\psi|\, q_i \,|\psi\rangle = q_i I^{(0)}\,, \tag{C.26}$$

$$X_{ij}^{(2)} \equiv \langle\psi|\, q_i q_j \,|\psi\rangle = I_{ij}^{(2)} + q_i q_j I^{(0)}\,, \tag{C.27}$$

$$\begin{aligned} X_{ijk}^{(3)} &\equiv \langle\psi|\, q_i q_j q_k \,|\psi\rangle \\ &= q_k I_{ij}^{(2)} + q_j I_{ik}^{(2)} + q_i I_{jk}^{(2)} + q_i q_j q_k I^{(0)}\,, \end{aligned} \tag{C.28}$$

$$\begin{aligned} X_{ijkl}^{(4)} &\equiv \langle\psi|\, q_i q_j q_k q_l \,|\psi\rangle = I_{ijkl}^{(4)} + q_k q_l I_{ij}^{(2)} + \\ &\quad q_j q_l I_{ik}^{(2)} + q_j q_k I_{il}^{(2)} + q_i q_l I_{jk}^{(2)} + q_i q_k I_{ik}^{(2)} + \\ &\quad q_i q_j I_{jk}^{(2)} + q_i q_j q_k q_l I^{(0)}\,, \end{aligned} \tag{C.29}$$

$$\tag{C.30}$$

and

$$\langle\psi|\, (\mathbf{q}-\mathbf{q_0})_i (\mathbf{q}-\mathbf{q_0})_j \hat{p}_n^2 \,|\psi\rangle \equiv \xi'_{ijn} + i\xi''_{ijn}\,, \tag{C.31}$$

where

$$\xi'_{ijn} = (2a''_{nn} + p_n^2) I_{ij}^{(2)} + 4(\mathbf{a}' \cdot \mathbf{I_{ij}^{(4)}} \cdot \mathbf{a}')_{nn} - 4(\mathbf{a}'' \cdot \mathbf{I_{ij}^{(4)}} \cdot \mathbf{a}'')_{nn}\,, \tag{C.32}$$

and

$$\xi''_{ijn} = -2a'_{nn} I_{ij}^{(2)} + 8(\mathbf{a}' \cdot \mathbf{I_{ij}^{(4)}} \cdot \mathbf{a}'')_{nn}\,. \tag{C.33}$$

For a system with a potential given by

$$V(\mathbf{q}) = \sum_i \sum_{j>i} V_{ij}^{(2)} q_i q_j + \sum_i V_i^{(1)} q_i + V^0\,, \tag{C.34}$$

such as the harmonic oscillator potentials used by the two-particle model Hamiltonian, the elements of χ are

$$\begin{aligned}\chi_{a'_{ij}} = -(2-\delta_{ij})\{&\sum_n \frac{\xi'_{ijn}}{2} + \\ &\sum_n \sum_{m>n} V^{(2)}_{nm}(X^{(4)}_{ijnm} - q_i X^{(3)}_{jnm} - q_j X^{(3)}_{inm} + q_i q_j X^{(2)}_{nm}) + \\ &\sum_n V^{(1)}_n (X^{(3)}_{ijn} - q_i X^{(2)}_{jn} - q_j X^{(2)}_{in} + q_i q_j X^{(1)}_n) + V_0 I^{(2)}_{ij}\}\,, \end{aligned} \tag{C.35}$$

$$\chi_{a''_{ij}} = -(2-\delta_{ij}) \sum_n \frac{\xi''_{ijn}}{2}\,, \tag{C.36}$$

$$\begin{aligned}\chi_{p_i} = -\{&\sum_n \frac{1}{2} p_n I^{(0)} (\mathbf{a}''^{-1} \cdot \mathbf{a}')_{in} + \\ &\sum_n \sum_{m>n} V^{(2)}_{nm}(X^{(3)}_{inm} - q_i X^{(2)}_{nm}) + \\ &\sum_n V^{(1)}_n (X^{(2)}_{in} - q_i X^{(1)}_n)\}\,, \end{aligned} \tag{C.37}$$

$$\chi_{q_i} = p_i E - 2(\mathbf{a}' \cdot \chi_{\mathbf{p}})_i + I^{(0)}(\mathbf{a}'' \cdot \mathbf{p})_i\,, \tag{C.38}$$

where $E = \langle \Psi | \, H \, | \Psi \rangle$,

$$\chi_\gamma = -E\,, \tag{C.39}$$

and

$$\chi_Z = 0\,. \tag{C.40}$$

APPENDIX D

ELEMENTS OF $\mathbf{M}$ AND χ FOR THE ANSATZ APPLIED TO COULOMBIC POTENTIALS

For the Nth-order ansatz introduced in Eq. 4.26, the elements of $\mathbf{M}$ may be split into three regions. Region 1 contains elements M_{mn} for which both $m \leq 2N$ and $n \leq 2N$ hold. Region 2 contains elements M_{mn} for which $m \leq 2N$ but $n > 2N$. Finally, Region 3 contains elements where both m and n are greater than $2N$. Note that we are now using the subscripts of $\mathbf{M}$ to refer to the subscripts of corresponding λ_i, as opposed to the names of the variables as used in Appendix C. Region 1 contains

$$M_{00} = I_0\,, \tag{D.1}$$

$$M_{0,n\neq 0} = \begin{cases} I_{\frac{n+1}{2}}, & \text{if } n \text{ is odd} \\ 0, & \text{if } n \text{ is even} \end{cases} \tag{D.2}$$

and

$$M_{m\neq 0,n\neq 0} = \begin{cases} I_{\frac{n+m+2}{2}}, & \text{if } n \text{ and } m \text{ are both odd} \\ I_{\frac{n+m}{2}}, & \text{if } n \text{ and } m \text{ are both even} \\ 0, & \text{otherwise} \end{cases} . \tag{D.3}$$

Here, unlike in the previous appendix though similarly motivated, $I_m \equiv \int dq\, q^m g^*(q) g(q)$, with

$$I_{m\neq 0} = \frac{1}{2^m} \frac{\partial^m}{\partial \beta'^m} I_0 \tag{D.4}$$

and

$$I_0 = e^{-\frac{\beta'^2}{2\alpha'}} \sqrt{\frac{\pi}{-2\alpha'}}\,. \tag{D.5}$$

In defining I_m, we have introduced $g(q) \;=\; e^{\alpha q^2+\beta q+i\gamma}$. Together with $f(q)=\sum_{n=0}^{N}(A_n q^n)$, we may write the ansatz as $\psi(q)=f(q)g(q)$.

Region 2 contains

$$M_{0n}=\begin{cases}-\Theta''_{\frac{n-2N-1}{2}}\,, & \text{if odd } n\\ \Theta'_{\frac{n-2N}{2}}\,, & \text{if even } n\end{cases} \tag{D.6}$$

and

$$M_{m\neq 0,n}=\begin{cases}-\Theta''_{\frac{m+n-2N}{2}}\,, & \text{if odd } m \text{ and odd } n\\ \Theta'_{\frac{m+n-2N+1}{2}}\,, & \text{if odd } m \text{ and even } n\\ \Theta'_{\frac{m+n-2N-1}{2}}\,, & \text{if even } m \text{ and odd } n\\ \Theta''_{\frac{m+n-2N}{2}}\,, & \text{if even } m \text{ and even } n\end{cases}\,. \tag{D.7}$$

In the above we have introduced $\Theta_m=\Theta'_m+i\Theta''_m\equiv\int dq\, q^m g^*(q)\psi(q)$, with

$$\Theta'_m=\lambda_0 I_0+\sum_{n=1}^{N}\lambda_{2n-1}I_{n+m} \tag{D.8}$$

and

$$\Theta''_m=\sum_{n=1}^{N}\lambda_{2n}I_{n+m}\,. \tag{D.9}$$

Region 3 consists of

$$M_{mn}=\begin{cases}\xi_{\frac{m+n-4N-2}{2}}\,, & \text{if } n \text{ and } m \text{ are both odd}\\ \xi_{\frac{m+n-4N}{2}}\,, & \text{if } n \text{ and } m \text{ are both even}\\ 0, & \text{otherwise}\,,\end{cases} \tag{D.10}$$

where

$$\xi_m\equiv\int dq\, q^m\psi^*(q)\psi(q)=\sum_{n=0}^{N}a_n^*a_nI_{m+2N}+2\ \mathrm{Re}\ \sum_{n=0}^{N}\sum_{\bar{n}=n+1}^{N}a_n^*a_{\bar{n}}I_{m+n+\bar{n}}\,. \tag{D.11}$$

Like $\mathbf{M}$, we may split χ into regions. Region 1 consists of the elements $\chi_{m\leq 2N}$ and Region 2 of $\chi_{m>2N}$. We begin with Region 1, which consists of

$$\chi_0 = \mathrm{Im}\left\{\zeta_0 - \frac{1}{2}\left[\sum_{n=1}^{N} n a_n \left((n-1)I_{n-2} + 4\alpha I_n + 2\beta I_{n-1}\right) + 4\alpha^2\Theta_2 + 4\alpha\beta\Theta_1 + (\beta^2+2\alpha)\Theta_0\right]\right\} \tag{D.12}$$

and

$$\chi_m = \begin{cases} \mathrm{Im}\left\{\zeta_{\frac{m+1}{2}} - \frac{1}{2}\left[\sum_{n=1}^{N} n a_n \left((n-1)I_{n-2+\frac{m+1}{2}} + 4\alpha I_{n+\frac{m+1}{2}} + 2\beta I_{n-1+\frac{m+1}{2}}\right) + 4\alpha^2\Theta_{\frac{m+5}{2}} + 4\alpha\beta\Theta_{\frac{m+3}{2}} + (\beta^2+2\alpha)\Theta\frac{m+1}{2}\right]\right\}, & \text{if odd } m \\ \mathrm{Re}\left\{\frac{1}{2}\left[\sum_{n=1}^{N} n a_n \left((n-1)I_{n-2+\frac{m}{2}} + 4\alpha I_{n+\frac{m}{2}} + 2\beta I_{n-1+\frac{m}{2}}\right) + 4\alpha^2\Theta_{\frac{m+4}{2}} + 4\alpha\beta\Theta_{\frac{m+2}{2}} + (\beta^2+2\alpha)\Theta_{\frac{m}{2}}\right] - \zeta_{\frac{m}{2}}\right\}, & \text{if even } m \end{cases} \tag{D.13}$$

where $\zeta_m \equiv \int dq\, q^m V(q) g^*(q)\psi(q)$. Region 2 contains

$$\chi_m = \begin{cases} \mathrm{Re}\left\{\frac{1}{2}\left[\sum_{n=1}^{N} n a_n \left((n-1)\Theta^*_{n-2+\frac{m-2N-1}{2}} + 4\alpha\Theta^*_{n+\frac{m-2N-1}{2}} + 2\beta\Theta^*_{n-1+\frac{m-2N-1}{2}}\right) + 4\alpha^2\xi_{\frac{m-2N-1}{2}+2} + 4\alpha\beta\xi_{\frac{m-2N-1}{2}+1} + (\beta^2+2\alpha)\xi_{\frac{m-2N-1}{2}}\right] - V_{\frac{m-2N-1}{2}}\right\}, & \text{for odd } m \\ \mathrm{Im}\left\{V_{\frac{m-2N}{2}} - \frac{1}{2}\left[\sum_{n=1}^{N} n a_n \left((n-1)\Theta^*_{n-2+\frac{m-2N}{2}} + 4\alpha\Theta^*_{n+\frac{m-2N}{2}} + 2\beta\Theta^*_{n-1+\frac{m-2N}{2}}\right) + 4\alpha^2\xi_{\frac{m-2N}{2}+2} + 4\alpha\beta\xi_{\frac{m-2N}{2}+1} + (\beta^2+2\alpha)\xi_{\frac{m-2N}{2}}\right]\right\}, & \text{for even } m \end{cases} \tag{D.14}$$

where

$$V_m \equiv \int dq\, q^m V(q)\psi^*(q)\psi(q)\,. \tag{D.15}$$

In Section 4.6, we fit the regularized Coulomb potential to a sum of Gaussians to make solving necessary integrals easier. The integrals ζ_m and V_m are those integrals. Substituting in the Gaussian fit from Eq. 4.25, we obtain

$$\zeta_m = \sum_{i=1}^{3} C_i \int dq\, q^m e^{-c_i q^2} g^*(q)\psi(q) \tag{D.16}$$

$$= \sum_{i=1}^{3} C_i \int dq\, q^m \bar{g}_i^*(q)\psi(q)\,, \tag{D.17}$$

where writing $\bar{g}_i(q) = e^{(\alpha - c_i)q^2 + \beta q + i\gamma}$ makes the connection between ζ_m and Θ_m more obvious. The ζ_ms have expressions analogous to those of the Θ_ms, though the parameters used to calculate analogous I_ms include the c_is. Similarly, we obtain

$$V_m = \sum_{i=1}^{3} C_i \int dq\, q^m \bar{\psi}_i^*(q)\psi(q)\,, \tag{D.18}$$

with $\bar{\psi}_i(q) = f(q)\bar{g}_i(q)$; V_m may be calculated analogously to ξ_m.

REFERENCES CITED

[1] P.A.M. Dirac, "Note on Exchange Phenomena in the Thomas Atom", Math. Proc. Cambridge **26**, 376 (1930).

[2] J. Frenkel, *Wave Mechanics: Advanced General Theory* (Clarendon Press, Oxford, 1934).

[3] A.D. McLachlan, "A variational solution of the time-dependent Schrödinger equation", Mol. Phys. **8**, 39 (1964).

[4] Y. Lee, M. Gorka, J.H. Golbeck and J.M. Anna, "Ultrafast energy transfer involving the red chlorophylls of cyanobacterial photosystem I probed through two-dimensional electronic spectroscopy", J. Am. Chem. Soc. **140**, 11631–11638 (2018).

[5] V. Tiwari, Y.A. Matutes, A. Konar, Z. Yu, M. Ptaszek, D.F. Bocian, D. Holten, C. Kirmaier and J.P. Ogilvie, "Strongly coupled bacteriochlorin dyad studied using phase-modulated fluorescence-detected two-dimensional electronic spectroscopy", Opt. Express **26**, 22327–22341 (2018).

[6] M. Cho, H.M. Vaswani, T. Brixner, J. Stenger and G.R. Fleming, "Exciton analysis in 2D electronic spectroscopy", J. Phys. Chem. B. **109**, 10542–10556 (2005).

[7] S.J. Jang and B. Mennucci, "Delocalized excitons in natural light-harvesting complexes", Rev. Mod. Phys. **90**, 035003 (2018).

[8] M.K. Lee, K.B. Bravaya and D.F. Coker, "First-principles models for biological light-harvesting: phycobiliprotein complexes from cryptophyte algae", J. Am. Chem. Soc. **139**, 7803–7814 (2017).

[9] J.A. Cina, D.S. Kilin and T.A. Humble, "Wave packet interferometry for short-time electronic energy transfer: multidimensional optical spectroscopy in the time domain", J. Chem. Phys. **118**, 46–61 (2003).

[10] V. Tiwari, W.K. Peters and D.M. Jonas, "Electronic resonance with anticorrelated pigment vibrations drives photosynthetic energy transfer outside the adiabatic framework", P. Natl. Acad. Sci. USA **110**, 1203–1208 (2013).

[11] J.A. Cina and G.R. Fleming, "Vibrational coherence transfer and trapping as sources for long-lived quantum beats in polarized emission from energy transfer complexes", J. Phys. Chem. A. **108**, 11196–11208 (2004).

[12] S.E. Bradforth, R. Jimenez, F. van Mourik, R. van Grondelle and G.R. Fleming, "Excitation transfer in the core light-harvesting complex (LH-1) of *Rhodobacter sphaeroides*: an ultrafast fluorescence depolarization and annihilation study", J. Phys. Chem. **99**, 16179–16191 (1995).

[13] V. Butkus, D. Zigmantas, L. Valkunas and D. Abramavicius, "Vibrational vs. electronic coherences in 2D spectrum of molecular systems", Chem. Phys. Lett. **545**, 40–43 (2012).

[14] J.D. Biggs and J.A. Cina, "Using wave-packet interferometry to monitor the external vibrational control of electronic excitation transfer", J. Chem. Phys. **131**, 224101 (2009).

[15] J.D. Biggs and J.A. Cina, "Calculations of nonlinear wave-packet interferometry signals in the pump-probe limit as tests for vibrational control over electronic excitation transfer", J. Chem. Phys. **131**, 224302 (2009).

[16] S. Tomasi, S. Baghbanzadeh, S. Rahimi-Keshari and I. Kassal, "Coherent and controllable enhancement of light-harvesting efficiency", arXiv:1810.03251v1 [physics.chem-ph] (2018).

[17] D.M. Jonas, "Two-dimensional femtosecond spectroscopy", Annu. Rev. Phys. Chem. **54**, 425–463 (2003).

[18] P.F. Tekavec, G.A. Lott and A.H. Marcus, "Fluorescence-detected two-dimensional electronic coherence spectroscopy by acousto-optic phase modulation", J. Chem. Phys. **127**, P214307 (2007).

[19] G.A. Lott, A. Perdomo-Oritz, J.K. Utterback, J.R. Widom, A. Aspuru-Guzik and A.H. Marcus, "Conformation of self-assembled porphyrin dimers in liposome vesicles by phase-modulation 2D fluorescence spectroscopy", P. Natl. Acad. Sci. USA **108**, 16521–16526 (2011).

[20] J. Schellman and H.P. Jensen, "Optical spectroscopy of oriented molecules", Chem. Rev. **87**, 1359–1399 (1987).

[21] Y. Song, A. Schubert, E. Maret, R.K. Burdick, B.D. Dunietz, E. Geva and J.P. Ogilvie, "Vibronic structure of photosynthetic pigments probed by polarized two-dimensional electronic spectroscopy and ab initio calculations", Chem. Sci. **10**, 8143–8153 (2019).

[22] N.S. Ginsberg, J.A. Davis, M. Ballottari, Y.C. Cheng, R. Bassi and G.R. Fleming, "Solving structure in the CP29 light harvesting complex with polarization-phased 2D electronic spectroscopy", Proc. Natl. Acad. Sci. U. S. A. **108**, 3848–3853 (2011).

[23] G.S. Schlau-Cohen, A. Ishizaki, T.R. Calhoun, N.S. Ginsberg, M. Ballottari, R. Bassi and G.R. Fleming, "Elucidation of the timescales and origins of quantum electronic coherence in LHCII", Nat. Chem. **4**, 389–395 (2012).

[24] R. Gera, S.L. Meloni and J.M. Anna, "Unraveling confined dynamics of guests trapped in self-assembled Pd_6L_4 nanocages by ultrafast mid-IR polarization-dependent spectroscopy", J. Phys. Chem. Lett. **10**, 413–418 (2019).

[25] L. Huang, N. Ponomarenko, G.P. Wiederrecht and D.M. Tiede, "Cofactor-specific photochemical function resolved by ultrafast spectroscopy in photosynthetic reaction center crystals", Proc. Natl. Acad. Sci. U. S. A. **109**, 4851–4856 (2012).

[26] J.A. Cina, D. Kilin and T.S. Humble, "Wave packet interferometry for short-time electronic energy transfer: Multidimensional optical spectroscopy in the time domain", J. Chem. Phys. **118**, 46–61 (2003).

[27] J.A. Cina and A.J. Kiessling, "Nuclear wave-packet dynamics in two-dimensional interferograms of excitation transfer systems", in *Coherent Multidimensional Spectroscopy*, edited by M. Cho, Chap. 3 (Springer Nature, Singapore, 2019), pp. 51–85.

[28] A. Matro and J.A. Cina, "Theoretical study of time-resolved fluorescence anisotropy from coupled chromophore pairs", J. Phys. Chem. **99**, 2568–2582 (1995).

[29] K. Wynne and R.M. Hochstrasser, "Anisotropy as an ultrafast probe of electronic coherence in degenerate systems exhibiting Raman scattering, fluorescence, transient absorption and chemical reactions", J. Raman Spectrosc. **26**, 561–569 (1995).

[30] S.J. Jang, "Effects of donor-acceptor quantum coherence and non-Markovian bath on the distance dependence of resonance energy transfer", J. Phys. Chem. C **123**, 5767–5775 (2019).

[31] S. Siwiak-Jaszek and A. Olaya-Castro, "Transient synchronisation and quantum coherence in a bio-inspired vibronic dimer", Faraday Discuss. **216**, 38–56 (2019).

[32] D.M. Jonas, "Vibrational and nonadiabatic coherence in 2D electronic spectroscopy, the Jahn-Teller effect, and energy transfer", Annu. Rev. Phys. Chem. **69**, 327–352 (2018).

[33] M. Maiuri, E.E. Ostroumov, R.G. Saer, R.E. Blankenship and G.D. Scholes, "Coherent wavepackets in the Fenna-Matthews-Olson complex are robust to excitonic-structure perturbations caused by mutagenesis", Nat. Chem. **10**, 177–183 (2018).

[34] C.C. Jumper, I.H.M. van Stokkum, T. Mirkovic and G.D. Scholes, "Vibronic wavepackets and energy transfer in cryptophyte light-harvesting complexes", J. Phys. Chem. B **122**, 6328–6340 (2018).

[35] G.D. Scholes, G.R. Fleming, L.X. Chen, A. Aspuru-Guzik, A. Buchleitner, D.F. Coker, G.S. Engel, R. van Grondelle, A. Ishizaki, D.M. Jonas, J.S. Lundeen, J.K. McCusker, S. Mukamel, J.P. Ogilvie, A. Olaya-Castro, M.A. Ratner, F.C. Spano, K.B. Whaley and X. Zhu, "Using coherence to enhance function in chemical and biophysical systems", Nature **543**, 647–656 (2017).

[36] V. Butkus, J. Alster, E.. Bašinskaitė, R. Augulis, P. Neuhaus, L. Valkunas, H.L. Anderson, D. Abramavicius and D. Zigmantas, "Discrimination of diverse coherences allows identification of electronic transitions of a molecular nanoring", J. Phys. Chem. Lett. **8**, 2344–2349 (2017).

[37] J.A. Cina, P.A. Kovac, C.C. Jumper, J.C. Dean and G.D. Scholes, "Ultrafast transient absorption revisited: Phase-flips, spectral fingers, and other dynamical features", J. Chem. Phys. **144**, 175102 (2016).

[38] J.D. Biggs and J.A. Cina, "Studies of impulsive vibrational influence on ultrafast electronic excitation transfer", J. Phys. Chem. A **116**, 1683–1693 (2012).

[39] J.D. Biggs and J.A. Cina, "Using wave-packet interferometry to monitor the external vibrational control of electronic excitation transfer", J. Chem. Phys. **131**, 224101 (2009).

[40] J.A. Cina and G.R. Fleming, "Vibrational coherence transfer and trapping as sources for long-lived quantum beats in polarized emission from energy transfer complexes", J. Phys. Chem. A **108**, 11196–11208 (2004).

[41] E.C. Wu, E.A. Arsenault, P. Bhattacharyya, N.H.C. Lewis and G.R. Fleming, "Two-dimensional electronic vibrational spectroscopy and ultrafast excitonic and vibronic photosynthetic energy transfer", Faraday Discuss. **216**, 116–132 (2019).

[42] J.D. Gaynor, A. Petrone, X. Li and M. Khalil, "Mapping vibronic couplings in a solar cell dye with polarization-selective two-dimensional electronic-vibrational spectroscopy", J. Phys. Chem. Lett. **9**, 6289–6295 (2018).

[43] C. Fang, L. Tang and C. Chen, "Unveiling coupled electronic and vibrational motions of chromophores in condensed phases", J. Chem. Phys. **151**, 200901 (2019).

[44] J.A. Cina and P.A. Kovac, "How fissors works: Observing vibrationally adiabatic conformational change through femtosecond stimulated Raman spectroscopy", J. Phys. Chem. A **117**, 6084–6095 (2013).

[45] C. Lee, C.H. Choi and T. Joo, "A solvent-solute cooperative mechanism for symmetry-breaking charge transfer", Phys.Chem.Chem.Phys. **22**, 1115–1121 (2020).

[46] L. Kringle, N.P.D. Sawaya, J. Widom, C. Adams, M.G. Raymer, A. Aspuru-Guzik and A.H. Marcus, "Temperature-dependent conformations of exciton-coupled Cy3 dimers in double-stranded DNA", J. Chem. Phys. **148**, 085101 (2018).

[47] J.R. Widom, W. Lee, A. Perdomo-Ortiz, D. Rappoport, T.F. Molinski, A. Aspuru-Guzik and A.H. Marcus, "Temperature-dependent conformations of a membrane supported zinc porphyrin tweezer by 2D fluorescence spectroscopy", J. Phys. Chem. A **117**, 6171–6184 (2013).

[48] P.F. Tekavec, T.R. Dyke and A.H. Marcus, "Wave packet interferometry and quantum state reconstruction by acousto-optic phase modulation", J. Chem. Phys. **125**, 194303 (2006).

[49] J.M. Womick and A.M. Moran, "Vibronic enhancement of exciton sizes and energy transport in photosynthetic complexes", J. Phys. Chem. B **115**, 1347–1356 (2011).

[50] J.C. Dean, T. Mirkovic, Z.S.D. Toa, D.G. Oblinsky and G.D. Scholes, "Vibronic enhancement of algae light harvesting", Chem **1**, 858–872 (2016).

[51] L. Allen and J.H. Eberly, *Optical Resonance and Two-Level Atoms* (Dover Publications, New York, 1975).

[52] L.W. Ungar and J.A. Cina, "The relaxation dynamics and short-time optical response of a multi-mode open system", J. Phys. Chem. A **102**, 7382–7392 (1998).

[53] L.W. Ungar and J.A. Cina, "Short-time fluorescence Stokes shift dynamics", Adv. Chem. Phys. **100**, 171–228 (1997).

[54] T. Mirkovic, E.E. Ostroumov, J.M. Anna, R. van Grondelle, Govindjee and G.D. Scholes, "Light absorption and energy transfer in the antenna complexes of photosynthetic organisms", Chem. Rev. **117**, 249–293 (2017).

[55] B. Kahr and R.W. Gurney, "Dyeing crystals", Chem. Rev. **101**, 893–951 (2001).

[56] B. Kahr and A.G. Shtukenberg, "Dyeing crystals since 2000", CrystEngComm **18**, 8988–8898 (2016).

[57] C. Hetzer, D.M. Guldi and R.R. Tykwinski, "Pentacene dimers as a critical tool for the investigation of intramolecular singlet fission", Chem. Eur. J. **24**, 8245–8257 (2018).

[58] S. Mueller, S. Draeger, X. Ma, M. Hensen, T. Kenneweg, W. Pfeiffer and T. Brixner, "Fluorescence-detected two-quantum and one-quantum-two-quantum 2D electronic spectroscopy", J. Phys. Chem. Lett. **9**, 1964–1969 (2018).

[59] S. Hoyer and K.B. Whaley, "Inverting pump-probe spectroscopy for state tomography of excitonic systems", J. Chem. Phys. **138**, 164102 (2013).

[60] J. Yuen-Zhou, J.J. Krich, M. Mohseni and A. Aspuru-Guzik, "Quantum state and process tomography of energy transfer systems via ultrafast spectroscopy", Proc. Natl. Acad. Sci. **108**, 17615–17620 (2011).

[61] J. Yuen-Zhou and A. Aspuru-Guzik, "Quantum process tomography of excitonic dimers from two-dimensional electronic spectroscopy. I. General theory and application to homodimers", J. Chem. Phys. **134**, 134505 (2011).

[62] L.A. Pachón, A.H. Marcus and A. Aspuru-Guzik, "Quantum process tomography by 2D fluorescence spectroscopy", J. Chem. Phys. **142**, 212442 (2015).

[63] T.S. Humble and J.A. Cina, "Nonlinear wave-packet interferometry and molecular state reconstruction in a vibrating and rotating diatomic molecule", J. Phys. Chem. B **110**, 18879–18892 (2006).

[64] J.A. Cina, "Wave-packet interferometry and molecular state reconstruction: Spectroscopic adventures on the left-hand side of the Schrödinger Equation", Annu. Rev. Phys. Chem. **59**, 319–342 (2008).

[65] J. Yuen-Zhou, D.H. Arias, D.M. Eisele, C.P. Steiner, J.J. Krich, M.G. Bawendi, K.A. Nelson and A. Aspuru-Guzik, "Coherent exciton dynamics in supramolecular light-harvesting nanotubes revealed by ultrafast quantum process tomography", ACS NANO **8**, 5527–5534 (2014).

[66] M. Marcus, G.C. Knee and A. Datta, "Towards a spectroscopic protocol for unambiguous detection of quantum coherence in excitonic energy transport", Faraday Discuss. **221**, 110–132 (2019).

[67] M.M. Wilde, J.M. McCracken and A. Mizel, "Could light harvesting complexes exhibit non-classical effects at room temperature?", Proc. R. Soc. A **466**, 1347–1363 (2010).

[68] D.V. Voronine, D. Abramavicius and S. Mukamel, "Coherent control protocol for separating energy-transfer pathways in photosynthetic complexes by chiral multidimensional signals", J. Phys. Chem. A **115**, 4624–4629 (2011).

[69] D.V. Voronine, D. Abramavicius and S. Mukamel, "Chirality-based signatures of local protein environments in two-dimensional optical spectroscopy of two species photosynthetic complexes of green sulfur bacteria: Simulation study", Biophys. J. **95**, 4896–4907 (2008).

[70] R.B. Woodward and R. Hoffman, "The Conservation of Orbital Symmetry", Angew. Chem. Int. Edit **8**, 781 (1969).

[71] F.A. Cotton, *Chemical Applications of Group Theory*, 3rd ed. (John Wiley & Sons, New York, 1990).

[72] A. Szabo and N.S. Ostlund, *Modern Quantum Chemistry: Introduction to Advanced Electronic Structure Theory* (Dover Publications, Inc., Mineola, NY, 1996).

[73] C.J. Cramer, *Essentials of Computational Chemistry: Theories and Models*, 2nd ed. (John Wiley & Sons, Ltd, West Sussex, England, 2004).

[74] D.R. Hartree and W. Hartree, "Self-Consistent Field, with Exchange, for Beryllium", P. Roy. Soc. Lond. A. Mat. **150**, 9 (1935).

[75] D.R. Hartree, "The Wave Mechanics of an Atom with a Non-Coulomb Central Field. Part I. Theory and Methods", Math. Proc. Cambridge **24**, 89 (1928).

[76] T. Helgaker, T.A. Ruden, P. Jørgensen, J. Olsen and W. Klopper, "A priori calculation of molecular properties to chemical accuracy", J. Phys. Org. Chem. **17**, 913 (2004).

[77] M.A. Morales, R. Clay, C. Pierleoni and D.M. Ceperley, "First Principles Methods: A Perspective from Quantum Monte Carlo", Entropy **16**, 287 (2014).

[78] K. Burke, "Perspective on Density Fuctional Theory", J. Chem. Phys. **136**, 150901 (2012).

[79] G.H. Booth and G.K. Chan, "Communication: Excited States, Dynamic Correlation Functions and Spectral Properties From Full Configuration Interaction Quantum Monte Carlo", J. Chem. Phys. **137**, 191102 (2012).

[80] A. Humeniuk and R. Mitrić, "Excited States from Quantum Monte Carlo in the Basis of Slater Determinants", J. Chem. Phys. **141**, 194104 (2014).

[81] E. Heller, "Time-Dependent Approach to Semiclassical Dynamics", J. Chem. Phys. **62**, 1544 (1975).

[82] E. Heller, "Frozen Gaussians: A Very Simple Semiclassical Approximation", J. Chem. Phys. **75**, 2923 (1981).

[83] B.R. Landry, A. Wasserman and E.J. Heller, "Semiclassical Ground-State Energies of Many-Electron Systems", Phys. Rev. Lett. **103**, 066401 (2009).

[84] E.J. Heller, "Time dependent variational approach to semiclassical dynamics", J. Chem. Phys. **64**, 63 (1976).

[85] S.Y. Lee and E.J. Heller, "Exact time-dependent wave packet propagation: Application to the photodissociation of methyl iodide", J. Chem. Phys. **76**, 3035 (1982).

[86] P.A. Kovac and J.A. Cina, "Mixed quantum/semiclassical wave-packet dynamical method for condensed-phase molecular spectroscopy signals", J. Chem. Phys. **147**, 224112 (2017).

[87] W.H. Press, B.P. Flannery, S.A. Teukolsky and W.T. Vetterling, *Numerical Recipes* (Cambridge University Press, Cambridge, 1986).

[88] B. Kloss, I. Burghardt and C. Lubich, "Implementation of a novel projector-splitting integrator for the multi-configurational time-dependent Hartree approach", J. Chem. Phys. **146**, 174107 (2017).

[89] J.C. Light and T. Carrington, Jr., "Discrete-Variable Representations and Their Utilization", in *Advances in Chemical Physics, Volume 114*, edited by I. Prigogine and S. A. Rice (John Wiley & Sons, Inc., New York, NY, 2007).

[90] E. Faou, V. Gradinaru and C. Lubich, "Computing semi-classical quantum dynamics with Hagedorn wavepackets", SIAM J. Sci. Comput. **31**, 3027–3041 (2009).

[91] C.T. Chapman, X. Cheng and J.A. Cina, "Numerical Tests of a Fixed Vibrational Basis/Gaussian Bath Theory for Small Molecule Dynamics in Low-Temperature Media", J. Phys. Chem. A. **115**, 3980 (2011).

[92] D. Neuhauser, "Bound state eigenfunctions from wave packets: Time $\rightarrow$ energy resolution", J. Chem. Phys. **93**, 2611 (1990).

[93] M.R. Wall and D. Neuhauser, "Extraction, through filter-diagonalization, of general quantum eigenvalues or classical normal mode frequencies from a small number of residues or a short-time segment of a signal. I. Theory and application to a quantum-dynamics model", J. Chem. Phys. **102**, 8011 (1995).

[94] Y. Wang, T. Carrington, Jr. and G.C. Corey, "A time-to-energy Fourier resolution method for calculating bound state energies and wavefunctions. Analysis of the method and application to 2D ArHCl", Chem. Phys. Lett. **228**, 144 (1994).

[95] M.H. Beck and H.D. Meyer, "Efficiently computing bound-state spectra: A hybrid approach of the multi-configuration time-dependent Hartree and filter-diagonalization methods", J. Chem. Phys. **114**, 2036 (2001).

[96] A.D. McLachlan and M.A. Ball, "Time-Dependent Hartree-Fock Theory for Molecules", Rev. Mod. Phys. **36**, 844 (1964).

[97] T. Kato and H. Kono, "Time-dependent multiconfiguration theory for electron dynamics of molecules in an intense laser field", Chem. Phys. Lett. **392**, 533 (2004).

[98] S. Ohmura, T. Kato, T. Oyamada, S. Koseki, H. Ohmura and H. Kono, "A single-electron picture based on the multiconfiguration time-dependent Hartree-Fock method: application to the anisotropic ionization and subsequent high-harmonic generation of the CO molecule", J. Phys. B:At. Mol. Opt. Phys. **51**, 034001 (2018).

[99] J.J. Goings, P.J. Lestrange and X. Li, "Real-time time-dependent electronic structure theory", WIREs Comput. Mol. Sci. **8**, 1341 (2018).

[100] M.V. Berry, "Quantal phase factors accompanying adiabatic changes", Proc. R. Soc. Lond. A **392**, 45–57 (1984).